Ultrasound-modulated Microbubbles as a Contrast Agent for Optical Spectroscopy in Biomedical Applications

A thesis submitted for the degree of Doctor of Philosophy (Ph.D.) at University College London

Jack E. Honeysett

Biomedical Optics Research Laboratory
Department of Medical Physics and Bioengineering
University College London

July, 2013

I hereby declare that the work presented in this thesis is my own, and where information has been derived from other sources, those sources are credited.

Jack Honeysett

Abstract

Microbubbles, which are currently used as contrast agents for diagnostic ultrasound (US) imaging, are proposed in this thesis as an optical scattering contrast agent for US-modulated light. Sometimes known as acousto-optic (AO) imaging, this is a hybrid technique which combines measurement of diffuse light in a turbid medium (such as biological tissue) with US, which modulates the properties of the tissue, specifically density, optical scattering and optical absorption. Hence the light field passing through the insonified region will also be modulated. The modulated optical signal provides greater spatial resolution than is usually achieved with diffuse light, however this signal is often very small compared with the background of unmodulated light.

This work investigates the use of microbubbles to amplify the US-modulation of light within the US focal region, by acting as an optical scattering contrast agent. The approach combines analytical modelling of microbubble behaviour under US using solutions of a Rayleigh-Plesset type equation with Monte Carlo (MC) modelling of light transport. Simulations of 780 nm wavelength light reflected from a large (10 mm diameter) blood vessel below a 10 mm depth of tissue show that a measurable change in optical attenuation is induced by insonifying microbubbles within the blood vessel. To model this complex geometry an approach based on perturbation Monte Carlo (pMC) is used, which improves the computational efficiency by several orders of magnitude. This microbubble-enhanced optical attenuation change (MOA) is also measured experimentally from an intralipid phantom containing microbubbles, which are insonified by US at clinically relevant pressures, using a 780 nm laser source and photon counter. The magnitude of this MOA signal is shown to increase with applied US pressure and also with microbubble concentration. Finally, a dual-wavlength optical measurement of MOA from a blood vessel is simulated using pMC. An analytical algorithm based on the Beer-Lambert law is derived which can accurately infer the oxygen satura-

tion of the blood vessel from this MOA measurement for blood vessel up to 20 mm below the tissue surface. This algorithm is accurate even when the oxygenation of the surrounding tissue varies. This suggests that this technique could be used to measure venous oxygen saturation in superficial blood vessels such as the jugular vein or pulmonary artery, particularly in young children.

Five publications resulting from this work can be found at the end of this thesis [46–49, 67].

Acknowledgements

Firstly, I would like to thank my supervisors for their help and advice during this project: Terence Leung, for regular support and assistance with much of this work, especially implementing the Monte Carlo code on a GPU. Eleanor Stride, for guidance on the practical aspects of working with microbubbles, and for introducing me to the 'bubble people' in the UK. Jing Deng, for advising on clinical measurements using ultrasound contrast agents.

I would like to thank the many people working in the Medical Physics department at UCL who have helped me somewhere along the way. In the Biomedical Optics group, Sam Powell has provided assistance with the Monte Carlo model of light, expert advice on all things acoustic as well as entertainment at conferences. Sonny Gunadi and Shihong Jiang shared their experience with the experimental side of acousto-optics and in particular designing tissue phantoms. Thanks also to Teedah Soonthornsaratoon for helping me to organise social events for the group, and for taking control of the social committee off of my hands when I discovered that writing up a thesis was not conducive to fun.

I have also very much appreciated the support of my friends and family during this project so far. In no logical order: Jon Hewer and Sarah Henderson for sharing the pain of flat-hunting in London and also cooking tips with me. Atiyo Ghosh for philosophical discussions on subjects including the mathematics of carrots. Naomi Banfield for cheering loudly during my acoustic performances at open mic evenings. To both Atiyo and Naomi together for deciding to get married on the other side of the world during the final months of my project, giving me a much-needed holiday. Jim Allen for driving the monstrous SUV on this holiday. Ben Sinclair for sharing humour, a mild obsession with Spanish cuisine and culture, and many enjoyable hours spent forming a musical band in tribute to the prodigious antipodean tal-

ent of Tim Minchin. Ryan Dee for many entertaining evenings in London, where we managed to leave our possessions behind in several different establishments. Finally, my parents Lis and Ian, sisters Rosie and Grace, nieces Chloe and Tilly, for always being there to share Sunday dinners and lasagna disasters.

This work was funded primarily by the Engineering and Physical Sciences Research Council, the British Heart Foundation and the Medical Research Council, who are the main sponsors of the CoMPLEX doctoral training centre at UCL (Centre for Mathematics and Physics in the Life Sciences and Experimental Biology).

It's a turnaround jump shot
It's everybody jumpstart
It's every generation throws a hero up the pop charts
Medicine is magical and magical is art
Thinking of the Boy in the Bubble
And the baby with the baboon heart

And I believe
These are the days of lasers in the jungle
Lasers in the jungle somewhere
Staccato signals of constant information
A loose affiliation of millionaires
And billionaires, and baby

These are the days of miracle and wonder
This is the long-distance call
The way the camera follows us in slo-mo
The way we look to us all
The way we look to a distant constellation
That's dying in a corner of the sky
These are the days of miracle and wonder
And don't cry baby, don't cry.

Simon, Paul. "The Boy In The Bubble." Music by Paul Simon and Forere Mothoeloa, *Graceland*, Warner Bros. 1986.

Contents

Table of Symbols

Symbol	Unit	Description
μ_a	m^{-1}	Optical absorption coefficient
I	$\mathrm{W\ m}^{-2}$	Light intensity
l	m	Pathlength
A		Absorbance
c	M	Concentration of absorber
α	$\mathrm{M}^{-1}\ \mathrm{m}^{-1}$	Specific absorption coefficient
μ_s	m^{-1}	Optical scattering coefficient
$p(\hat{s}, \hat{s'})$		Scattering phase function
g		Scattering anisotropy factor
μ_s'	m^{-1}	Reduced scattering coefficient
l'	m	Transport mean free path
$L(\vec{r}, \hat{s}, t)$	$\mathrm{W\ m}^{-2}\ \mathrm{sr}^{-1}$	Radiance
$\Phi(\vec{r}, t)$	$\mathrm{W\ m}^{-2}$	Isotropic fluence rate
$\vec{J}(\vec{r}, t)$	$\mathrm{W\ m}^{-2}$	Flux vector term
D	m	Diffusion coefficient
n		Optical refractive index
η		Elasto-optical coefficient
ρ_L	$\mathrm{kg\ m}^{-3}$	Fluid density
P_a	Pa	Acoustic pressure
v_a	$\mathrm{m\ s}^{-1}$	Acoustic speed
Q		Quality factor
k_0	m^{-1}	Optical wavenumber
A_a	m	Acoustic amplitude
ω_a	$\mathrm{rad\ s}^{-1}$	Acoustic angular frequency
f_a	Hz	Acoustic frequency
k_a	m^{-1}	Acoustic wavenumber

ϕ_d		Phase shift of a photon as a result of scatterer displacement
ϕ_n		Phase shift of a photon as a result of refractive index modulation
ϕ_r		Phase shift of a photon as a result of radiated pressure from bubbles
E	N C^{-1}	Electric field of a photon
G_1		Autocorrelation of the optical electric field
I_n		Spectral power of the autocorrelation at a frequency $n\omega_a$
T_a	s^{-1}	Acoustic period
M		Modulation depth
P_0	Pa	Ambient liquid pressure
P_G	Pa	Pressure inside a bubble
R_0	m	Equilibrium radius of a bubble
d_s	m	Effective thickness of a bubble shell
R	m	Radius of microbubble at time t
$\dot{R}$	m s^{-1}	Velocity of microbubble wall
$\ddot{R}$	m s^{-2}	Acceleration of microbubble wall
η_L	Pa s	Viscosity of surrounding fluid
f_{ce}	Pa	Elastic resistance
f_{cd}	Pa	Dissipative resistance
σ	N m^{-1}	Surface tension
k		Polytropic constant
M		Mach number
G_s	Pa	Effective shear modulus
β	Pa^{-1}	Response function for linear bubble oscillations
ξ		Relative phase of linear oscillation
X_0		
X_1		Response functions of second order oscillations
X_2		
x		Particle size parameter
m		Refractive index ratio
T	K	Temperature
R	J kg^{-1} mol^{-1}	Molar gas constant
A	m^3 mol^{-1}	Molar refractivity
ρ_b	m^{-3}	Density of microbubbles

$\mu_{s,b}$	m^{-1}	Optical scattering coefficient of microbubbles
θ	rad	Photon deflection angle
λ_0	m	Optical wavelength
P_{rad}	Pa	Radiated pressure
s	m	Photon step size between scattering events
ζ		Uniformly distributed random variable
τ	s	Time delay between photon arrivals
ϵ	m^{-1} mol^{-1}	Specific extinction coefficient
ΔA		Change in optical attenuation relative to reference level
I_{ref}	W m^{-2}	Light intensity at reference level
SO_2		Oxygen saturation
S_vO_2		Oxygen saturation of blood vessel
S_tO_2		Oxygen saturation of surrounding tissue
A_{US}		Optical attenuation in the presence of ultrasound
MOA		Microbubble-enhanced optical attenuation
ΔA		Differential attenuation
$\Sigma_{O,v}$		Sensitivity of optical signal to S_vO_2
$\Sigma_{O,t}$		Sensitivity of optical signal to S_tO_2
$\Sigma_{AO,v}$		Sensitivity of acousto-optic signal to S_vO_2
$\Sigma_{AO,t}$		Sensitivity of acousto-optic signal to S_tO_2
l_v	m	Partial path length of photon in blood vessel
l_t	m	Partial path length of photon in tissue
Δl_v	m	US-induced change in partial path length of photon in blood vessel
Δl_t	m	US-induced change in partial path length of photon in tissue

Table of Acronyms

Acronym	Description
US	Ultrasound
AO	Acousto-optics/Acousto-optical
RTE	Radiative transfer equation
DE	Diffusion equation
UCA	Ultrasound contrast agent
UL	Ultrasound-modulation of light
AC	Time-varying signal (alternating current)
DC	Time-indepedent signal (direct current)
UCA	Ultrasound contrast agent
CW	Continuous wave
RMS	Root mean square
GPU	Graphic processing unit
NIRS	Near infrared spectroscopy
MC	Monte Carlo
UOT	Ultrasound-modulated optical tomography
CCD	Charge-coupled device

Chapter 1

Introduction

Historical Background

In 1895 Wilhelm Röntgen created skeletal images of his wife's hand using X-rays. Medical imaging of the human body has since made use of various forms of radiation. Unfortunately for these early researchers (including Mrs. Röntgen) the main disadvantage of this original method, which was only realised some time later, is that X-rays have a harmful ionising effect. Magnetic Resonance Imaging (MRI) is an alternative which does not use ionising radiation, however the cost and size of the equipment required as well as the limited temporal resolution leaves scope for certain clinical roles to be fulfilled by other imaging modalities. One such technique is diffuse optical imaging, whereby measurements of the attenuation of light due to scattering and absorption in biological tissue can be used to infer information about the structure and composition of that tissue. The propagation of light through such a turbid medium is analagous to a diffusion process, in contrast with the ballistic description of light travelling through a non-scattering medium such as air. Fortunately the optical attenuation of biological tissue is sufficiently low that visible red or near infrared light can be detected after penetrating a depth of several centimetres: this wavelength range is known as the tissue optical window.

Photons in the visible range do not have sufficient energy to ionise tissue, the only risk associated with these techniques being the deposition of energy as heat. Optical imaging is routinely used for diagnostic purposes, in particular the spectroscopic measurement of tissue oxygenation [53]. This makes use of the fact that the absorption spectra of oxyhemoglobin and deoxyhemoglobin are distinct, and so their relative concentrations can be resolved using multiple wavelengths of light. There are however still limitations associated with this technique. Highly absorbing regions such as large blood vessels do not contribute to an optical signal [31] since the fluence within them becomes very small, and therefore only a small proportion of the detected light signal will have passed through these regions. The spatial resolution of any optical measurement is also inherently limited, since light spreads out diffusely in a scattering medium such as tissue.

Acousto-optic (AO) imaging has been proposed as a hybrid technique combining focused ultrasound (US) with diffuse optical measurements in a scattering medium. Changes in pressure as a result of the sound field cause modulation of the properties of the tissue (such as density, refractive index, optical absorption and scattering), which in turn will cause small changes in the optical field close to the focal US region. The light arriving at an optical detector on the surface of the tissue will have a component which has passed through the US focal region (and hence been modulated in intensity and phase), and a component which travelled through another diffusive route to the detector. Extracting this modulated component from the often large background of unmodulated light is a significant challenge: many techniques use an approach which makes use of interference effects between photons arriving at a detector, creating dark and light speckles. Extracting the component of this speckle pattern which varies at the same frequency as the US field, known as the AC light signal, can give a measure of the AO modula-

tion [90]. This relies on the phase relationships between photons arriving at a detector, and hence requires coherent light. Changes in the mean intensity of light, the DC signal, are generally small, and often not detectable using US pressures which are safe for clinical use or from phantoms of a realistic size.

Ultrasound has a successful history in its own right in medical diagnostic imaging. However the contrast provided by US images is often not sufficient to observe small structures such as fine blood vessels, since this depends on the difference in acoustic properties on the boundary of these structures, and so different tissue types of similar densities do not provide a large reflected signal. In order to improve this shortcoming of US images, contrast agents have been developed, microbubbles being the most common contrast agent to be used clinically [123]. These can be formed as a suspension in liquid[1] and injected intravenously as required. Small bubbles of gas (1 μm radius) are much more compressible than the surrounding liquid, and so will oscillate under US and scatter more sound energy than tissue alone. This has been used to improve the contrast of blood vessels in an US image, but more recently microbubbles have been proposed as contrast agents for other combined modality AO systems [40, 139]. The size variations of microbubbles oscillating under US can be described by several theoretical models [65]. These size variations are expected to lead to changes in the optical properties of the bubbles in addition to the acoustic properties for which they were originally designed.

Clinical Motivation

Optical measurements in biological tissue are already in use for clinical monitoring, including continuous measurement of tissue oxygen saturation [32].

[1] e.g. either from freeze-dried powder or by agitation, using the protein surfactants present in blood.

This technique of near infrared spectroscopy (NIRS) is, however, limited by strong optical scattering in tissue. The measurement accounts for a large volume of tissue, therefore NIRS provides only a bulk estimate of tissue oxygenation rather than being sensitive to more localised changes in blood oxygenation. Measuring blood oxygen saturation inside blood vessels currently requires an intravenous catheter to take constant samples for analysis outside the body: for example, the monitoring of oxygen saturation in the pulmonary artery is used in intensive care medicine to provide an early-warning indication of the risk of cardiac failure. Performing such a measurement invasively is both costly and carries significant patient risk [104].

The improved spatial resolution of AO techniques over NIRS make it a promising candidate for performing spectroscopic measurements of venous oxygen saturation in blood vessels such as the pulmonary artery without the need for catheterisation. Contrast agent injections have been shown to improve diagnostic US image quality in the pulmonary artery [34]. In this work the use of intravenous microbubbles is investigated as a means of amplifying the AO signal to a level which would make the technique feasible for clinical monitoring. The feasibility of any method for this clinical application will be judged according to the following criteria: can the method distinguish between venous oxygen saturation and the (often higher) oxygen saturation in surrounding arteries and capillaries? Is the method successful at clinically safe US pressures? Is the method successful using microbubble concentrations which can be achieved *in vivo*? Is the method robust to changes such as those due to noise in the signal?

Outline of Thesis

In this chapter the work has been introduced in the context of medical imaging, and in particular the clinical monitoring of oxygen saturation using NIR light. A clinical application for which NIRS has been unsuccessful, the mon-

itoring of oxygen saturation in a large vein, has been presented and the need for a non-invasive solution to this problem has been discussed.

Chapter 2 will outline the theoretical background that underpins the work of the following chapters, including a theoretical description of how light travels through a highly scattering turbid medium such as biological tissue. Models for describing the propagation of light, such as those based on the diffusion equation or radiative transfer, will be presented and their relevance to this work discussed. A description of the interactions between US and light in a turbid medium is given, including the mechanisms by which US is known to modulate the transport of light through turbid media, and this is compared with models which describe the dynamical behaviour of insonified microbubbles.

In order to first understand how microbubbles may interact with both US and NIR light in biological tissue, theoretical models describing the behaviour of microbubbles under US will be investigated. Chapter 3 presents solutions to some of these models of bubble dynamics, along with their implications for the optical properties of microbubbles. A novel mechanism for modulating the phase of coherent light by microbubbles, as as means of amplifying the AO effect, is proposed.

In Chapter 4 the theory of light transport in biological and turbid media will be discussed, including the effect of US on the optical properties of a medium. A Monte Carlo model which simulates the transport of light through a turbid medium containing microbubbles and an US field is developed, and this is used to investigate the feasibility of using microbubble-enhanced AO techniques to measure changes in optical properties. In particular the effect of insonified microbubbles on both AC and DC modulation of a light signal is modelled in order to inform the experimental and theoretical studies of the following chapters. The sensitivity of this DC light signal to changes in the oxygenation of a large blood vessel containing microbubbles is investigated, to confirm that this technique is worthy of further investigation.

Chapter 5 deals with some of the issues encountered in Chapter 4, particularly with the computational time required to simulate highly absorbing media such as blood using a MC model of light transport. Here a more computationally efficient model is developed based on perturbation Monte Carlo (pMC) which allows the optical properties of the medium to be modified by post-processing the results of the simulation, rather than requiring a completely new simulation to be run. The results of this model are validated against a standard MC model, showing that it is equally accurate and significantly faster, and therefore more suitable for the parametric sensitivity analysis which will be required in the following chapters.

In Chapter 6 this pMC model is validated against an experimental investigation, in which the change in the AC light level (i.e. the light intensity) is measured as a result of US modulation with microbubbles. A phantom containing intralipid and microbubbles is insonified, and a photon counter is used to measure the change in light intensity transmitted through the phantom when the US is turned on and off. The magnitude of this microbubble-enhanced optical attenuation change (MOA) is recording as a function of microbubble concentration, US pressure, and background scattering in the medium for two types of microbubbles: SonoVue (which are used clinically) and Expancel (which are not). This is used to access the feasibility and limitations of this technique for the application of measuring venous blood oxygenation, in particular with reference to the performance with clinically safe US pressures and with clinically achievable microbubble concentrations.

Chapter 7 uses this experimentally validated pMC model of light transport with microbubbles and US to investigate a more complex phantom geometry which more closely matches the clinical application, i.e. a deep vein surrounded by tissue which may have a different (and variable) oxygen saturation. An algorithm is derived which relates the MOA signal at two wavelengths to the venous oxygen saturation, and can therefore be used to predict this value given these measurements at the surface of the tissue. In order

to assess the performance of this algorithm, it is compared with the current standard of non-invasive oxygen saturation measurement which uses NIRS. The accuracies of both algorithms for predicting venous oxygen saturation when surrounding tissue saturation is not constant are compared. The performances of both algorithms are also compared when instrumentation noise is present in the light intensity measurements, in order to assess the suitability of an MOA-based technique for the clinical application outlined in this chapter.

Finally, Chapter 8 discusses the strengths and limitations of this technique, how far this thesis supports its use for the clinical application of venous oximetry, and the further questions which remain from the work within this thesis.

Chapter 2

Theoretical background

The hybrid medical imaging techniques described in this thesis are concerned with the propagation of light and of ultrasound through biological tissue. Near infrared light can be detected after travelling several centimetres through tissue, and the attenuation of this signal dependents on the composition of the tissue. The theoretical descriptions of optical scattering and absorption outlined in this chapter are used in chapters 4 and 6 of this work. In chapters 4 and 6 the interactions between ultrasound and light in a turbid medium are used to simulate and measure an ultrasound-modulated optical signal. The theory describing these interactions is presented here. Microbubbles, which are a clinical ultrasound contrast agent, are used in chapters 5 and 7 of this work, where they are used to enhance the ultrasound-modulation of an optical field in tissue. A description of the nature of microbubble contrast agents, their behaviour under ultrasound and the effect of the bubble coating is included in this chapter.

2.1 Optics in tissue

In this section, the optical properties of biological media are discussed, including commonly used models for describing the interactions between light

and tissue. The key properties this section focuses on are absorption of light by tissue, and the scattering of light inside tissue.

2.1.1 Absorption

Light propagating through biological tissue interacts with molecules or structural elements[1] in the medium. The reduction in light intensity as a result of these interactions can be represented by the optical absorption coefficient μ_a. This is defined by the Lambert-Bouguer Law, assuming that photons are absorbed and not re-emitted:

$$\frac{dI}{I} = -\mu_a dl \Rightarrow I = I_0 \exp\left(-\mu_a l\right) \tag{2.1}$$

where I is the light intensity and dI is the intensity change after travelling a distance dl in the medium. The light intensity of a beam is expected to fall to $\frac{1}{e}$ of its intial value after a pathlength of $\frac{1}{\mu_a}$. The incident light intensity is represented by I_0 (i.e. $I = I_0$ when $l = 0$). While the absorption coefficient is a property of the material, another quantity can be derived which describes the effect of the absorbing medium on a particular light path: the absorbance A. Here absorbance (a dimensionless quantity) is defined as the logarthmic ratio of incident light intensity to the remaining light intensity after travelling a distance l through an absorbing medium:

$$A = \ln \frac{I_0}{I} = \mu_a l \tag{2.2}$$

If the medium in question contains only one particular species of absorber (chromophore), then the absorption coefficient can be defined in terms of the concentration of absorbers c (in M) and the specific absorption coefficient of

[1] A note on terminology: in this work 'particle' will be used as a general term to describe such scattering elements

that particular chromophore α (usually in $\mathrm{M}^{-1}\mathrm{cm}^{-1}$). In this case, $\mu_a = c\alpha$. It is more common for multiple chromophores to be present in a biological medium: in which case the total absorbance (for a given pathlength l) is given by the linear sum of the absorbances due to each of the N chromophores present:

$$A = \sum_{\mathrm{i}=1}^{\mathrm{N}} c_i \alpha_i l = (c_1\alpha_1 + c_2\alpha_2 + ... + c_N\alpha_N)l \tag{2.3}$$

In general, the specific absorption coefficient of a chromophore will be dependent on the wavelength of the incident light, and so the absorbance of a biological medium will also vary with wavelength.

2.1.2 Scattering

Optical scattering in tissue results from any process which may cause the direction in which a photon propagates to change. This could be due to interactions with individual particles in the biological medium, or due to structural features on a similar scale to the wavelength of the photon. If this process does not result in a reduction (or increase) in the energy of the photon then it is known as elastic scattering, and the direction of the photon will change whilst the wavelength remains the same (e.g. Rayleigh scattering). In the case of elastic scattering the properties of the medium can be described by: the scattering coefficient μ_s, which relates to the probability that scattering will occur; and the scattering phase function $p(\hat{s}, \hat{s'})$, which describes the probability that a photon travelling in the $\hat{s}$ direction will have a direction $\hat{s'}$ after a scattering event. The scattering coefficient is defined in a similar way to the absorption coefficient, where $\frac{1}{\mu_s}$ is the pathlength after which a fraction $\frac{1}{e}$ of the photons in a light beam will have undergone a scattering event.

Here the orientation of scatterers within a biological medium is assumed to be isotropic. Therefore the scattering phase function is only dependent on the difference in angle θ between the incoming photon's direction $\hat{s}$ and the scattered photon's direction $\hat{s'}$, where[2] $\cos\theta = \hat{s}.\hat{s'}$. If the scattering is sufficiently strong (i.e. μ_s is of the order of that found in biological tissue), so that multiple scattering dominates, the phase function $p(\theta)$ can be accurately described by a single parameter, the anisotropy factor g:

$$g =< \cos(\theta) >= \int_{4\pi} \cos(\theta) p(\theta) d\Omega \tag{2.4}$$

which is the average cosine of the scattering angle, and the integration is over all solid angles $d\Omega$. $-1 < g < 1$, where a value of $g = 0$ indicates isotropic scattering, whereas $g = 1$ indicates strongly forward scattering and $g = -1$ indicates strongly backwards scattering. Using this the reduced scattering coefficient for a medium can be defined:

$$\mu'_s = \mu_s(1 - g) \tag{2.5}$$

giving the transport mean free path $l' = \frac{1}{\mu'_s}$, which is the mean path-length which a photon must travel in the medium before its new direction is independent of its previous direction. In a similar way to absorption, the scattering properties of a biological medium may vary with the wavelength of the light.

[2] $\hat{s}$ and $\hat{s'}$ are unit vectors by definition.

2.1.3 Diffusion Equation for Light Propagation

The propagation of light through a turbid medium such as biological tissue can be described analytically by the Radiative Transfer Equation (RTE) [51]. This expresses the principle of conservation of energy in terms of the various sources and sinks present in a volume element of the medium for a given wavelength of light, taking into account the effects of scattering and absorption. Although it is possible to obtain a solution to this integro-differential equation using numerical methods, such an approach is generally computationally demanding [20]. By making some reasonable assumptions, as described below, the RTE can be simplified into a form which is easier to deal with. The RTE is expressed in terms of the radiance $L(\vec{r}, \hat{s}, t)$, which is the rate of energy flow per unit area at position $\vec{r}$ and time t and into the direction $\hat{s}$ (with units $\mathrm{Wm^{-2}sr^{-1}}$).

The diffusion approximation assumes that the radiance throughout the medium is nearly isotropic: if expressed in terms of a spherical harmonic series expansion, at most only the first two terms will remain (which correspond to an isotropic fluence rate term $\Phi(\vec{r}, t)$ and a weakly anisotropic flux vector term $\vec{J}(\vec{r}, t)$ [20]). This is valid when multiple scattering dominates the propagation of light in the medium. The small anisotropic correction term $\vec{J}(\vec{r}, t)$ is also assumed to vary slowly with time, relative to the mean time it takes for a photon to become 'fully' scattered $\frac{l'}{c}$[3]. Using these assumptions it is possible to integrate the RTE over all possible photon directions, converting the integro-differential equation into a differential equation which is significantly simpler. Integrating the radiance over all directions produces the fluence rate $\Phi(\vec{r}, t)$, which is proportional to the density of photons at a given point and time. A direction-weighted integration of the radiance gives rise to the flux vector term $\vec{J}(\vec{r}, t)$, whose direction gives the net flow of photons at a particular point, with a magnitude proportional to the pho-

[3] c is the optical speed in the medium

ton current. The time-dependent form of the diffusion equation (DE) is the result of this integration [84]:

$$\left[\frac{1}{c}\frac{\partial}{\partial t} - \nabla.(D\nabla) + \mu_a\right]\Phi(\vec{r},t) = q(\vec{r},t) \tag{2.6}$$

where D is the diffusion coefficient (dimensions of length) and $q(\vec{r},t)$ is a source term, describing the power per unit volume entering the medium at the point $\vec{r}$ at time t. By comparing the result of this integration with the definition of the diffusion equation, the diffusion coefficient is therefore equal to:

$$D = \frac{1}{3(\mu_a + \mu_s')} \tag{2.7}$$

where μ_s' is the reduced scattering coefficient (equation 2.5). In situations where these diffusion approximations are valid, the DE has an advantage over the RTE since exact analytical solutions can be found for simple geometries (given appropriate boundary conditions) [96].

2.2 Ultrasound-modulated Optics

2.2.1 Mechanisms of Ultrasound-modulation of Light

Incoherent Light (non-phase effects)

An ultrasound (US) wave passing through a medium will cause variations in the properties of the medium, as a result of local changes in pressure. The piezo-optic effect [11] describes how changes in pressure cause local changes in the refractive index of the medium:

$$\Delta n(\vec{r},t) = \frac{n_0 \eta P_a(\vec{r},t)}{\rho v_a^2} \tag{2.8}$$

where $P_a(\vec{r},t)$ is the applied pressure, η is the elasto-optical coefficient of the material, ρ is the density, v_a is the acoustic speed and n_0 is the refractive index in the absence of an applied pressure. We would expect that other optical properties of the material will change as a result of the changing local pressure and density: in particular the properties discussed in Section 2.1, the absorption coefficient and scattering coefficient.

Since the absorption coefficient is proportional to the concentration of absorbing particles in a material (equation 2.3), as the tissue is compressed under US the absorption will increase in those regions. The change in absorption induced by US is [78]:

$$\Delta \mu_a(\vec{r},t) = \mu_a \frac{P_a(\vec{r},t)}{\rho v_a^2} \tag{2.9}$$

The scattering coefficient will also be locally modulated by US. The concentration of scatterers will change in a similar way, but in addition to this, the scattering properties of a particle depend on the refractive index mis-

match encountered by light at the boundary of the scatterer. According to Mie theory [17] the quality factor of a scatterer Q is a function of the ratio of the refractive index inside the scattering particle to the refractive index of the surrounding medium. The scattering coefficient μ_s of a population of these scatterers is proportional to the quality factor Q and the number density of scattering particles, and also depends on the size of the particles relative to the optical wavelength. The US-induced change in scattering is therefore dependent on these two effects combined, and to be fully described requires a solution based on Mie theory (although an approximate result has been given by Liu *et al.* [78]).

These mechanisms affect the way in which light propagates through tissue when US is applied. Changes in μ_a and μ_s together will change the mean free path of photons ($\frac{1}{\mu_a+\mu_s'}$), where it leaves the tissue and hence whether or not it hits a detector on the way out. Changes in the relative proportion of scattering and absorption events will alter the probability that a photon travelling along a particular path will leave the tissue without being absorbed, therefore modulating the amplitude of detected light with respect to time. Since these mechanisms only affect photons which pass through the focal region of the US, the modulated part of a detected signal contains information which derives only from the focal region: the photons passing through there have been 'tagged', while all other photons remain un-modulated [81].

Coherent Light (phase modulation)

So far we have only considered mechanisms for US-modulation of light (UL) which lead to a change in the amplitude of a light signal reaching a certain detection point. This does not require the incident light to be coherent, since we have not considered the phase of individual photons. These incoherent effects are in general small relative to the effect of US on the phase of photons passing through the focal region [134]. The relative phases of photons

arriving at the detector will create an interference pattern which will vary spatially across the detection surface, since the relative pathlengths of arriving photons will depend on detector position [109]. Any additional changes to the phase of photons as a result of US will alter the locations of constructive and destructive interference on the surface (i.e. the bright and dark spots on a speckle pattern). Methods for detecting this phase-modulated signal are discussed in Section 2.2.2.

Two mechanisms for US-modulation of the phase of photons are considered here. Firstly, changes in the refractive index of the medium will modulate the optical pathlength of photons between scattering events. If l_j is the physical pathlength between the $(j-1)^{th}$ scattering event and the j^{th} scattering event, then we can integrate the phase along this path due to a continuously varying refractive index (see figure 2.1). The phase change (relative to an un-modulated photon) due to this mechanism is then:

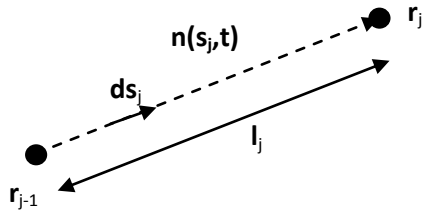

Figure 2.1: A continuously varying refractive index can be integrated along the photon path between successive scattering events to give the total phase change. Here ds_j represents an infinitesimal element along the path between the previous scatterer r_{j-1} and the next scatterer r_j, and $n(s_j, t)$ is the refractive index of the surrounding medium at point s_j along this path and time t.

$$\phi_{nj}(t) = \int_0^{l_j} k_0 \Delta n(s_j, t) ds_j \tag{2.10}$$

where k_0 is the optical wavenumber, ds_j is a length element along this j^{th} photon path and Δn is the US-induced change in refractive index at location s_j along the current path at time t (equation 2.8). Although these photon paths between scatterers are often assumed to be straight lines [78, 134], in reality the paths will bend when encountering a refractive index change [117].

The second mechanism is due to the movement of scattering particles as they oscillate under the applied US pressure. This will change the physical distance that a photon must travel between successive scattering events, since the particles have been displaced from their expected position. The displacement of a particle under US can be expressed as:

$$\vec{A}_a(\vec{r},t) = \frac{P_a(\vec{r},t)}{\rho v_a \omega_a}\hat{k_a} \tag{2.11}$$

where $\hat{k_a}$ is a unit vector in the direction of the US pressure gradient and ω_a is the acoustic angular frequency. This difference in pathlength can be interpreted as an US-induced phase shift. The phase shift in the j^{th} path of a photon due to the displacement of scatterers can be written as:

$$\phi_{dj}(t) = -n_0(\vec{k}_{j+1} - \vec{k}_j).\vec{A}_a(\vec{r}_j,t) \tag{2.12}$$

where $\vec{k}_j$ is the wavevector of the j^{th} light path and $\vec{r}_j$ is the location of the j^{th} scatterer. A full derivation is given in Appendix A.1.

2.2.2 Autocorrelation and Speckles

A detector positioned at the surface of a scattering medium will receive photons which have followed many different diffusive paths. Photons will have a range of phases ϕ due to the spread of pathlengths ($\exp[i\phi] = \exp[i(\omega t -$

$\sum \vec{k_j}.\vec{r_j})]$). As described in Section 2.2.1 these relative phases produce a speckle pattern of light and dark areas: this will be spatially random due to scattering. In the absence of UL, the phases will also be temporally random. However the phase changes induced by US vary across each acoustic cycle (see equations 2.10 and 2.12), and so the speckle pattern will acquire a time-varying component. The autocorrelation of the detected electric field at the surface can be used as a measure of this time-dependent component [70]:

$$G_1(\tau) = \langle E(t)E^*(t+\tau)\rangle = \int_{-\infty}^{\infty} E(t)E^*(t+\tau)dt \tag{2.13}$$

where τ is a time delay. The weak scattering approximation can be adopted, since the mean photon path is much longer than the optical wavelength, which itself is much larger than the acoustic amplitude[4]. Under this approximation the correlation between photons which have travelled paths of different lengths is negligible, and only photons which have the same path-length s (occuring with probability $p(s)$) contribute to the autocorrelation:

$$G_1(\tau) = \int_0^{\infty} p(s)\,\langle E(t)E^*(t+\tau)\rangle\,ds \tag{2.14}$$

Any temporally random phase changes produce a constant contribution to G_1; time-dependent phase changes can be seen as variations in $G_1(\tau)$, including UL and Brownian motion of scatterers [82]. To extract this modulated signal from the autocorrelation function we can use the Wiener-Khinchin theorem [14], which provides the spectral power I_n at an integer multiple of the acoustic frequency $n\omega_a$:

[4]i.e. the maximum displacement of scattering particles

$$I_n = \frac{1}{T_a} \int_0^{T_a} \cos(n\omega_a \tau) G_1(\tau) d\tau \tag{2.15}$$

where T_a is the acoustic period. The signal I_1 gives an estimate of the magnitude of US-modulation, or the AC signal. I_0 is the DC zero-frequency component, which in practice can be several order of magnitudes larger than I_1. A measure of the signal-to-noise ratio of an US-modulated optical technique is the modulation depth, $M = \frac{I_1}{I_0}$. This is used as an indicator of the magnitude of US-modulation, and determines the ability of a system to detect an UL signal behind a large background DC signal [62, 90].

2.3 Microbubbles

2.3.1 Ultrasound Contrast Agents

Medical ultrasound scanning produces an image by detecting backscattered sound from tissue. However this technique has often suffered from poor contrast between vasculature and surrounding tissue, since the acoustic properties of the two are very similar. This motivated the development of ultrasound contrast agents (UCAs) as a means of improving image quality: the most common types of UCA are based on microbubbles [123], which are introduced intravenously to improve the contrast of blood vessel images. There is a large body of work demonstrating the effectiveness of microbubbles in improving the contrast of different US imaging techniques [75].

Bubbles of gas are highly compressible compared with the surrounding tissue, and so will experience changes in volume in an applied US field [16]. This results in increased backscattering of sound, which contributes to a stronger detected signal. The backscattered signal also contains higher harmonic components of the driving US frequency [54,55,85], making this signal distinctive compared with the reflections from surrounding tissue [120]. The frequency response of a particular UCA depends on the size of the microbubble, and on the properties of any surfactant or polymer shell which may coat the bubble.

Microbubble UCAs are generally formed with a coating or shell, which may be a surfactant or other polymer [56], although it is possible to form a suspension of microbubbles by manually agitating or sonicating a solution [28]. Encapsulated bubbles will last longer before collapsing under surface tension and also generally have a more well-defined size distribution. The nature of the internal gas and the coating will also affect the rate of diffusion of gas across the shell, and hence the lifespan of the bubbles before

they fully dissolve into the blood [26].

2.3.2 Behaviour Under Ultrasound Exposure

The equation of motion of a bubble's response to US can be formulated in several different ways, depending on the underlying assumptions that are made about the bubble properties, the liquid and the US propagation [65]. In this section a selection of these models are reviewed, starting with the model containing the most simplifying assumptions. These equations of motion depend on physical properties of the microbubble (see figure 2.2) and other parameters of the system (see Section).

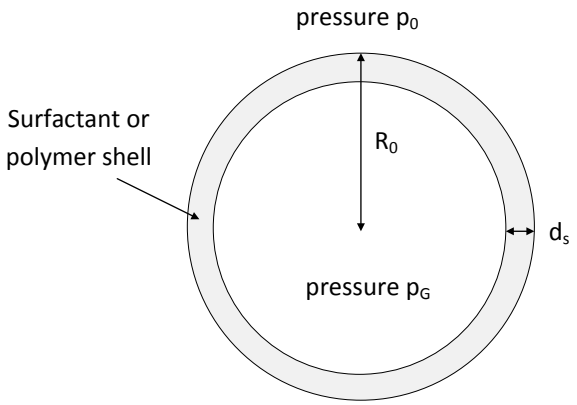

Figure 2.2: An encapsulated bubble at equilibrium. In the case of an uncoated bubble the surrounding surfactant or polymer layer is not present.

Rayleigh-Plesset Equation

The Rayleigh-Plesset equation is based on several assumptions:

- A single bubble is surrounded by an infinite volume of liquid.
- The bubble is spherical.

- The internal pressure P_G and temperature are spatially uniform.
- The radius of the bubble R_0 is much smaller than the acoustic wavelength, so that the acoustic pressure is uniform on all sides of the bubble.
- Gravitational forces within and acting on the bubble are ignored.
- The surrounding liquid and the shell are incompressible and irrotational.
- Diffusion of gas across the shell is ignored.

The equation of motion for a single uncoated bubble [97, 103] can be modified to take into account the properties of the coating, in which case the Rayleigh-Plesset equation can be written as:

$$\rho_L \left(R\ddot{R} + \frac{3}{2}\dot{R}^2 \right) + P_0 - P_a(t) - P_G(R) + \frac{4\dot{R}}{R}\eta_L = f_{ce} + f_{cd} \tag{2.16}$$

where $R(t)$ is the radius of the bubble at time t, $P_a(t)$ is the applied acoustic pressure and the other parameters are properties of the bubble or surrounding liquid (see table). f_{ce} and f_{cd} are terms describing the elastic and dissipative resistance of the bubble respectively, and the form of these is discussed in Section 2.3.3. $P_G(R)$ is the pressure of the gas inside the bubble, which is assumed to behave polytropically:

$$P_G(R) = \left(P_0 + \frac{2\sigma_0}{R_0} \right) \left(\frac{R_0}{R} \right)^{3k} \tag{2.17}$$

where k is the polytropic constant.

Herring-Trilling Equation

As the US pressure driving the bubble oscillations is increased, the assumption of the previous model which first becomes problematic is that the liquid is incompressible: this in turn implies that the speed of sound in the medium is infinite, since the density of the liquid is assumed to be uniform. As the velocity of the bubble wall $\dot{R}$ increases, this limits the validity of the Rayleigh-Plesset equation. At larger acoustic Mach numbers, where $M = \dot{R}/v_a$, the model can be improved by assuming a constant finite speed of sound, which derives from the state equation $\frac{\partial P}{\partial \rho} = v_a^2$ [94]. The Herring-Trilling equation [43,129] makes use of this, and also takes into account the energy stored in compressing the fluid:

$$R\dot{R}\frac{d\dot{R}}{dR}(1-2M) + \frac{3}{2}\dot{R}^2(1-4M) = \frac{RM}{\rho_L}\frac{dP_L}{dR} + \frac{P_\infty - P_L}{\rho_0} \tag{2.18}$$

where P_∞ is the pressure of the liquid at an infinite distance from the bubble, and P_L is the pressure at the bubble surface. In the case where the Mach number is very small and the bubble is simply an empty cavity (having no surface tension), the pressure at the surface $P_L = 0$ and equation 2.18 reduces to a form of the Rayleigh-Plesset equation [94]. This suggests that equation 2.16 is a reasonable approximation only under low excitation pressures, where the bubble wall velocity $\dot{R}$ is negligible compared with the speed of sound v_a.

Keller-Miksis Equation

The formulation by Keller and Miksis [59] takes into account the acoustic pressure radiated by an oscillating bubble, and is based on the Navier-Stokes fluid equations. It assumes a large but finite acoustic speed, and allows for small changes in fluid density as a result of compression. This results in the differential equation:

$$\left(1-\frac{\dot{R}}{v_a}\right)R\ddot{R}+\frac{3}{2}\dot{R}^2\left(1-\frac{\dot{R}}{3v_a}\right)=\left(1+\frac{\dot{R}}{v_a}\right)\frac{P}{\rho_L}+\frac{R}{\rho_L v_a}\frac{dP}{dt} \tag{2.19}$$

where

$$P=\left(P_0+\frac{2\sigma}{R_0}\right)\left(\frac{R_0}{R}\right)^{3k}-P_0-\frac{2\sigma}{R}-\frac{4\eta_L}{R}\dot{R}-P_a(t) \tag{2.20}$$

This model can be extended with a new formulation for the pressure inside the bubble [101], and the damping of bubble oscillations by thermal effects can also be considered [100]. For the application presented in this thesis these effects will not be significant since the acoustic pressures are low, so this model is only briefly mentioned here for reasons of completeness.

2.3.3 Effect of Bubble Coating

If a bubble is encapsulated by some kind of surfactant or polymer this will have an effect on its dynamics, compared with a bubble which is simply an empty or gas-filled cavity in a liquid. This may alter the amplitude of bubble oscillations and their US frequency response. Depending on the nature of the coating, this can be incorporated into the equations of motion presented in Section 2.3.2 in several ways, as will be discussed in this section.

Polymer Shell (Hoff model)

For a microbubble coated with a solid polymer shell, a model developed by Church [13] and then reduced to the case of an infinitely thin shell by Hoff *et al.* [45] can be used to describe the elastic and dissipative resistance terms f_{ce} and f_{cd}. This relies on estimations of several parameters of the shell, such as its shear modulus and shear viscosity. Using these parameters:

$$f_{ce} = -\frac{12G_s d_s R_0^2}{R^3}\left(1-\frac{R_0}{R}\right)-\frac{2\sigma_0}{R_0} \tag{2.21}$$

$$f_{cd} = -\frac{12\eta_s d_s R_0^2 \dot{R}}{R^4} \tag{2.22}$$

This model assumes that the values of these shell parameters are constant, whereas experimental evaluations [126] suggest that these quantities will vary with the size of the bubble as it oscillates and also with time. This model therefore diverges from these observed results, apart from in the case of low amplitude oscillations such as those considered here.

Surfactant Shell

The stability of manufactured microbubbles is often controlled by the addition of surfactants, which form a thin coating on the surface. This can reduce the surface tension at the bubble wall, and have an effect on the rate at which bubbles will naturally collapse [122]. It will also add resistance to bubble oscillations, as described by the following model [126]:

$$f_{ce} = -\frac{2}{R}\left[\sigma+\frac{K\Gamma_0^{\chi+1}}{\chi+1}\left(1-\left(\frac{R_0}{R}\right)^{2(\chi+1)}\right)\right] \tag{2.23}$$

$$f_{cd} = -\frac{4\dot{R}}{R^2}\eta_{so}\exp\left(\frac{ZR_\chi^2}{R^2-R_\chi^2}\right) \tag{2.24}$$

where R_χ is the minimum bubble radius, below which the coating will buckle and surface tension will be disrupted, and $\Gamma_0, \chi, K, \eta_{so}$ and Z are properties of the surfactant coating. This model is essentially equivalent to the Hoff model for the relatively small amplitude oscillations considered here, hence the Hoff model is used for the sake of simplicity of implementation.

Chapter Summary

- The theory of light propagation in biological and turbid media has been discussed, which considers the absorption and scattering properties of the medium.
- The mechanisms by which US can modulate the optical properties of a medium have been introduced, in particular the displacement of scattering particles and changes in refractive index.
- The Rayleigh-Plesset, Herring-Trilling and Keller-Miksis equations for bubble dynamics under US have been reviewed, including additional terms which account for a coating around the bubble.

Chapter 3

Analytical Modelling of Microbubble Interactions with Light and Ultrasound

In order to investigate the effectiveness of microbubbles as a contrast agent for ultrasound-modulated biomedical optics this thesis makes use of mathematical and computational modelling techniques. In chapter 4 Monte Carlo models are used to simulate the propagation of light through biological tissue which is also insonified by ultrasound. When microbubbles are included in this model it is necessary to consider how a gas-filled shell surrounded by fluid, such as a bubble in a blood vessel, will behave under application of an external ultrasound field. In this chapter an analytical model for the dynamic response of microbubbles to ultrasound is described. The process for solving this equation of motion numerically and using analytical approximations is explained, and a novel solution which considers terms up to second order is derived.

In addition to the interactions between bubbles and ultrasound, the scattering of light from microbubbles needs to be considered in these Monte Carlo

simulations. Section 3.2 applies Mie theory to the scattering of light from a bubble within a biological medium in order to derive a theoretical description of the optical properties of a microbubble. In the final section of this chapter a novel hypothesis is presented for a mechanism by which insonified microbubbles may enhance acousto-optic modulation. This is based on the pressure which is radiated from the surface of an oscillating bubble, and is investigated further in Chapter 4.

3.1 Dynamic Response of Bubbles

To understand the effect of microbubbles on an US-modulated optical signal, we first need to analyse the response of a bubble to focused US. The analytical work in this section concentrates on the Rayleigh-Plesset equation of motion (see Section 2.3.2), which is valid provided that the applied US pressure is low[1]: at higher pressures disruption of the spherical structure is known to occur, and eventually bubbles will be destroyed [124]. This equation of motion is a non-linear differential equation in terms of the bubble radius $R(t)$, and as such no closed analytical solution exists [101]. Solutions generally involve numerical methods [57], or approximations limiting the response of a bubble to a few harmonic components [99].

In the simplest case of an uncoated bubble, an analytical solution has been derived by assuming that the bubble response contains a single harmonic component at the applied US frequency. This was first investigated by Minnaert [86], who showed that 'musical' bubbles are partly responsible for the sound of running water, and later by Plesset and Prosperetti [97]. Similar linear analysis has provided a solution for a bubble coated with surfactant [126] (using the model described in Section 2.3.3). Further work by Church [13] introduced weakly non-linear analysis, which was used to solve a

[1]In this work, pressures are restricted to below 0.2 MPa for US of frequency 1 MHz

modified Rayleigh-Plesset equation considering both linear and second order harmonic components at frequencies of ω_a and $2\omega_a$. Similar analysis is used in this section to solve the Rayleigh-Plesset equation combined with the Hoff model (Section 2.3.3) for a solid polymer-coated bubble, which matches the types of microbubbles used in the later experimental work of Chapter 6.

3.1.1 Numerical Solutions

To accurately describe the non-linear behaviour of a microbubble under US generally requires the equation of motion to be solved numerically: as the driving US pressure is increased, the non-linear components of microbubble oscillations become dominant. The Rayleigh-Plesset equation (2.16) is combined with the Hoff model (2.21 and 2.22) and solved using Mathematica and Matlab. This will provide a 'gold standard' result for the time series of a microbubble oscillation $R(t)$, which can be compared with the analytical approximations derived later. The applied US pressure is a continuous wave (CW) with a single frequency component:

$$P_a(\vec{r},t) = -P_a \cos(\vec{k_a}.\vec{r} - \omega_a t) \tag{3.1}$$

The parameters which describe the shell properties are taken from the values given in these references [35, 126] for SonoVue® phospholipid coated microbubbles. These parameters are found by fitting a model to experimentally measured oscillations of microbubbles: since the response is in the same low amplitude, stable regime as that expected here these properties are assumed to be a good approximation to the parameters for Expancel^{TM} microbubbles. The surrounding fluid was assumed to be water (see table 3.1 for a full list of the parameters). Figure 3.1 shows the response of a single coated bubble to US: at low applied pressures the behaviour is linear and is dominated by the fundamental frequency component ω_a. As the pressure

is increased higher order frequency components become visible. This can be more clearly seen in figure 3.2, which shows the frequency response of the bubble for 3 different values of P_a. At the lowest pressure a single peak is seen in the response at around 1.6 MHz, which agrees closely with the expected linear resonance frequency (see Section 3.1.2). A second peak clearly appears when the pressure is increased to 100 kPa, which corresponds to the first subharmonic with a frequency of around 0.8 MHz.

Description	Symbol	Value
Equilibrium bubble radius	R_0	2.25 μm
Density of surrounding fluid	ρ_L	1000 kg m^{-3}
Viscosity of surrounding fluid	η_L	1.5 mPa s
Equilibrium surface tension	σ_0	0.05 N m^{-1}
Effective thickness of shell	d_s	1 nm
Effective shear modulus	G_s	20 MPa
Effective shear viscosity	η_s	1.5 Pa s
Ambient surrounding pressure	P_0	100 kPa
Polytropic constant of gas	k	1

Table 3.1: Values of parameters used in the Rayleigh-Plesset equation of motion for a bubble, with shell terms based on the Hoff model.

These numerical solutions for bubble time series are the optimal choice when computational time is not an issue. However in the case where we would like to simulate large scale systems with many microbubbles present, calculation speed becomes limiting and it is necessary to use simpler solutions such as those that follow.

3.1.2 Linear Approximation

The simplest forms of bubble oscillations are those driven by low US pressures. In this case we can assume that the amplitude of oscillations is small, so that $R(t) = R_0[1 + z(t)]$. The equation of motion can then be re-written in terms of $z(t)$, and if we assume that $z(t) \ll 1$ we can discard all terms of

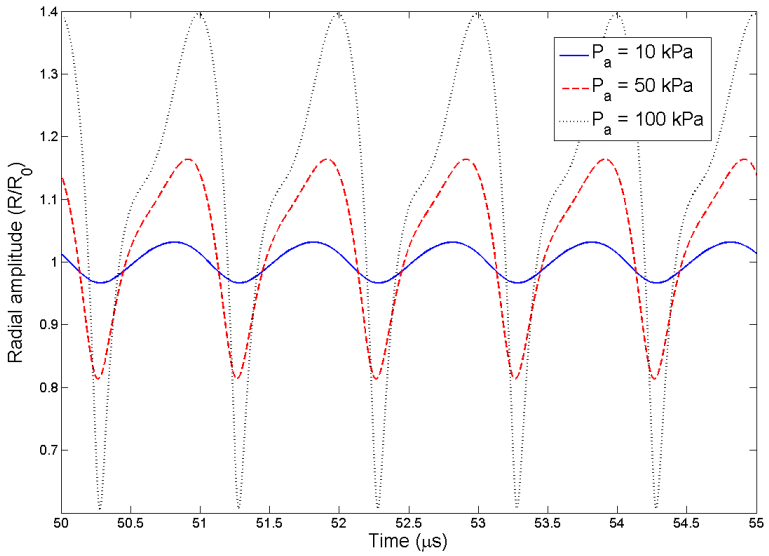

Figure 3.1: Numerical solutions for response of a coated bubble to varying US pressure at $f_a = 1$ MHz. The first 50 μs are discarded to ensure that any transient solution is not included.

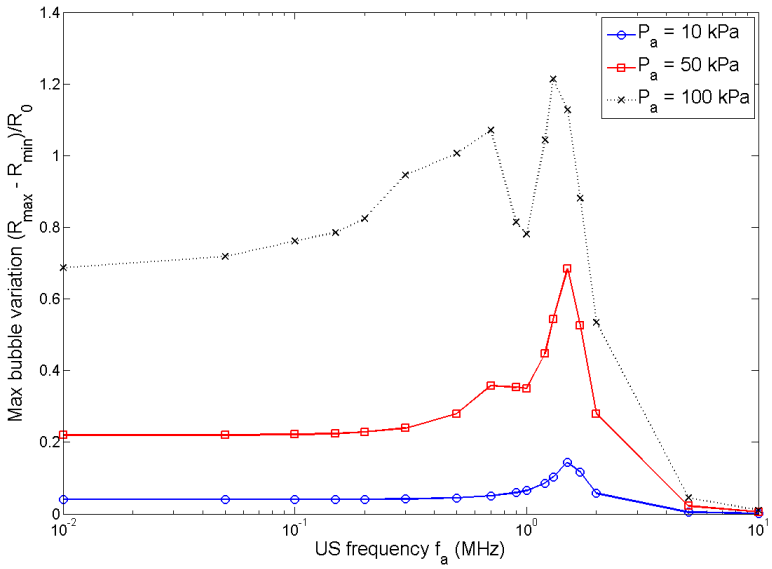

Figure 3.2: Numerical solutions for the frequency response of a bubble at low, moderate and high US pressures. Response is calculated as the maximum variation in bubble radius (normalised by the equilibrium bubble radius R_0).

order z^2 or higher. Appendix A.2 shows that the equation of motion is then analagous to a driven simple harmonic oscillator with damping:

$$a\ddot{z} + b\dot{z} + cz = P_a(t) \tag{3.2}$$

where a, b and c are coefficients that depend on the parameters of the bubble and surrounding liquid. The solution to this linear equation of motion is therefore analytically simple:

$$R(t) = R_0\left[1 + z(t)\right] = R_0\left[1 + \frac{P_a}{\beta}\sin(\vec{k}_a.\vec{r} - \omega_a t + \xi)\right] \tag{3.3}$$

where β is the response function, which describes the frequency response of the oscillator and is a function of ω_a. ξ is a phase offset relative to the driving US. These functions take the form:

$$\beta = \sqrt{\omega_a^2\left(4\eta_L + 12\frac{d_s\eta_s}{R_0}\right)^2 + \left(3P_0 + \frac{6\sigma_0}{R_0} + 12\frac{G_s d_s}{R_0} - \rho_L R_0^2\omega_a^2\right)^2} \tag{3.4}$$

$$\xi = \arctan\left(\omega_a \frac{4\eta_L + 12 d_s\eta_s R_0^{-1}}{\rho_L R_0^2\omega_a^2 - 3P_0 - 6\sigma_0 R_0^{-1} - 12 G_s d_s R_0^{-1}}\right) \tag{3.5}$$

Figure 3.3 compares the linear model with the full numerical solution for a bubble driven at low pressure and a bubble driven with a higher pressure: this demonstrates that the linear model is appropriate for describing low amplitude oscillations, but diverges from the non-linear solution when bubble oscillations are large. We can quantify the accuracy of this linear model

by calculating the root mean square (RMS) error, i.e. the RMS difference between the linear model and the numerical solution. Figure 3.4 shows that the linear method loses accuracy at a steady rate as the applied US pressure is increased.

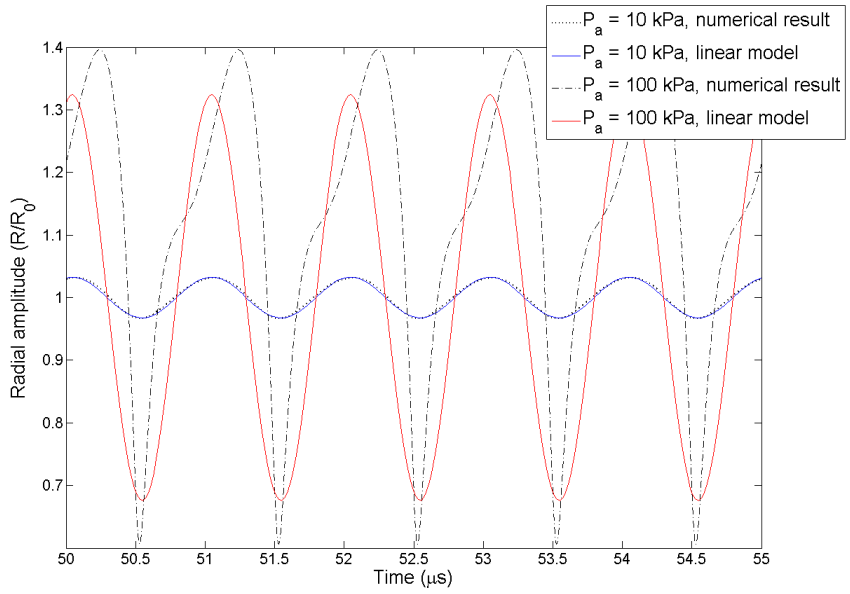

Figure 3.3: Comparing the solution to the linearised Rayleigh-Plesset equation with the all-order numerical result at low and high applied US pressures.

3.1.3 Second Order Approximation

While the linear approximation provides an accurate description when the applied US pressure is low, the results deviate progressively further from the numerical solution as P_a is increased, since non-linear components of the oscillation become significant [99]. This suggests that a model which takes into account higher order terms of the equation of motion will be more appropriate for describing bubble oscillations under higher US pressures. To derive a quadratic solution to the Rayleigh-Plesset equation of motion, we assume a solution which contains a component with frequency $2\omega_a$:

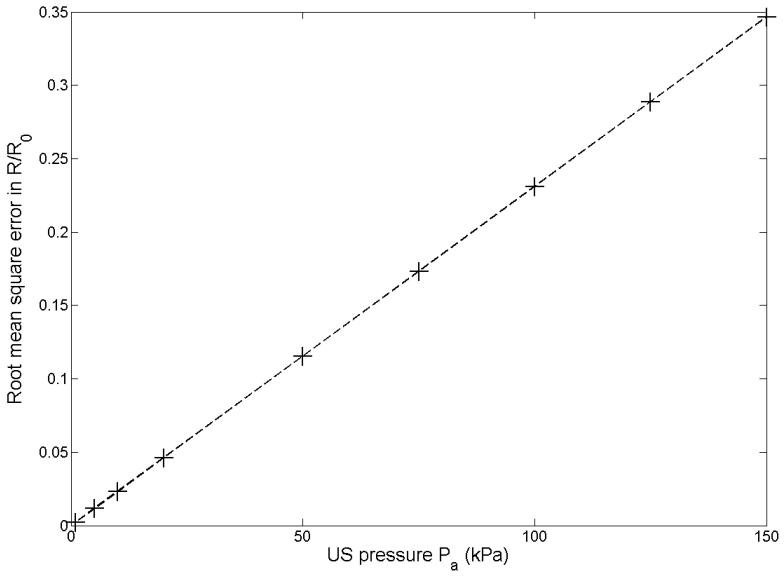

Figure 3.4: Root mean square error in the bubble radius from the linear model compared with the numerical solution as a function of US pressure (with $f_a = 1$ MHz).

$$
\begin{aligned}
&R(t) \\
&= R_0 \left[1 + z(t)\right] \\
&= R_0 \left[1 + X_0 + X_1 e^{i\omega_a t} + X_1^* e^{-i\omega_a t} + X_2 e^{2i\omega_a t} + X_2^* e^{-2i\omega_a t}\right]
\end{aligned} \tag{3.6}
$$

where the response functions X_0, X_1 and X_2 depend on the applied US frequency. X_1 and X_2 are complex, so that they represent both the magnitude of the bubble response and its phase relative to the applied US. A weakly non-linear analysis similar to Church's approach [13] can be applied, which assumes that $1 > |X_1| > |X_2| \approx X_0$ (i.e. that the 1st order term is dominant) and that terms of order z^3 are negligible. The equation of motion can then be expressed in terms of $z(t)$, with the general form of a harmonic oscillator with some higher order terms:

$$
a\ddot{z} + b\dot{z} + cz = P_a(t) + dz^2 + ez\dot{z} - az\ddot{z} - \frac{3}{2}a\dot{z}^2 \tag{3.7}
$$

The full analysis is given in Appendix A.3, including expressions for the response functions. Figure 3.5 shows the result of this model for a driving pressure of $P_a = 100$ kPa.

Although the RMS error of this second order model also increases rapidly as the driving US pressure is increased (see figure 3.6), it more accurately represents the mean bubble radius. This is because it takes into account a shift in the equilibrium size of the bubble as a result of insonification, and also because the non-linear components of a bubble's oscillation do not average out to zero over one acoustic cycle (since each non-linear component will in general not be in phase with the linear component). Figure 3.7 shows the time-average of the bubble radius $R(t)$ for the linear, quadratic and numerical models.

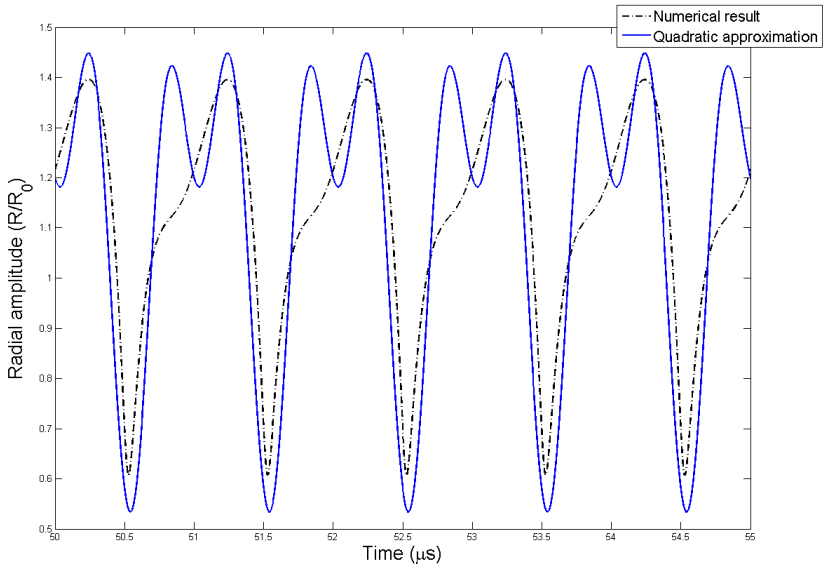

Figure 3.5: Second order model for bubble oscillations compared with numerical result with $P_a = 100$ kPa (and $f_a = 1$ MHz).

These analytical approximations require significantly less computational time to calculate than the full-order numerical solution. In the Chapters which follow large scale Monte Carlo models of microbubbles, light and US are investigated: this requires the interactions between millions of photons and bubbles to be modelled, and so these approximations may be useful in increasing the computational efficiency of such a model. In the final section of this Chapter an analytical model for the interaction between light and microbubbles is presented, which relies on these predictions of the radii of insonified bubbles at given temporal and spatial coordinates.

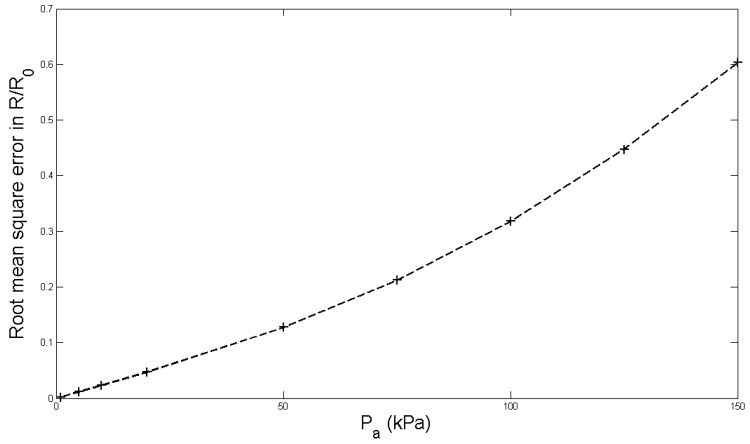

Figure 3.6: Root mean square error in the bubble radius from the second order model compared with the numerical solution as a function of US pressure (with $f_a = 1$ MHz).

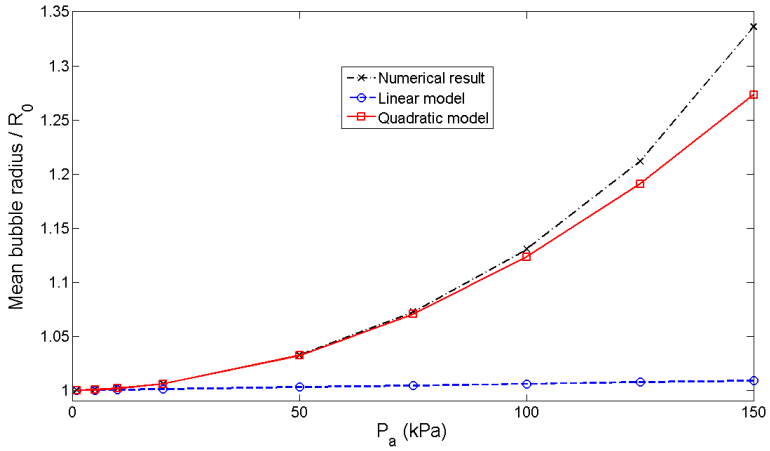

Figure 3.7: Mean bubble radius (averaged over one acoustic cycle) as predicted by the linear, quadratic and numerical models (with $f_a = 1$ MHz).

3.2 Optical Scattering from Microbubbles

The scattering of light by a microbubble suspension has been used as an indicator of bubble size [38]: this makes use of the fact that an oscillating bubble will have optical properties that vary with radius. Although the use of microbubbles has been demonstrated in US-modulated optical detection (e.g. US-modulated fluorescence [139]), the mechanisms for microbubble contrast enhancement of an US-modulated optical signal have not previously been fully analysed. Theoretical results exist which describe the scattering of light by a sphere, the most complete being Mie theory [17]. Since this result is analytically complex, an approximation to the scattering phase function was first proposed by Henyey and Greenstein in an astrophysics context [42]. This result is regularly used in the field of biomedical optics due to its simplicity, although more recently alternatives have been suggested [77]. Further approximations which rely on geometrical optics (i.e. the limit that the optical wavelength is small compared with the particle size) have also been proposed [18,33]; when the particle is much smaller than the wavelength, the Rayleigh scattering approximation may be used [10].

3.2.1 Using Mie Theory

The scattering of light by spherical particles can be treated analytically by solving Maxwell's equations of electromagnetism: such a solution is generally known as Mie theory or the Mie solution [17]. This can be used to calculate the scattering cross section of a particle as well as the phase function which describes the angular distribution of scattered optical power. In general the solution depends only on the particle size parameter $x = k_0 R$, where k_0 is the wavelength and R is the radius, and the refractive index mismatch at the interface between the particle and its surrounding medium is $m = n_p/n_0$.

For an oscillating microbubble this radius is a function of time. In addi-

tion, as the pressure inside the bubble changes during expansion and contraction, the refractive index of the gas will change as a result of density changes. The Lorentz-Lorenz formula [11] states that the following relationship holds between the pressure P of a gas, the temperature T and its refractive index n:

$$A \approx \frac{RT(n^2 - 1)}{3P} \tag{3.8}$$

where A is the molar refractivity of the gas in question (with dimensions of molar volume), R is the molar gas constant and the approximation is valid for $n^2 \approx 1$. Assuming values for n, P and T at standard temperature and pressure gives an estimate for A, which is used to calculate n as a function of changing pressure. The pressure inside the bubble is related to bubble radius according to equation 2.17. The scattering phase function according to the Mie result is shown in figure 3.8 for a bubble at equilibrium and after expanding to twice its equlibrium radius. A Matlab-based algorithm [80] was used to calculate the Mie results.

3.2.2 Approximations to Mie Theory

To develop a simpler model for optical scattering from microbubbles, which is more appropriate for large scale simulations, we can adopt an approximation which derives from geometrical optics. In the case where the wavelength of light is small compared with the size of the bubble, it is expected that the scattering probability will be proportional to the cross-sectional area of the bubble which is presented to photons passing through the suspension. This suggests that the optical scattering coefficient due to a population of microbubbles can be approximated as [18]:

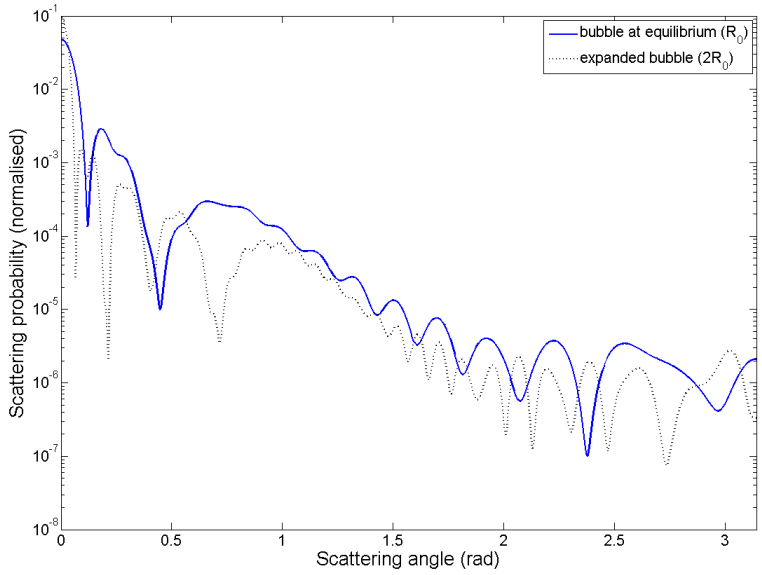

Figure 3.8: Scattering phase function calculated from Mie theory.

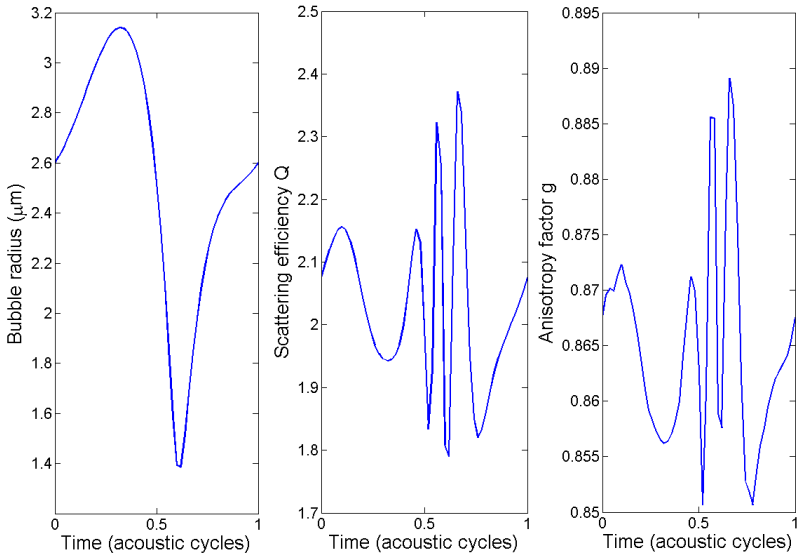

Figure 3.9: Variations of scattering efficiency Q and anisotropy factor g as a microbubble oscillates under US ($P_a = 100$ kPa, $f_a = 1$ MHz).

$$\mu_{s,b} = \pi R(t)^2 \rho_b Q \tag{3.9}$$

where ρ_b is the density of microbubbles (in mm^{-3}) and Q is the quality factor of the scattering, which takes into account the discrepancy between the physical cross-section of a bubble and the effective cross-sectional area for scattering which a photon 'sees'. It is the ratio of the actual scattering cross-section to the scattering cross-section which would be expected from geometrical optics. In the limit of a very large particle $Q \approx 2$ [17]. In general Q can be found from Mie theory, and will vary slightly with particle size (see figure 3.9).

The scattering phase function, which according to Mie theory is not a trivial function of scattering angle (see figure 3.8), can also be represented by a simpler approximation. The Henyey-Greenstein phase function [42] is commonly used since it has a simple analytical form, which is especially convenient for large scale computational work such as that presented in Chapter 4. This requires just one parameter to characterise the angular distribution, which is the anisotropy factor g (the average cosine of the scattering angle). The Henyey-Greenstein function can be written as:

$$p_{HG}(\cos\theta, \cos(\theta + d\theta)) = \frac{1 - g^2}{2(1 + g^2 - 2g\cos\theta)^{3/2}} \tag{3.10}$$

where p_{HG} is the probability that a photon will be scattered with a deflection angle between θ and $d\theta$ (in the limit where $d\theta$ is infinitesimally small). Figure 3.10 compares the Mie result with the Henyey-Greenstein approximation using the average cosine value of the Mie result as the value of g.

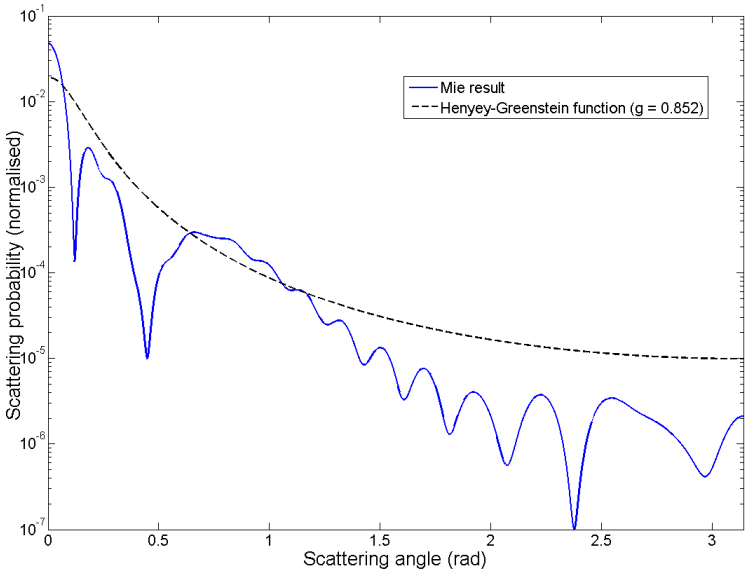

Figure 3.10: Mie result for the scattering phase function compared with the Henyey-Greenstein phase function with an equivalent anisotropy g (bubble size $R = 2.25$ μm and $\lambda_0 = 500$ nm).

3.3 Optical Phase Shift due to Microbubbles

Section 2.2.1 explains the mechanism by which US pressure leads to changes in the refractive index of tissue, which affects the optical pathlengths in that medium. In a similar way, the pressure changes resulting from the presence of microbubbles would be expected to have an effect on the refractive index of the liquid they are suspended in. An oscillating microbubble has been shown to radiate pressure from its surface [126, 130]. In this analysis it is assumed that there is no interaction between the radiated pressure fields of neighbouring bubbles: this is true provided that the bubble density is low, such that the distance between bubbles is greater than a few bubble diameters [30], otherwise secondary radiation forces must be considered. Appendix A.5 gives more details on the magnitudes of bubble density which satisfy this assumption, and shows that for the densities used in the proceeding Chapters this assumption is appropriate.

3.3.1 Radiated Pressure

The pressure field radiated by an oscillating microbubble is given by [126]:

$$P_{rad}(r,t) = \rho_L \left(\frac{1}{r}(R^2\ddot{R} + 2R\dot{R}^2) - \frac{1}{2r^4}R^4\dot{R}^2 \right) \tag{3.11}$$

where r is the radial distance from the centre of the bubble, and $R = R(t)$. Figure 3.12 shows a graphical representation of this radiated pressure field around a bubble, including the incoming and outgoing paths of a photon scattering from the bubble. A photon travelling along this path will experience a phase shift relative to a photon in the absence of this radiated pressure. Using equation 2.10 this phase shift can be integrated along the incoming and outgoing photon paths to give the total additional phase of the photon. The limits of this integration are illustrated by figure 3.11, where

R_0 is the equilibrium radius of the bubble. We assume here that bubbles are small enough to be considered as point scatterers, so that a photon always approaches and recedes along the radial direction. In the case of microbubbles the size of the particle (1000 nm) is not insignificant compared with the wavelength of near infrared light (800 nm). However as they are similar in magnitude, as has already been discussed in section 3.2, the scattering from the surface of the bubble is not dependent on the angle of incidence of the photon relative to the bubble surface as it would be in the case of scattering from a large particle. $\phi_{r,j}$, the radiated pressure phase shift induced at the j^{th} scattering event between a bubble and a photon, is then:

$$\begin{aligned} \phi_{r,j} = & \int_{l_j}^{R_0} k_0 \Delta n(r,t)(-dr) + \int_{R_0}^{l_{j+1}} k_0 \Delta n(r,t) dr \\ = & \frac{n_0 k_0 \eta}{\rho_L v_a^2} \left[\int_{R_0}^{l_j} P_{rad}(r,t) dr + \int_{R_0}^{l_{j+1}} P_{rad}(r,t) dr \right] \end{aligned} \tag{3.12}$$

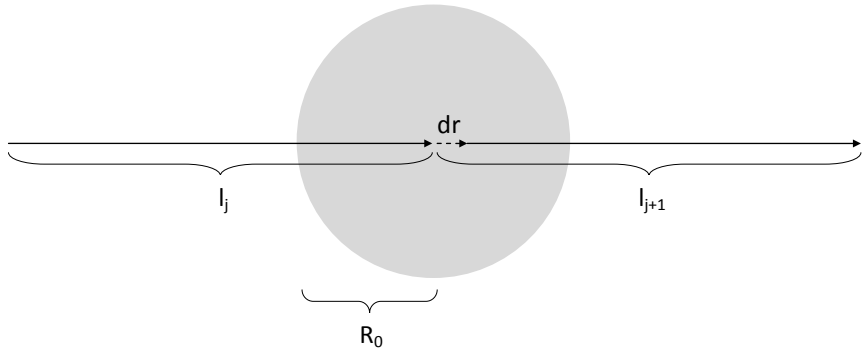

Figure 3.11: The radiated pressure is integrated along the length of the approaching photon path l_j and the receeding path l_{j+1}. Within the bubble wall the radiated pressure is assumed to be zero.

Here equation 2.8 is used to express the local change in refractive index Δn in terms of P_{rad}. As the bubble population is assumed not to be dense,

and the radiated pressure falls rapidly with distance from a bubble, the phase shift due to the pressure radiated by other bubbles can be ignored; when a scattering event occurs a photon necessarily passes very close to a bubble, and so the effect of the radiated pressure field will be greatest in these cases.

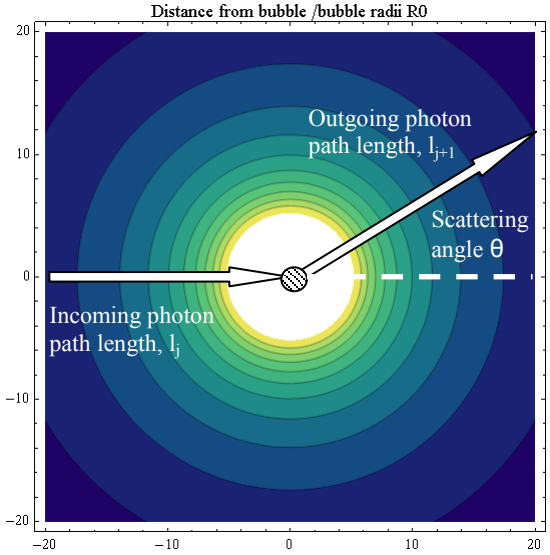

Figure 3.12: The radiated pressure is indicated by the contrast, with the pressure at its highest close to the bubble surface.

3.3.2 Linearised Result

In general, the photon phase shift can be found from equation 3.12 by integrating the radiated pressure P_{rad}, which is itself a function of the bubble radius R, the bubble velocity $\dot{R}$ and the bubble acceleration $\ddot{R}$. Several models for calculating the radius of a bubble as a function of time have already been described here: a numerical method, a linear analytical solution and a quadratic analytical solution. In this section an analytical expression for the radiated pressure phase shift $\phi_{r,j}$ will be derived in the case of linear microbubble oscillations.

Firstly, the radiated pressure P_{rad} can be expressed in terms of the non-dimensional bubble radius change from equilibrium $z(t)$, where $R(t) = R_0(1+z(t))$. After inserting this expression into equation 3.11, only terms of first order in z are retained. The bubble velocity is therefore $\dot{R} = R_0\dot{z}$ and the acceleration $\ddot{R} = R_0\ddot{z}$. The linearised form of P_{rad} is:

$$\begin{aligned} P_{rad}(r,t) &= \rho_L \left(\frac{R_0^3}{r} \left[(1+z)^2 \ddot{z} + 2(1+z)\dot{z}^2 \right] - \frac{R_0^6}{2r^4}(1+z)^4 \dot{z}^2 \right) \\ &= \frac{\rho_L R_0^3}{r} \ddot{z} + O(z^2) \end{aligned} \tag{3.13}$$

The linear solution to the Rayleigh-Plesset equation for $z(t)$ is given in equation 3.3. This is now substituted into the above expression to give the linear form of the radiated pressure:

$$P_{rad}(r,t) = -\frac{1}{r} \frac{\rho_L R_0^3 \omega_a^2 P_a}{\beta} \sin(\vec{k}_a.\vec{r} - \omega_a t + \xi) \tag{3.14}$$

Integrating equation 3.12 with this linear form of P_{rad} gives:

$$\phi_{r,j} = \frac{n_0 k_0 \eta k_a^2 R_0^3 P_a}{\beta} \sin(\vec{k}_a.\vec{r}_j - \omega_a t + \xi) \left[\ln\left(\frac{R_0}{l_j}\right) + \ln\left(\frac{R_0}{l_{j+1}}\right) \right] \tag{3.15}$$

This is the additional phase shift of a photon during collision with a bubble as a result of the radiated pressure surrounding the bubble. It is therefore a function of the bubble position $\vec{r}_j$, the incoming photon pathlength l_j and the outgoing pathlength l_{j+1}. Like other mechanisms of UL, such as refractive index modulation and scatterer displacement [134], the phase shift due to microbubbles is proportional to the applied US pressure in this linear regime. It is also at a maximum when the bubble is at resonance, i.e. the US

frequency matches the resonant frequency of the bubble, as shown by figure 3.13.

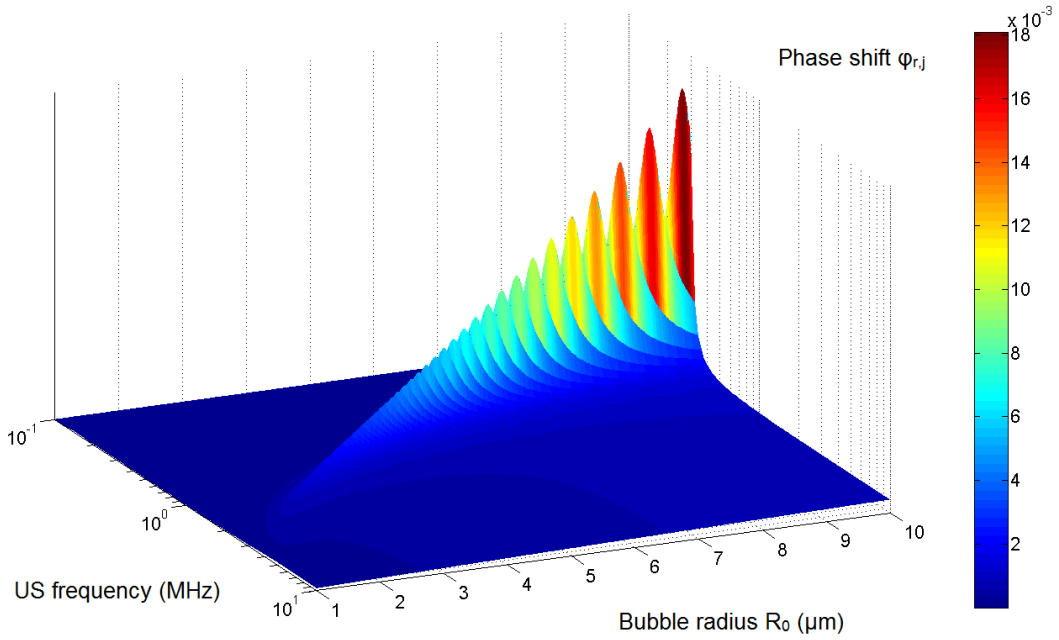

Figure 3.13: Analytical result for the phase shift of a photon due to the pressure radiated by a microbubble as a function of the microbubble size and driving US frequency. For comparative purposes, the mean phase shift experienced by a photon in the absence of US is of the order of 10^{-2} for the parameters used in these simulations (see Chapter 4).

There are of course several simplifying assumptions in this model which should be emphasised. Firstly that the bubble is a point-like scatterer, and therefore that photons can be considered to approach and recede along a direction radial to the bubble. Variations in the field of an electromagnetic wave as it approaches the liquid/gas interface are ignored, as they would require a solution to Maxwell's equations. This is likely to be the most significant assumption, since the radius of a microbubble (several μm) is not

negligible compared with the wavelengths of light used here (around 500 nm). In order to provide more confidence in this model, experimental validation would be required, but it is presented here as a discussion on the mechanisms which are likely to be involved in the US-modulation of light in a medium containing microbubbles.

Chapter Summary

- Numerical solutions to the Rayleigh-Plesset equation describing a bubble under US show that the bubble response is dominated by a single frequency at low pressures (10 kPa).
- At higher pressures (100 kPa or above) higher order harmonics are significant.
- Analytical solutions for linear oscillations and oscillations containing second order components are derived. Although the RMSE of both solutions are of a similar magnitude, the quadratic model predicts the mean bubble radius more accurately at higher pressures (above 20 kPa).
- These analytical solutions require significantly less computational time to calculate, and so may be useful in Monte Carlo models of large scale systems containing microbubbles, light and US such as those investigated in the following Chapters.
- Scattering of light from microbubbles is modelled by fitting a Henyey-Greenstein angular distribution to the results calculated from Mie Theory. The instantaneous radius of an insonified bubble is used to predict its optical scattering efficiency.
- A mechanism for modulating the phase of coherent light with microbubbles is proposed, leading to amplification of the AO effect. This considers the refractive index changes caused by pressure radiated from the surface of an oscillating bubble.

Chapter 4

Monte Carlo Modelling of Light Transport with Microbubbles

Monte Carlo (MC) methods were first used in the field of biomedical optics to predict dose distributions in photodynamic therapy [137]. This introduces the idea of simulating computationally the paths of weighted photons through a medium: i.e. what is referred to as one photon in the simulation corresponds physically to many photons, and its weight indicates the fraction of those photons which have not yet been absorbed by the medium. Grouping photons together into photon packets[1] improves statistical accuracy for a given amount of computational time, compared with the alternative of generating each photon's path individually, since more photons overall can be simulated.

This method was extended to consider multi-layered tissue [132], where each layer is semi-infinite and may have different optical scattering and absorption properties. Simulating large numbers of photons with highly scattered paths is computationally intensive. However the process lends itself naturally to parallelisation, for example on a graphics processing unit

[1] A note on terminology: from here onwards 'photon' is used in place of 'photon packet'.

(GPU) [1]. This has been shown to reduce simulation times by at least three orders of magnitude [2]. These improvements made it feasible to extend the MC modelling of light transport to include more complex systems, such as those involving ultrasonic modulation of light (UL). Analytical results for two mechanisms of UL [134] were applied to a MC model of coherent light [133]: the validation of this MC model was incomplete however, since the analytical model only applies to isotropic scattering. This limitation was improved upon with an analytical solution for media with anisotropic scattering [107, 108]. An alternative approach to an analytical solution for UL makes use of the correlation transfer equation [109, 110], which is also appropriate for non-uniform US fields. A change in DC light level detected by a photorefractive crystal as a result of US-induced phase shifts has also been shown by MC modelling [9].

In addition to these two most common mechanisms of UL[2], additional effects have been proposed and modelled such as the curving of light rays in a medium with varying refractive index [117]. Changes in the wavelength of photons caused by the Doppler effect as a result of moving scatterers have also been considered [23]. These mechanisms all rely on relative phase changes and hence require coherent light, however this is not essential to observe US-modulation: mechanisms of the modulation of incoherent light have also been proposed [78], which consider local changes in absorption and scattering and lead to modulation in the DC light level.

In this Chapter I will introduce a method for including microbubbles in a Monte Carlo model of light transport in tissue. This requires a new method for determining the pathlengths of photons travelling through a turbid medium, since existing algorithms only account for single populations of homogenous scatterers such as is appropriate when light interacts only with

[2]The two main mechanisms of UL, refractive index changes due to pressure and pathlength changes due to scatterer displacement, are described in Section 2.2.

the biological medium. Microbubbles are first introduced in a simulation with coherent light to illustrate the effect of the pressure radiated from insonified bubbles on the modulation depth of a light signal detected on the surface of the turbid medium, making use of the analytical results derived in Section 3.3. This method for simulating ultrasound-modulated light in a medium containing microbubbles is then adapted to a system for detecting only DC changes in light level (intensity changes), which does not require coherent light. This is applied to the more clinically relevant situation of a large blood vessel containing blood of varying proportions of oxy/deoxyhemoglobin, and therefore varying optical absorption. The sensitivity of this microbubble-enhanced optical absorption (MOA) signal to the oxygen saturation in the blood vessel is computed to investigate the suitability of this technique for this clinical application, which is the focus of the latter Chapters in this thesis.

4.1 Phase-based Model for US-modulation of Coherent Light

The computational model presented here [46] is concerned with the transport of coherent light in tissue: applying an US field to the tissue can modulate the phase of photons as described in Section 2.2.1. This Monte Carlo (MC) model considers the effect of US pressure on the refractive index of tissue, which leads to a phase change ϕ_n, and the displacement of scatterers by US, which leads to a phase change ϕ_d. In addition to these previously established [81] mechanisms, the effect of adding microbubbles is simulated. The pressure radiated from the surface of an oscillating microbubble is expected to also modulate the refractive index of the surrounding medium, and hence give rise to a further phase shift ϕ_r (as derived in Section 3.3).

4.1.1 Monte Carlo procedure

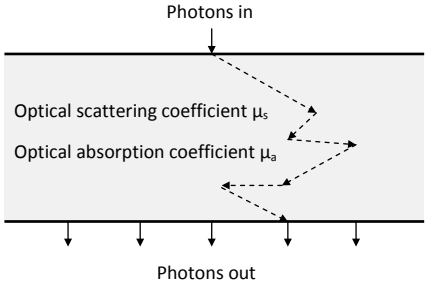

Figure 4.1: Slab geometry of the MC simulation, with photons injected at a single point, following a diffusive random walk through the turbid medium and exiting on the lower plane. The medium is finite in the z dimension and extends to infinity in the x and y dimensions.

The model is based on a MC model proposed by Wang [132,133], and implemented on a graphics processing unit (GPU) by Alerstam *et al.* [1] with improved computational speed [68]. This considers a slab geometry, with photons injected at a single point on the upper plane and detected across the surface of the lower plane (see figure 4.1). The pathlength of each photon between scattering events s_j is generated from the Poisson distribution $P(s_j = s') = \mu_t e^{-\mu_t s'}$, where $\mu_t = \mu_a + \mu_s$ is the total optical attenuation coefficient, which by definition is equal to the reciprocal of the mean free path. This can be integrated to give the cumulative distribution for photon pathlengths:

$$\begin{aligned} P(s_j < s) = \int_0^s \mu_t e^{-\mu_t s'} ds' = & \quad 1 - e^{-\mu_t s} \\ \Rightarrow s_j = & \quad -\frac{\ln(1-\zeta)}{\mu_t} \end{aligned} \tag{4.1}$$

where a uniformly distributed random number ζ is used to generate a photon pathlength from the cumulative distribution $P(s_j < s)$. When mi-

crobubbles are added to this model, we have a situation where the medium contains two distinct populations of scatterers: the background of biological scatterers, and the microbubbles. In this case a new procedure is required to both generate a photon path and determine whether at the end of that free path the photon scatters from a bubble or from the background medium. This requires two random variables to be generated, ζ_s and ζ_b, and two photon step sizes to be determined. This process is summarised in figure 4.2. This results in the same overall distribution of photon paths as would be achieved by generating a single length using the combined scattering coefficient $\mu_s + \mu_{s,b}$, where $\mu_{s,b}$ is the scattering coefficient of the population of microbubbles, except with the advantage that the model has determined which scattering event should occur at the end of the path.

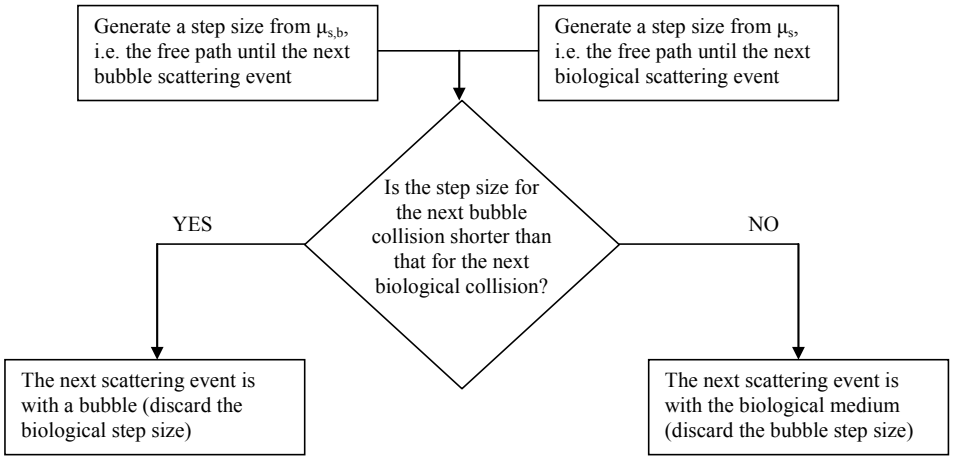

Figure 4.2: Flowchart describing the generation of a single free path length from the combined distribution of two scatterer populations.

The background medium is modelled using the optical properties of a solution of 1% Intralipid [121]: with anisotropic factor $g = 0.77$, optical scattering $\mu_s = 48$ cm^{-1} and absorption $\mu_a = 0.015$ cm^{-1}. The optical scattering coefficient of microbubbles $\mu_{s,b}$ is calculated using equation 3.9

and the linear approximation for a bubble radius $R(t)$ (equation 3.3). The time-averaged value of the scattering coefficient is used to remove the need to recalculate at every time step:

$$\langle \mu_{s,b}(t) \rangle = \pi \langle R(t) \rangle \rho_b Q = \pi \rho_b Q R_0^2 \left(1 + \frac{P_a^2}{2\beta^2} \right) \tag{4.2}$$

The quality factor is assumed to take the limiting value of $Q = 2$ for particles much larger than the optical wavelength [17]. An order of magnitude estimate for the microbubble concentration can be obtained by assuming that 1 ml of saturated microbubble solution is dissolved in 5 l of blood, in which case $\rho_b \approx 10^5$ mm^{-3}. The Henyey-Greenstein function (equation 3.10) with $g = 0.85$ is used to approximate the microbubble phase function.

There is a theoretical limit to the concentrations of microbubbles which can be modelled with these methods. Appendix A.5 describes the limits imposed by the assumptions of the optical model and the acoustic model, showing that a concentration of $\rho_b \approx 10^5$ mm^{-3} is within these limits. It should be noted that this is an unrealistically high concentration of microbubbles, and is likely to be significantly larger than the concentrations that are achievable *in vivo*. It is also larger than the maximum concentration which was achievable in the *in vitro* experiments presented in Chapter 7. The results here are not intended to be directly relatable to those which could be observed clinically, but are instead included to demonstrate a proof of principle and to illustrate the theoretical results derived in the previous Chapter. This high microbubble concentration will lead to a higher proportion of scattering events with microbubbles compared with scattering events with the biological medium, and therefore the effect of the radiated pressure from microbubbles on the phase of photons will be more noticeable.

4.1.2 Phase Differences

Spatial and temporal variations in the phase of photons exiting the medium will result in constructive and destructive interference, forming a speckle pattern (as described in Section 2.2.2). The autocorrelation of the detected light is used to extract the signal which varies at the frequency of the US, I_1. The phase shifts induced by the three mechanisms of US-modulation contribute to the autocorrelation as follows:

$$\begin{aligned} G_1(\tau) &= \langle E(t)E^*(t+\tau)\rangle = \left\langle E_0(t)E_0(t+\tau)e^{i\phi(t)}e^{-i\phi(t+\tau)}\right\rangle \\ &= \left\langle |E_0(t)||E_0(t+\tau)|e^{i\phi_n(t)+i\phi_d(t)+i\phi_r(t)}e^{-i\phi_n(t+\tau)-i\phi_d(t+\tau)-i\phi_r(t+\tau)}\right\rangle \\ &= \langle |E_0(t)||E_0(t+\tau)|\exp\left[-i\Delta\phi_n(t,\tau)-i\Delta\phi_d(t,\tau)-i\Delta\phi_r(t,\tau)\right]\rangle \end{aligned} \tag{4.3}$$

where $\Delta\phi_n(t,\tau) = \phi_n(t+\tau) - \phi_n(t)$ is the phase difference between two photons with a relative time delay of τ due to the US-modulation of refractive index, and similarly for $\Delta\phi_d$ (scatterer displacement) and $\Delta\phi_r$ (microbubble radiated pressure). So for each photon path and scattering event, it is only necessary for the MC model to track the phase differences (see Appendix A.4 for a derivation):

$$\begin{aligned} \Delta\phi_{n,j}(t,\tau) &= 4n_0k_0A_a\eta\sin(-\omega_a\tau/2)\sin(k_al_j\cos\theta_j/2) \\ &\quad \cos(\vec{k}_a.\vec{r}_{j-1} + k_al_j\cos\theta_j/2 - \omega_at - \omega_a\tau/2)/\cos(\theta_j) \\ \Delta\phi_{d,j}(t,\tau) &= 2n_0k_0A_a\sin(\omega_a\tau/2)\left[(\hat{k_{j+1}} - \hat{k_j}).\hat{k_a}\right] \\ &\quad \cos(\vec{k}_a.\vec{r}_j - \omega_at - \omega_a\tau/2) \\ \Delta\phi_{r,j}(t,\tau) &= \frac{2n_0k_0\eta k_a^2R_0^3P_a}{\beta}\left[\ln(\frac{R_0}{l_j}) + \ln(\frac{R_0}{l_{j+1}})\right] \\ &\quad cos(\vec{k}_a.\vec{r}_j - \omega_at - \omega_a\tau/2 + \xi)\sin(-\omega_a\tau/2) \end{aligned} \tag{4.4}$$

The expression for the phase difference due to microbubbles $\Delta\phi_{r,j}(t,\tau)$ depends on both the incident pathlength l_j and the pathlength which immediately follows the scattering event l_{j+1}. At the point of calculation in the MC model the receding pathlength of the photon is not known, and so is assumed to be equal to the mean free pathlength $l = 1/\mu_t$.

4.1.3 Results

The magnitude of the US-modulated component of the light signal is measured using the modulation depth $M = \frac{I_1}{I_0}$ (as explained in Section 2.2.2). Figure 4.3 shows the modulation depth as a function of US frequency with and without microbubbles included in the simulation. The linear resonance frequency predicted from the linearised Rayleigh-Plesset equation (1.6 MHz) is shown on the figure. There is an increase in modulation as a result of adding microbubbles. It has been shown that stronger scattering in a medium tends to lead to increased US-modulation [107]. However the higher modulation depth seen here is also dependent on the frequency of the applied US: this suggests that the modulation is not purely the result of the increased μ_s, which is independent of frequency. The largest relative increase occurs in the region around the resonant frequency, but not exactly at the theoretical resonance of 1.6 MHz. Although the bubble response is greatest at resonance (figure 3.2), and hence the radiated pressure will be at a maximum there, the total phase shift of a photon also depends on the phase offset of the bubble oscillations relative to the driving US (see equation 3.3). In addition, this predicted resonance point is only true for linear bubble oscillations, which occur at low driving pressures: figure 3.1 shows that for the US pressures used here the bubble response is not linear but contains higher order harmonics. This explains why the largest increase in modulation depth with microbubbles is not necessarily observed at the linear resonant frequency.

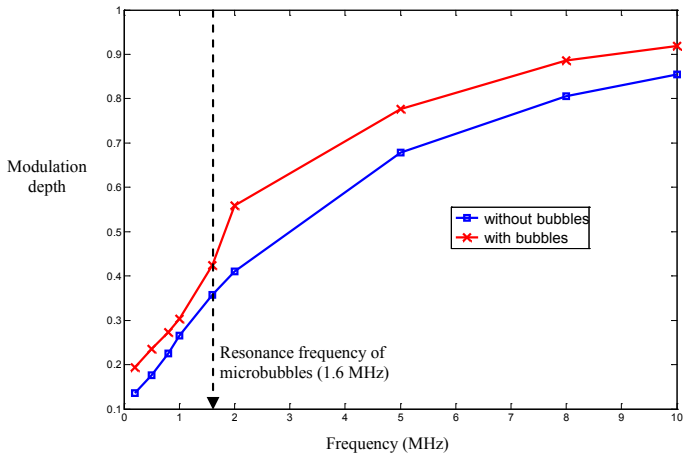

Figure 4.3: MC calculations of modulation depth M in a slab geometry with and without microbubbles (the plane-wave, CW US amplitude is fixed at $A_a = 1.7$nm). Microbubbles are monodispersed with radius $R_0 = 2.25\mu$m.

4.2 Non-phase Model for Oxygen Saturation Measurement

4.2.1 Blood Vessel Geometry

This model is not concerned with the phase differences induced in photons as a result of the applied US. The MC model only considers the total intensity arriving at a measurement point, and hence is designed to model the detection of a change in the DC light signal. For this non-phase based model [48], a more clinically relevant simulation geometry was chosen. Rather than a homogeneous slab, this model contains a large (diameter 1 cm) highly absorbing cylindrical blood vessel, surrounded by tissue with a low optical absorption. This geometry is illustrated in figure 4.4. Light is detected at a detection area located 25 mm from the point source. We make use of the symmetry of the model to also detect photons which arrive at a second identical detection area, reflected about the line of symmetry in the z-y plane.

The blood vessel is assigned the optical properties of venous blood, and also contains microbubbles. A model for the tissue properties of the extracerebral layer of the head [69] is used to estimate the optical absorption and scattering in the surrounding tissue.

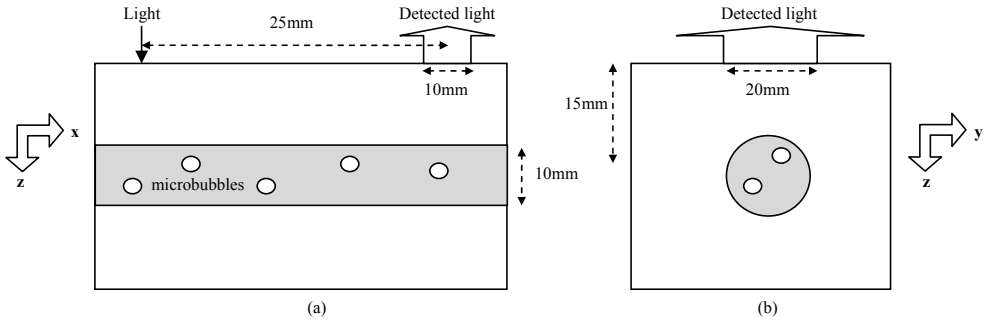

Figure 4.4: Simulation geometry, viewing the blood vessel from the side (a) and along its axis (b).

The blood vessel in this model contains both biological scatterers (with scattering coefficient μ_s) and microbubbles ($\mu_{s,b}$): the effective optical scattering is therefore given by $\mu_s + \mu_{s,b}$. This is handled by the MC code using the same procedure as the phase-based model (see figure 4.2). This model introduces an improvement from the phase-based approach in the way that $\mu_{s,b}$ is calculated: rather than assuming constant scattering, microbubble scattering varies spatially and temporally within the blood vessel according to the distribution of US pressure. Figure 4.5 illustrates the variation of bubble radius (and hence $\mu_{s,b}$) within the vessel. In this MC model the value of $\mu_{s,b}$ is given by equation 3.9, where the radius of a bubble as a function of position and time is calculated using the quadratic approximation to the Rayleigh-Plesset equation (Section 3.1.3).

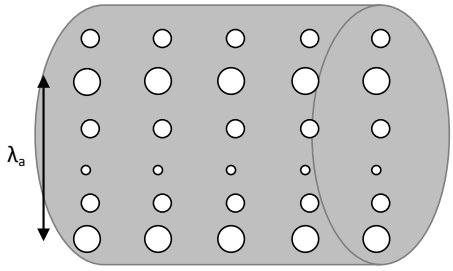

Figure 4.5: Size distribution of microbubbles within the blood vessel under US.

4.2.2 Oxygen Saturation

The optical properties of the surrounding tissue and of the blood within the vessel can be specified independently in this MC model. Whilst the background scattering μ_s is assumed constant, the optical absorption can be varied to model a range of oxygen saturations in the vessel (S_vO_2) or the tissue (S_tO_2). Here oxygen saturation is the fraction of hemoglobin which is oxygenated, defined as:

$$SO_2 = \frac{c_{HbO_2}}{c_{HbO_2} + c_{HHb}} \tag{4.5}$$

where c_{HbO_2} is the concentration of oxyhemoglobin and c_{HHb} is the concentration of deoxyhemoglobin. Although the total concentration of hemoglobin ($c_{HbO_2}+c_{HHb}$) is kept constant, changing the proportion of hemoglobin which is oxygenated alters the optical properties of the tissue: this is due to differences in the absorption spectra of oxy/deoxyhemoglobin [50] (see figure 4.6). The absorption in the blood vessel ($\mu_{a,v}$) is modelled by assuming a hemoglobin concentration of 14 g/dl, using known extinction coefficients for oxy/deoxyhemoglobin [4]:

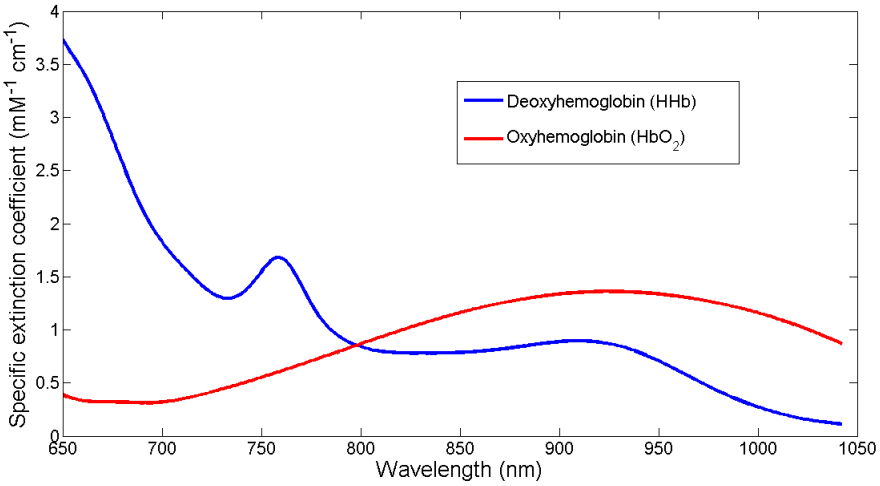

Figure 4.6: Specific absorption spectra of oxyhemoglobin and deoxyhemoglobin over a range of optical wavelengths commonly used in biomedical NIRS [15].

$$\mu_{a,v}(\lambda) = \epsilon_{HHb}(\lambda)c_{HbT}(1 - SO_2) + \epsilon_{HbO_2}(\lambda)c_{HbT}SO_2 \tag{4.6}$$

For the surrounding tissue a model for the optical properties of the extracerebral layer of the head [69] is used to approximate the absorption $\mu_{a,t}$, which also takes into account the background absorption due to water in the tissue. Table 4.1 summarises the optical properties of the blood vessel and surrounding tissue used in this MC model.

4.2.3 Sensitivity Analysis

In this section the model is used to investigate the sensitivity of a signal to changes of oxygen saturation (SO_2) in the blood vessel and surrounding tissue. A purely optical signal (such as that used in NIRS techniques) is compared with a microbubble-enhanced AO signal. The optical signal used

	μ_s (cm^{-1})	Aniso-tropy, g	Hb conc. (μM)	back-ground μ_a(cm^{-1})	SO_2 (%)	Hb μ_a (cm^{-1})
Tissue	20	0.9	11	0.032	65	0.1963
					70	0.1966
					75	0.1970
					80	0.1973
					85	0.1977
Blood	20	0.9	2200	-	65	5.063
					70	5.135
					75	5.207
					80	5.278
					85	5.350

Table 4.1: Parameters for the optical properties of the blood vessel and surrounding tissue in the MC model (for λ_0=830 nm).

here is the change in optical attenuation ΔA relative to a reference level:

$$\Delta A = \ln\left(\frac{I_{ref}}{I}\right) \tag{4.7}$$

where I_{ref} is the detected light intensity at oxygen saturations of 75% S_vO_2 and 75% S_tO_2. The microbubble-enhanced optical attenuation change, MOA, is defined as the difference in measured light attenuation resulting from the interaction between the US field and the microbubbles, $MOA = A_{US} - A$. The differential version of this (again relative to the reference level of 75% SO_2) is given by:

$$\Delta MOA = \Delta A_{US} - \Delta A \tag{4.8}$$

where ΔA_{US} is the measured change in optical attenuation relative to the reference SO_2 level with the US field turned on. The sensitivity of optical

techniques to changes in S_vO_2 is given by $\Sigma_{O,v}$, and the sensitivity of the AO signal to changes in S_vO_2 is given by $\Sigma_{AO,v}$:

$$\Sigma_{O,v} = \frac{\partial(\Delta A)}{\partial(S_vO_2)} \tag{4.9}$$

$$\Sigma_{AO,v} = \frac{\partial(\Delta MOA)}{\partial(S_vO_2)} \tag{4.10}$$

and similarly for the sensitivity of the optical/AO signal to tissue oxygenation changes ($\Sigma_{O,t}$ and $\Sigma_{AO,t}$). Figures 4.7 and 4.8 show the results of the MC simulation. This shows that the optical signal has a similar sensitivity to changes in blood vessel oxygenation compared with tissue oxygenation ($\Sigma_{O,v}/\Sigma_{O,t} = 1.7$): this property is exploited by NIRS in measurements of tissue oxygenation index [53,131], which provide a bulk measurement of oxygenation averaged over the whole tissue. The AO signal however is much more sensitive to changes in S_vO_2, with a relative sensitivity compared with tissue oxygenation of $\Sigma_{AO,v}/\Sigma_{AO,t} = 11.6$.

4.2.4 Pathlength Analysis

In order to explain the results of Section 4.2.3 we consider here a simplified model of light attenuation inside this blood vessel geometry, based on the modified Beer-Lambert law applied to an inhomogeneous medium [44]. Since the total hemoglobin concentration is constant within the tissue/vessel, the differential attenuation ΔA can be expressed in terms of changes in SO_2:

$$\Delta A = \epsilon_{HbO_2}\left[l_v c_{v,HbO_2} + l_t c_{t,HbO_2}\right] + \epsilon_{HHb}\left[l_v c_{v,HHb} + l_t c_{t,HHb}\right] \tag{4.11}$$

$$= \left[l_v c_v \Delta S_vO_2 + l_t c_t \Delta S_tO_2\right](\epsilon_{HbO_2} - \epsilon_{HHb}) \tag{4.12}$$

where $l_{v/t}$ is the partial path length (PPL) in the vessel/tissue, $c_{v/t}$ is the absolute total hemoglobin concentration in the vessel/tissue and $\epsilon_{HbO_2/HHb}$

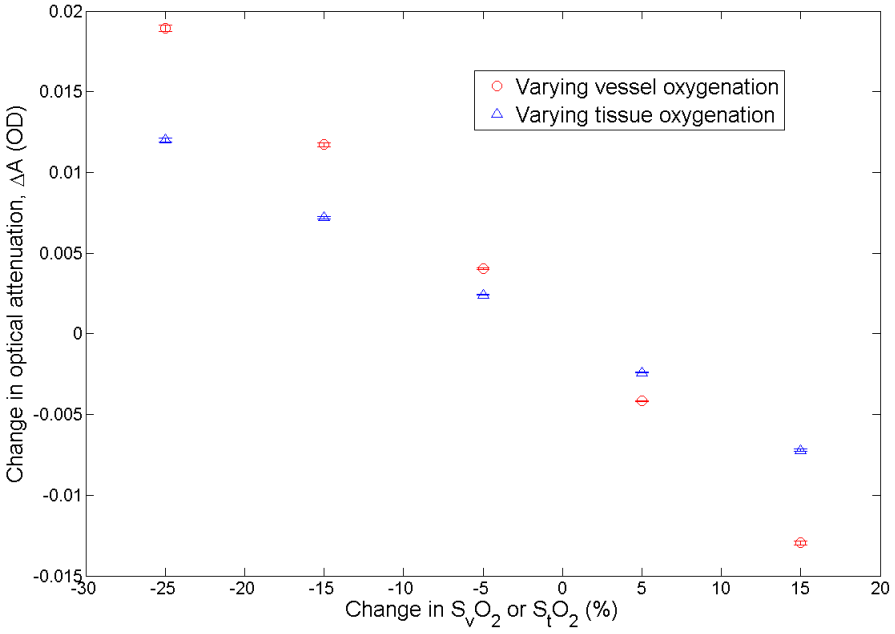

Figure 4.7: MC results showing change in optical signal as a result of changing vessel/tissue SO_2. A MC method with improved efficiency is used to compute these results, which is explained in more detail in Chapter 6.

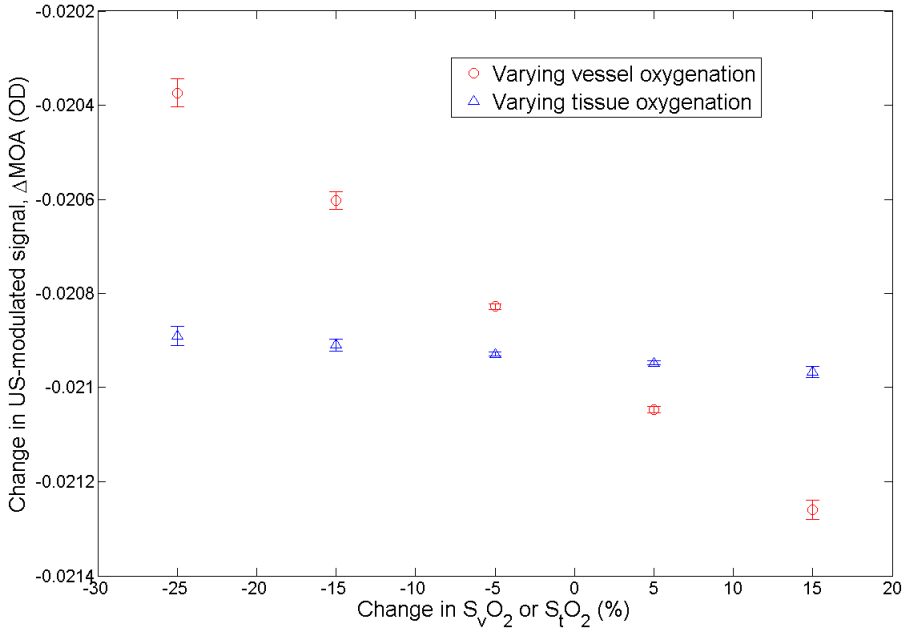

Figure 4.8: MC results showing change in AO signal as a result of changing vessel/tissue SO_2. A MC method with improved efficiency is used to compute these results, which is explained in more detail in Chapter 6.

is the specific extinction coefficient of oxy/deoxyhemoglobin. Figure 4.9 illustrates how the pathlength of a single photon through the medium is decomposed into a PPL within the tissue and a PPL within the blood vessel.

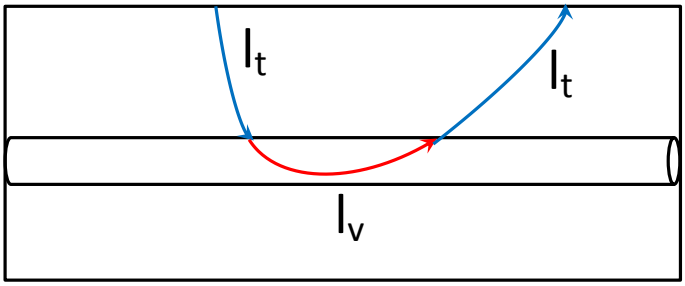

Figure 4.9: Illustration of the decomposition of a single photon pathlength into the PPL within the tissue (l_t) and the PPL within the blood vessel (l_v).

Similarly for the MOA signal, an analytical model can be derived by combining the modified Beer-Lambert law (equation 4.12) with the definition of MOA (equation 7.5), giving:

$$\Delta MOA = \left[\Delta l_v c_v \Delta S_v O_2 + \Delta l_t c_t \Delta S_t O_2\right] \left(\epsilon_{HbO_2} - \epsilon_{HHb}\right) \tag{4.13}$$

where $\Delta l_v = l_{v,US} - l_v$ is the change in PPL in the blood vessel as a result of US-modulation (and similarly for Δl_t). According to these models, the sensitivity of optical attenuation to vessel oxygenation is proportional to $l_v c_v$, whereas the sensitivity of an AO signal to $S_v O_2$ changes is proportional to $\Delta l_v c_v$. Changes in the PPLs of photons within the tissue and the blood vessel are a result of US-induced changes in microbubble scattering in the vessel. The MC model also tracks the pathlengths of individual photons: these have been compiled into a histogram which illustrates the distribution of these PPLs with and without US-modulation (see figure 4.10). Table 4.2

shows the mean PPLs as obtained from these histograms, as well as the mean changes in PPL Δl_v and Δl_t.

	PPL without US (mm)		US-induced change in PPL, Δl (mm)	
	Mean	Standard error	Mean	Standard error
Vessel PPL, l_v	0.440	0.003	0.0118	0.0002
Tissue PPL, l_t	51.10	0.04	0.21	0.02

Table 4.2: PPLs l_v and l_t and changes in PPL induced by US Δl, calculated from the MC model.

An estimate for the relative sensitivity of the optical signal to S_vO_2 can be found by combining the MC results for the mean PPLs (table 4.2) with the analytical model based on the modified Beer-Lambert law (equation 4.12): the relative sensitivity is then given by the ratio l_vc_v/l_tc_t. Similarly the relative sensitivity of the AO signal to S_vO_2 is predicted by equation 4.13 to be $\Delta l_vc_v/\Delta l_tc_t$, where Δl_v and Δl_t are also provided by the MC simulation. Table 4.3 compares these predictions with the simulation results for the optical and AO signal. A relative sensitivity greater than 1 indicates that the technique is more sensitive to changes in S_vO_2 than to S_tO_2, whereas a relative sensitivity less than 1 implies that the technique is more sensitive to S_tO_2.

	Relative sensitivity to vessel S_vO_2	Predicted by analytical model (eqns 4.12 and 4.13)	Simulation results (Figure 4.7 & 4.8)
Optical signal	$\Sigma_{O,v}/\Sigma_{O,t}$	1.68	1.7
AO signal	$\Sigma_{AO,v}/\Sigma_{AO,t}$	11.63	11.6

Table 4.3: Relative sensitivity of optical and AO signal to blood vessel oxygenation: results of the MC simulation are compared with predictions from the modified Beer-Lambert law (with values for l and Δl taken from table 4.2).

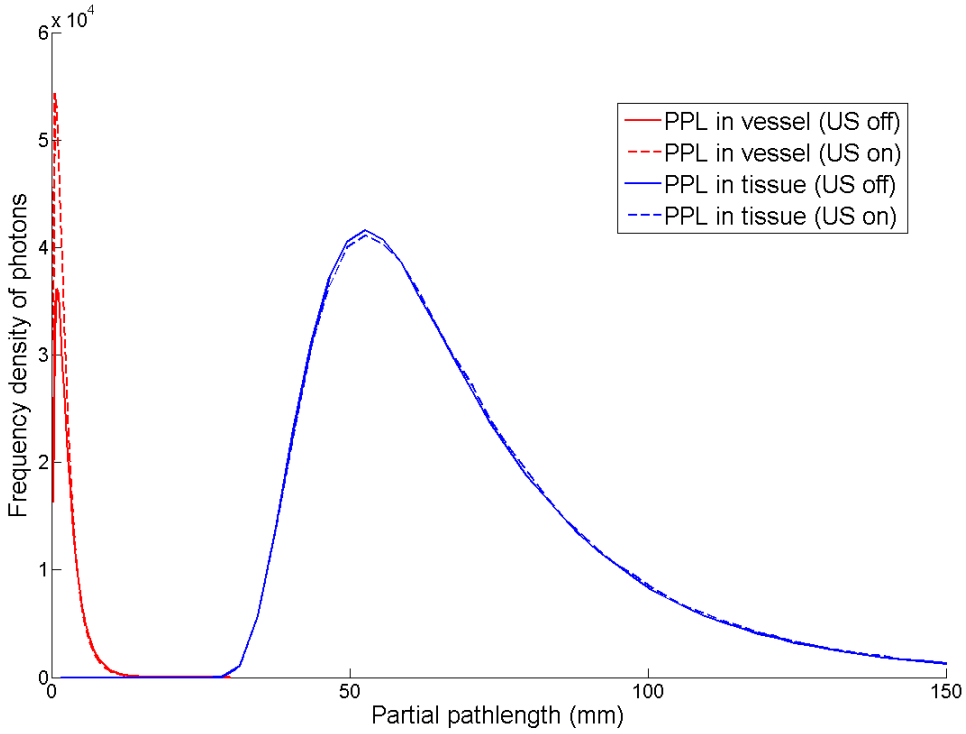

Figure 4.10: MC results for PPLs of photons in the blood vessel and surrounding tissue, compared with PPLs of photons with US-modulated optical scattering from microbubbles. (10^8 photons in total were sampled.)

The modelling of the non-phase based modulation of incoherent light by insonified microbubbles presented here suggests that a measurement of MOA may be sensitive to the changes in optical properties of highly absorbing structures within a medium. This sensitivity is explained by analysing the pathlengths of photons travelling through the medium, and the effect of US-modulated optical scattering from microbubbles on these pathlength changes. These results were used to inform the planning of the experimental studies present in Chapter 6. The MC model presented here is mainly limited by the long computational time required to perform a sensitivity analysis. Certain assumptions have been made to increase the simulation efficiency, such as using a 2nd order approximate analytical solution to determine the radii of insonified microbubbles rather than a full numerical solution. However despite this simplification the speed of the simulation is still too slow to be practical to be used for calculations such as solving the inverse problem of relating S_vO_2 to an MOA measurement. For this reason Chapter 6 will concentrate on a method for improving the computational efficiency of these MC simulations, perturbation Monte Carlo (pMC), which was used to compute the results shown in figures 4.7 and 4.8.

Chapter Summary

- A MC model of US-modulation of coherent light including microbubbles is implemented. The additional phase shift due to the pressure radiated by microbubbles is derived in Chapter 3.

- The modulation depth of the AO signal is increased when microbubbles are present, with the largest relative increase seen when the US frequency is close to the predicted resonant frequency.

- The effect of microbubbles on a non-coherent light signal is also demonstrated with a further MC model, containing a cylindrical blood vessel surrounded by tissue.

- Sensitivity analysis shows that the microbubble-enhanced optical attenuation is more sensitive to changes in SO_2 of a large blood vessel rather than to changes in the SO_2 of the surrounding tissue. A NIR signal shows similar sensitivity to changes in the surrounding tissue SO_2 and in the blood vessel SO_2.

- Despite using an analytical approximation to determine the radii of insonified microbubbles, the complexity of this MC model is such that it is unsuitable for large-scale analysis such as solving the inverse problem of S_vO_2 measurement.

Chapter 5

Perturbation Monte Carlo

In Chapter 4, a method for incorporating microbubble scattering in a Monte Carlo model for light transport in tissue was presented. It was noted here that the MC method in this form had several deficiencies. Firstly, the computational time required to simulate enough photons for a convergent result was prohibitively long; to reduce this time, an analytical approximation was used to the radius of a microbubble as it oscillates under US which did not require a full numerical solution of the equation of motion in realtime. Whilst this approximation matches closely with the numerical solution when the driving amplitude is low, non-linear components of the oscillation grow with US pressure and cause the analytical solution to diverge from the numerical result. In addition, the eventual purpose of this model will be to investigate the sensitivity of a microbubble-enhanced optical attenuation (MOA) signal to changes in oxygen saturation, which requires many simulations over a range of parameters. For this reason, it is necessary to consider MC methods which are able to generate simulation results for a range of optical properties more efficiently, which will be the subject of this Chapter.

The flexibility of a Monte Carlo model of light transport makes this a very useful tool for simulating complex geometries, where analytical models

such as those based on the diffusion equation cannot provide a solution. Although a statistical solution can be found for any structure, one drawback of the MC method is that the length of computational time required for a solution to converge is very dependent on the geometry of the model [52]. When the tissue to be modelled contains regions of high absorption, such as blood in large vessels, a prohibitively large number of photons may be required to produce a convergent light distribution. The explanation for this is that most photons that pass through the blood are absorbed, leaving very few which eventually reach the detector. This has been noted, for example, in the simulation of energy deposited in blood vessels during photodynamic therapy [58, 79]. In this work MC simulations will be used to investigate the sensitivity of an optical measurement to a highly absorbing blood vessel. A NIR signal has been shown to be insensitive to changes in blood vessel oxygenation, both in theoretical [31] and experimental [76] studies: to model this situation with sufficient precision for sensitivity analysis would require more computational time than is practical, and so a more efficient technique was investigated. In this Chapter a MC model based on perturbation Monte Carlo theory (pMC) will be presented and applied to the problem of highly absorbing structures within turbid media.

The advantage of pMC is that the results of a light transport model in different media with different optical properties can be generated from a single MC simulation [36]. The assumptions required for this are the same as those made in a standard MC model of light transport, i.e. that the lengths of the photon free paths are much longer than the optical wavelength (the weak scattering approximation) and that the acoustic displacement is smaller than the optical wavelength [107]. The principle of pMC is that this method only requires knowledge of the pathlength of each photon, and the number of interactions that photon experienced with the medium. The detected weight of each photon for a single set of nominal optical properties is recorded by

the initial MC simulation. To determine what the weight of a photon following the same path in a medium of different absorption and/or scattering would be, an additional perturbation term must be applied which depends on the difference in optical coefficients between the desired medium and the simulated medium [60, 112]. This reduces the required computational time greatly, particularly in problems that require small changes in absorption to be applied such as inverse problems [41] and sensitivity analysis.

Consider a single photon travelling through a medium which contains N regions of distinct optical properties $\hat{\mu}_{a,i}$ and $\hat{\mu}_{s,i}$. If the weight of a photon, W, travelling through another medium of different optical properties $\mu_{a,i}$ and $\mu_{s,i}$ is known, then the new weight of the photon $\hat{W}$ in the desired medium can be calculated given that S_i is known by applying a perturbation [115]:

$$\hat{W} = W \prod_{1 \leq i \leq N} \left(\frac{\hat{\mu}_{s,i}/\hat{\mu}_{t,i}}{\mu_s/\mu_t} \right)^{j_i} \left(\frac{\hat{\mu}_{t,i}}{\mu_t} \right)^{j_i} \left[\frac{\exp(-\hat{\mu}_{t,i} S_i)}{\exp(-\mu_t S_i)} \right] \tag{5.1}$$

where S_i is the partial pathlength (PPL) of the photon within the ith region, and j_i is the number of interactions experienced by the photon in that region. In the case where the scattering is constant and only the absorption is perturbed in each region, this expression simplifies considerably (see equation 5.5) and the number of collisions or scattering events is no longer required to perform this pMC analysis. The PPLs in each region of the medium are sufficient to reproduce an optical field for any set of absorption parameters. This process has been shown to be accurate (<1% error) even when the absorption coefficients are large compared with scattering [60], where the alternative models based on the diffusion equation fail.

The aim of this Chapter is to show that a simulation based on pMC can also be used to model a medium containing insonified microbubbles, whose

optical scattering varies spatially and temporally. The reflectance on the top surface of the medium as predicted by the pMC model is compared with an analytical model based on the diffusion equation (DE) [84], which can provide an exact solution in the case of the simple geometries investigated in sections 5.2.1 and 5.2.2. The pMC model developed in this Chapter is used later to provide a comparison with the experimental results of Chapter 6, and to investigate the feasibility of a clinical measurement of oxygen saturation from a blood vessel with microbubbles (Chapter 7).

5.1 Structure of Sumptuous Bubbles

The pMC model used in this section is based on code developed at UCL, affectionately known as Sumptuous (simulating ultrasound-modulated photons), which is based on a modified version of a MC model developed for acousto-optics [98]. This is a finite-element implementation of a light propagation model within an optically scattering and absorbing medium. The medium is defined by a tetrahedral mesh, with optical properties specified for distinct structures within the medium which are subsets of this mesh. In this work we use two broad classes of tissue type: blood, in this example contained within a large (2mm) cylindrical vessel with high absorption, and tissue surrounding the blood vessel, with lower optical absorption. Figure 5.1 shows the dimensions of the tissue structure.

The blood vessel contains microbubbles, which increase the optical scattering. The scattering coefficient for bubbles $\mu_{s,b}$ is calculated from a numerical Rayleigh-Plesset model (see Section 3.2). This is used to generate the step lengths of photons travelling within the blood vessel. Inside the vessel there are two distinct populations of scatterers: the biological medium (with the properties of venous blood) and intravenous microbubbles. After each photon free path, it is necessary for the MC procedure to identify which type

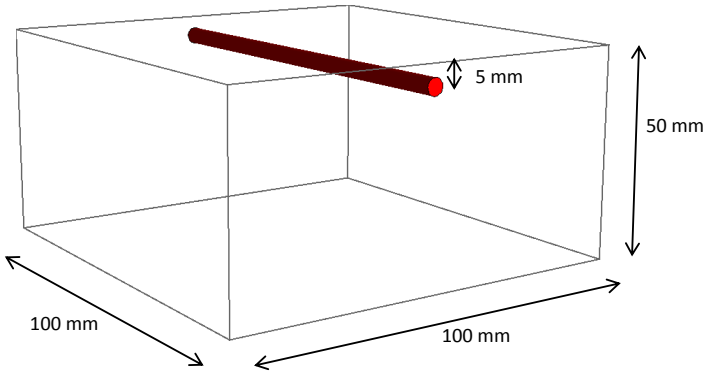

Figure 5.1: The medium structure, containing two distinct regions with indepedent optical properties. A cylindrical blood vessel containing microbubbles runs parallel to the top surface.

of scatterer the photon has collided with so that the correct scattering phase function and albedo can be used; if its path terminates in the vessel, this collision could be with either the background or a microbubble. This is dealt with using the same mechanism as was developed in Chapter 4, by generating two random numbers ξ_b and ξ_m. Using these, free paths until the next bubble collision s_b and the next collision with the medium s_m are generated from the Poisson distribution $\xi = \exp\left[-\int_0^s \mu_s(\bar{r}, t)ds\right]$. This assumes that the absorption of the microbubbles, $\mu_{a,b}$, is zero.

If $s_b > s_m$, then the next scattering event is with the biological media, and the free path will be equal to s_m. If $s_b < s_m$ then the photon will hit a microbubble first, and the path s_m is discarded. This results in an equivalent pathlength distribution to a material with total scattering $\mu_{s,b} + \mu_s$. The US period is assumed to be much longer than the time of flight of a photon, and so as the path of each photon is being calculated the scattering $\mu_{s,b}(r)$ is fixed. The resultant scattering along a given photon path is found by

integrating $\mu_{s,b}(r)$ along that path. This must be performed iteratively in the MC model, since the free path of the photon will itself depend on the resultant scattering coefficient. In this implementation $\mu_{s,b}(r)$ is assumed to vary piece-wise linearly, with the variation across each acoustic wavelength divided up into 50 layers. The integral can then be discretised:

$$-\ln \xi_b = \mu_{s,b}(t, \bar{r}_1)\frac{h_1}{\cos\theta} + \sum_{\mathrm{i}=2}^{\mathrm{N}-1} \mu_{s,b}(t, \bar{r}_i)\frac{h}{\cos\theta} + \mu_{s,b}(t, \bar{r}_N)\frac{h_N}{\cos\theta} \qquad (5.2)$$

where h is the width of each layer within which $\xi_{s,b}$ is assumed constant, θ is the angle between the photon direction and the US direction, h_1 is the distance until the photon reaches the first layer transition and $\bar{r}_i$ is the midpoint of the ith layer. The final step h_N is adjusted so that it is less than h and the equality holds. The total pathlength is then $s_b = h_1 + h_N + (N-2)h$. Figure 5.2 illustrates the piece-wise linear decomposition of this photon path within a medium with variable microbubble scattering. The values of $\mu_{s,b}$ for each layer are generated as described in Chapter 3, and stored by the MC code. Once the step size has been generated, and the type of collision determined, the remainder of the MC process follows a standard procedure (summarised in figure 5.3). The MC code also contains some variance reduction procedures [132].

5.2 Validating Sumptuous Bubbles

After tracking the path of each photon from the source to the point where it is either detected or absorbed, Sumptuous reports the surviving weight of the photon and its partial pathlengths (PPLs) in the vessel and the tissue seperately. Using these PPLs, the absorption in either compartment can be adjusted by post-processing the photon weights according to pMC theory. In this section, the reflectance detected on the top surface of the tissue is com-

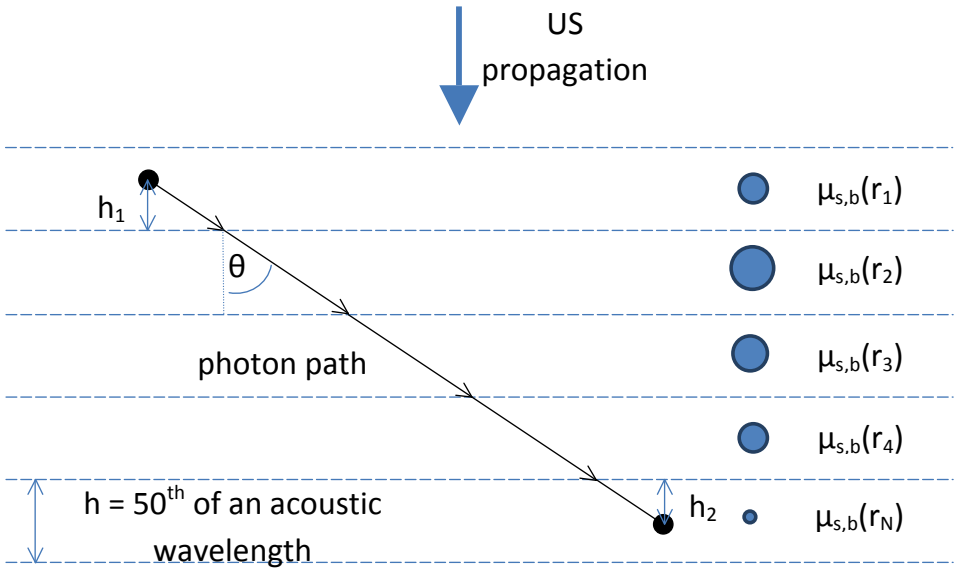

Figure 5.2: Linear decomposition of a free photon path travelling through a medium with spatially varying microbubble scattering.

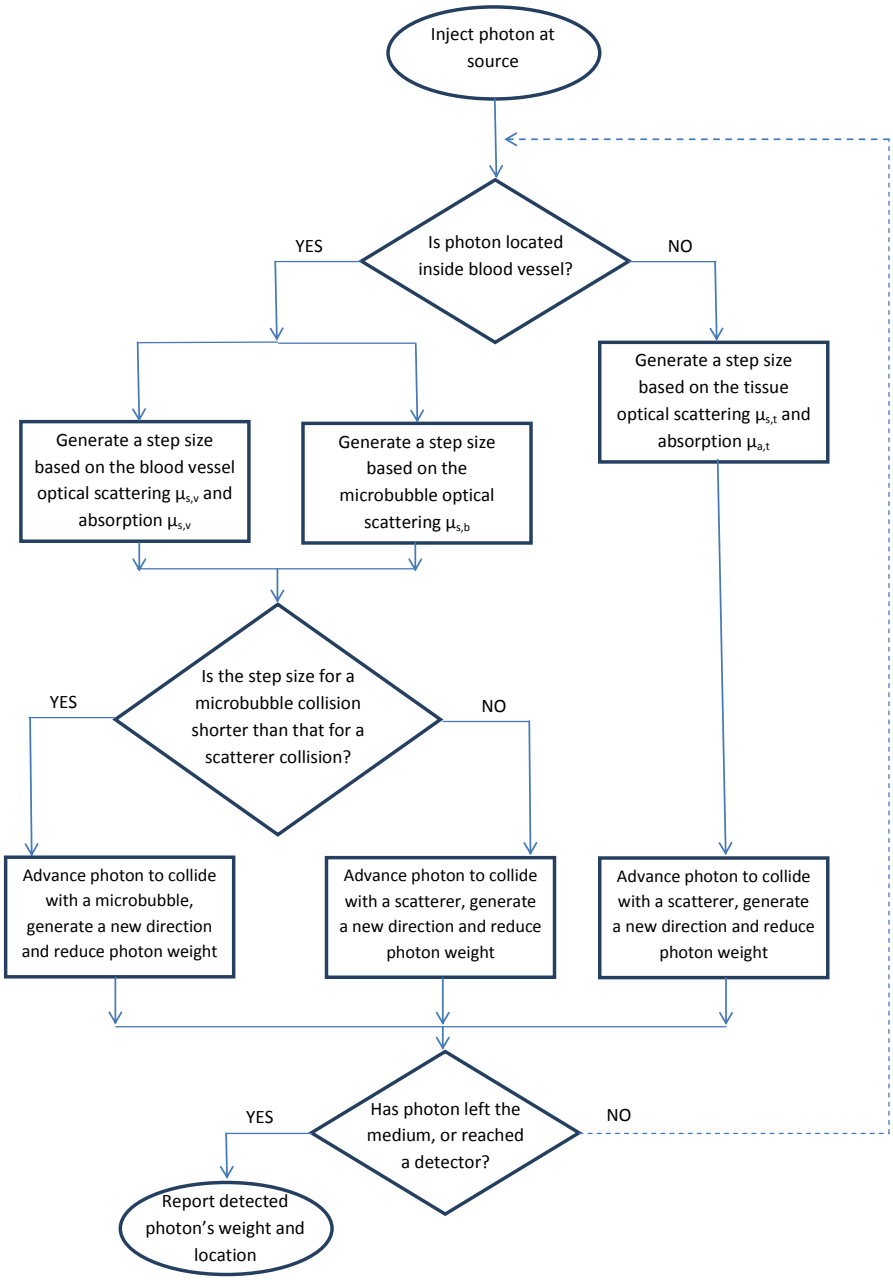

Figure 5.3: Flowchart outlining the process for propagating a photon through a medium composed of two distinct compartments. One compartment (the blood vessel) contains both biological scatterers and microbubbles.

pared with an analytical solution. The fluence in the tissue is calculated using the diffusion equation (DE), which is valid when multiple scattering dominates (as is the case in biological tissue, where $\mu_s \gg \mu_a$). The single point beam of light injected on the top surface can be represented by an isotropic point source at a depth of $1/(\mu_a + \mu_s)$, which is the depth at which incoming light no longer retains its directionality but can be treated as isotropic within the medium [20]. The reflectance R at a distance r from the source was found using an n-layered model by Kienle *et al.* [60]. This implements the DE in a cylinder which can be divided into n horizontal slices with different μ_a and μ_s.

The PPLs of photons reported by Sumptuous are compared with the values predicted by the modified Beer-Lambert law (MBLL). In the case where the medium is divided into distinct compartments, the mean PPL in each compartment is given by:

$$< l_i >= \frac{dA}{d\mu_{a,i}} \tag{5.3}$$

where $< l_i >$ is the mean PPL in the ith compartment, $\mu_{a,i}$ is the absorption in that part of the tissue and A is the attenuation at a point on the tissue surface.

In this section the Sumptuous Bubbles model is subjected to four tests in order to validate its output. Firstly the reflectance from a homogeneous medium without microbubbles is compared with an analytical DE solution, in order to confirm that the additional code included in the model which handles the possibility of microbubble scattering has not affected the performance of the model when the microbubble concentration is set to zero. Secondly microbubbles are added to the medium, and the simulated reflectances with and without US insonification are compared with the DE solution. These first

two tests validate the handling of spatially and temporally varying optical scattering from microbubbles (equation 5.2). Next a blood vessel structure is added to the medium, and the partial pathlengths of photons within the surrounding tissue and within the vessel are validated against those estimated using the MBLL. Finally these PPLs are used to generate a reflectance from a highly absorbing blood vessel by applying pMC theory to a simulation with nominal optical absorption. This result is compared with the reflectance generated from a standard MC simulation with the same high absorption, in order to validate the pMC analysis.

5.2.1 Homogeneous medium

Firstly the reflectance is calculated from the weights of photons detected on the top surface of the tissue. A homogeneous medium is used in this case, i.e. the blood vessel is assigned the same optical properties as the surrounding tissue. The dimensions of the medium are 100 mm x 100 mm x 50 mm. The reflectance can therefore be compared with the DE solution for a homogeneous medium. No microbubbles are present, and the medium has optical scattering $\mu_s' = 20\text{cm}^{-1}$ and low absorption $\mu_a = 0.1\text{cm}^{-1}$ to ensure that light propagation is in the diffusion regime. The reflectance is calculated using a series of ring detectors at a distance r from the source, each with a radial width Δr, so that the reflectance is given by:

$$R(r_i) = \frac{\sum W_i}{2\pi r_i \Delta r N} \tag{5.4}$$

where $R(r_i)$ is the reflectance at radial distance r_i, $\sum W_i$ is the total of all photon weights detected in the ith ring and N is the total number of photons launched from the source. The radially-resolved reflectance is shown on figure 5.4, along with a DE solution for the same optical parameters.

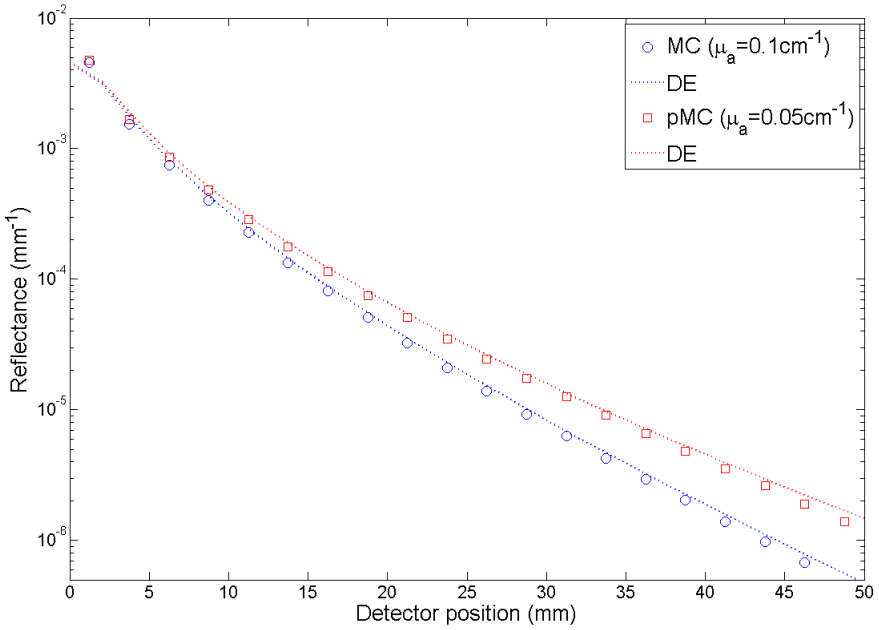

Figure 5.4: Radially-resolved reflectance from MC results and pMC analysis, compared with equivalent DE solutions.

These results for $\mu_a = 0.1\text{cm}^{-1}$ are then re-processed using the pMC approach. The weights of each photon are rescaled for a new absorption value of $\hat{\mu}_a = 0.05\text{cm}^{-1}$ according to each of their pathlengths l_i:

$$\hat{W}_i = W_i \exp \frac{-\hat{\mu}_a l_i}{-\mu_a l_i} \tag{5.5}$$

where W_i is the detected weight of each photon and $\hat{W}_i$ is the weight for the new perturbed absorption value. The resulting reflectance is compared with the theoretical DE result (shown in figure 5.4), showing close agreement more than a few mm from the source where light is in the diffusion regime. This test confirms that the code added to the model which handles the possibility of microbubble scattering has not affected the performance of the model when the microbubble concentration is set to zero, and validates the basic photon transport model in Sumptuous.

5.2.2 Microbubbles with and without insonification

In this section the handling of microbubble scattering by the MC model is validated: to compare this with the n-layer DE [60], a structure of 50 layers per acoustic wavelength was chosen (i.e. $h = \lambda_a/50$, see equation 5.2). The scattering for each layer was calculated as the sum of the background μ_s plus the microbubble $\mu_{s,b}$ at that location, assuming a microbubble concentration of $\rho_b = 10^5\text{mm}^{-3}$. The first layer had a larger depth of 1 mm, to ensure that the isotropic point source was located in this slice. In half of the simulations, the medium was insonified with US at a frequency of 1 MHz (and therefore wavelength of 1.5 mm) and peak pressure 100 kPa.

Where $z > 1$ mm, both microbubbles and background scatterers were present as shown in figure 5.5 (with no vessel structure included here). A large background scattering of $\mu_s' = 12\ \text{cm}^{-1}$ and low absorption of $\mu_a = 0.05$

cm^{-1} were chosen so that the fluence was isotropic. Reflectance was also computed with the MC model with identical background scattering (and a 1 mm 'buffer' layer to match the DE solution), and figure 5.6 shows that these results agree within 5 cm of the source. This process was repeated with the US field turned on, in which case the microbubble scattering now varies in each of the n layers according to the solution from Section 3. This is handled by the MC model using piece-wise integration along photon paths as previously described.

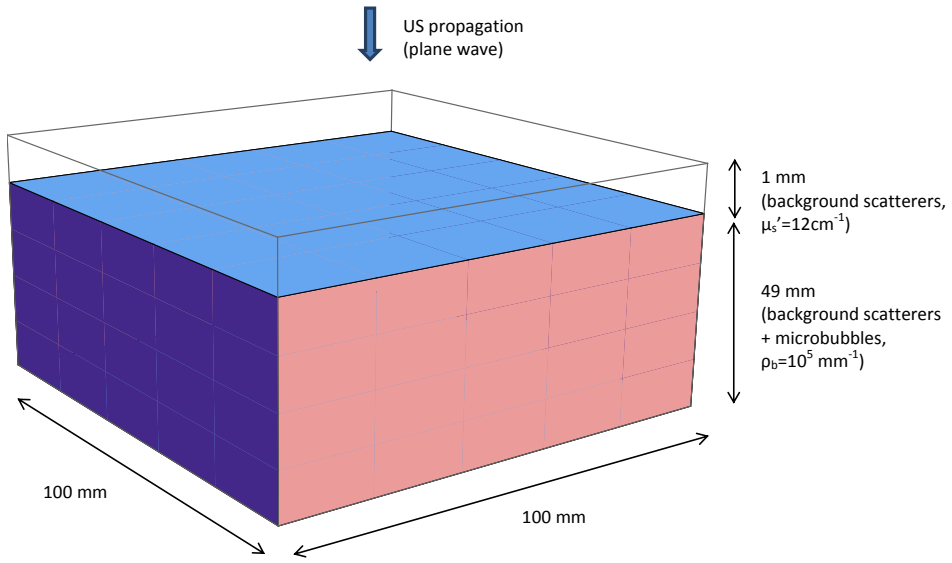

Figure 5.5: Geometry of the simulation for the homogeneous medium containing microbubbles. Within 1 mm of the source there are no microbubbles, so as to match the diffusion equation solution. Photons are injected at the centre of the top surface.

The agreement of the MC results with the DE solution gives confidence that the process used to generate photon free paths between microbubble scattering events is reliable, and can handle the situation where microbubble scattering varies over a short distance scale (0.03 mm). The US wavelength

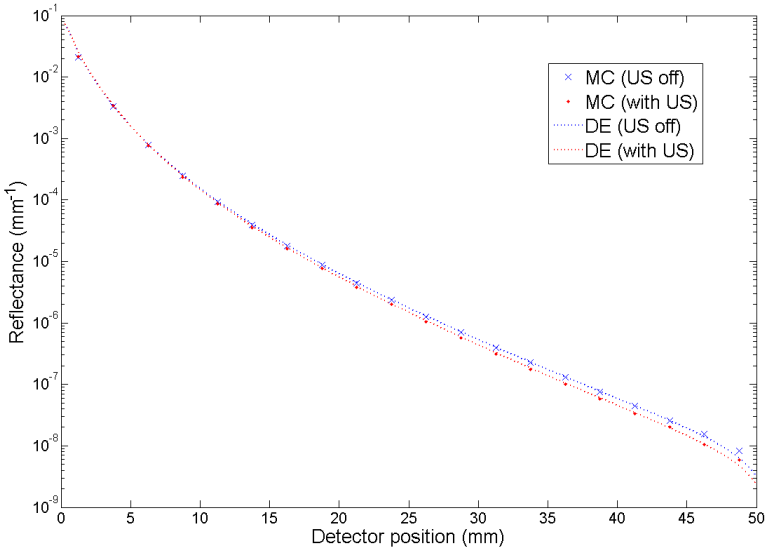

Figure 5.6: Reflectance for a homogeneous medium containing microbubbles, with and without US applied. This is compared with a DE solution for an equivalent n-layered medium.

used in this validation is chosen to be the same as that used in the experimental and theoretical studies presented in the following Chapters of this thesis.

5.2.3 Partial pathlength tracking

The tracking of photon pathlengths is now compared with an analytical result from the Beer-Lambert Law (BLL). The homogeneous case will be addressed first. Equation 5.3 is used to calculate the mean pathlength of photons arriving at a given detector position on the top surface. The pMC procedure previously described is applied to each photon weight to give a 1% change in μ_a. The resulting change in attenuation is then $\Delta A = \log(I/\hat{I})$, for a given absorption change $\Delta\mu_a = \hat{\mu}_a - \mu_a$. This BLL estimate is compared with the mean pathlength of all detected photons reported by Sumptuous:

$$\langle l \rangle = \frac{\sum W_i l_i}{\sum W_i} \tag{5.6}$$

where W_i and l_i are the weights and pathlengths of all photons detected at a certain radius from the source. Figure 5.7 shows the agreement of the mean pathlengths of photons calculated by these two methods.

A similar analysis is now performed for the case where the tissue is no longer homogeneous, and the medium is seperated into two compartments. A cylindrical blood vessel is now included (see figure 5.1), and the PPLs of photons moving within the vessel are tracked seperately from their PPLs in the surrounding tissue. The absorption in the blood vessel is large compared with the surrounding tissue: $\mu_{a,v} = 5\text{cm}^{-1}$ in the vessel and $\mu_{a,t} = 0.05\text{cm}^{-1}$ in the tissue. The PPL in the vessel, l_v, is estimated by varying $\mu_{a,v}$ by 1% and applying equation 5.3. Figure 5.8 shows these theoretical results for the PPL of photons detected at a distance r from the source, compared with the

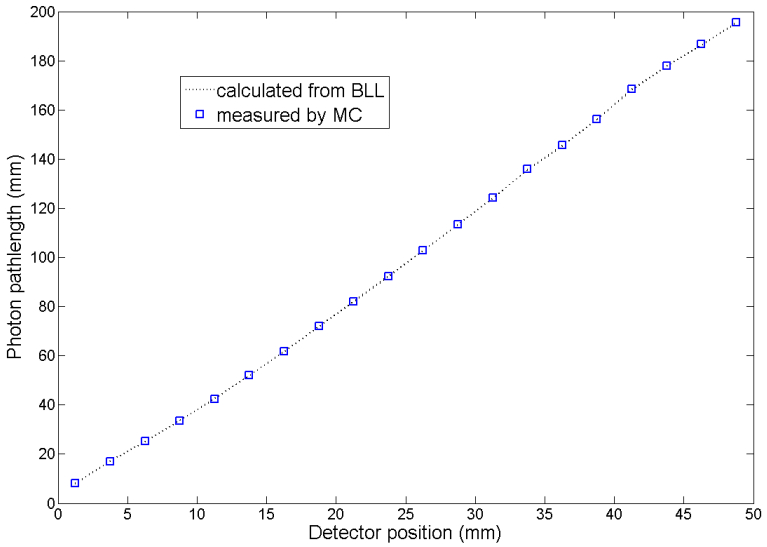

Figure 5.7: Mean pathlength through a homogeneous medium of photons detected at a given radius from the source. The theoretical result is calculated using the Beer-Lambert Law.

actual values tracked by the MC simulation.

The PPLs tracked by the model have been shown to agree with analytical results, and so those PPLs are used in the final section of this Chapter to test the pMC algorithm. This algorithm is applied to the results of a simulation to generate an optical distribution for a medium of different optical properties.

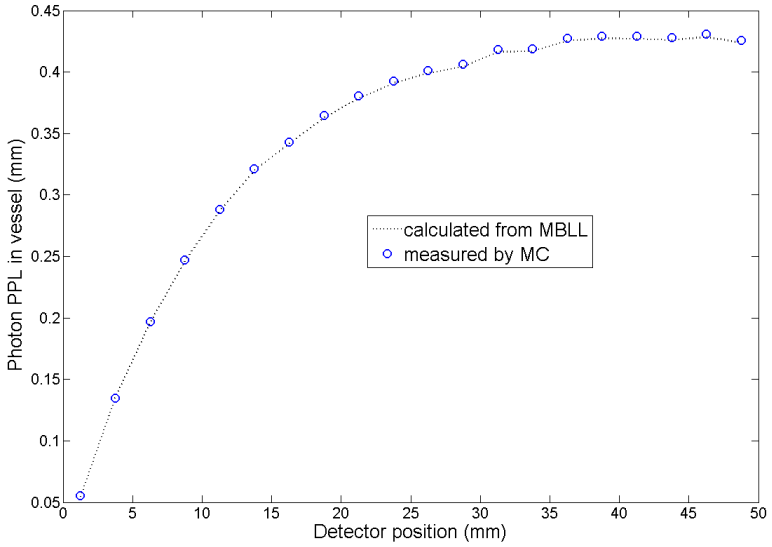

Figure 5.8: Mean partial pathlength of photons within the vessel in the case of an inhomogeneous medium, detected at a given radius from the source. The modified Beer-Lambert Law is used to calculate the theoretical result.

5.2.4 pMC in a heterogeneous medium

Finally the pMC algorithm is applied in the non-homogeneous case, with the blood vessel structure now present. Since the PPLs of photons are tracked seperately for both compartments, it is possible to vary the absorption in the vessel $\mu_{a,v}$ independently from the absorption in the surrounding tissue $\mu_{a,t}$. In this section the results of a pMC simulation are compared with a

standard MC simulation with equivalent optical properties.

The pMC results are generated by running a MC simulation with nominal optical properties of $\mu_{a,t} = \mu_{a,v} = 0.05\text{cm}^{-1}$. Equation 5.5 is applied to each photon to produce photon weights for a different set of optical parameters $\hat{\mu}_{a,t}$ and $\hat{\mu}_{a,v}$, using the tracked PPL values l_t and l_v. Figure 5.9 shows the pMC results for two sets of properties calculated in this way, compared with the reflectance from a standard MC simulation performed with the same absorption parameters without perturbation analysis.

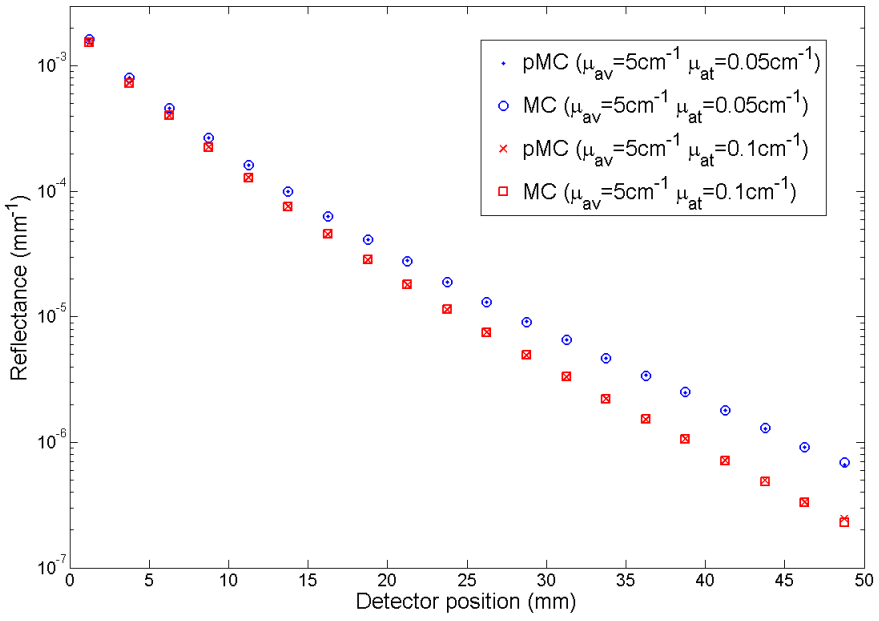

Figure 5.9: Radially-resolved reflectance for two sets of optical parameters, calculated using pMC from one result with nominal $\mu_{a,v}$ and $\mu_{a,t}$. This is compared with the result from a standard MC simulation.

This section has confirmed that the reflectance from a medium containing a highly absorbing blood vessel can be generated by applying pMC theory

to a MC simulation with nominal (low) optical absorption. The Sumptuous Bubbles model validated here is used in the following Chapters. This will provide comparative results to accompany an experimental measurement of microbubble-enhanced optical attenuation. Sumptuous Bubble is also used to investigate theoretically the limitations on applying this microbubble-enhanced optical technique to a clinical application, such as *in vivo* measurements of oxygen saturation from a large vein.

Chapter Summary

- pMC can be used to produce radially-resolved reflectance from structures with different optical properties by post-processing the same set of MC data.
- For a homogeneous cylindrical medium, the reflectance produced by the pMC method using the Sumptuous model agrees closely with the DE solution.
- The implementation of insonified microbubbles with Sumptuous is validated by comparing the simulated reflectance with an n-layer DE solution, showing good agreement.
- The photon pathlengths reported by Sumptuous are also validated against an estimate of the total and partial pathlengths made by applying the BLL (and MBLL) to the reflectance measurements.
- pMC simulations with a cylindrical blood vessel structure have been made for a range of absorptions within the vessel, producing reflectances which agree closely with those generated from a MC siulation.
- Sumptuous Bubbles therefore provides a reliable basis for estimating light transport through a turbid medium containing microbubbles, and is used further in the following Chapters of this thesis.

Chapter 6

Experimental Sensitivity Analysis of Microbubble-enhanced NIRS

In Chapter 4 the modulation of light from a laser source by ultrasound was modelled and shown to be enhanced by the presence of microbubbles: these preliminary studies suggested that microbubbles may provide an increased modulation both with a coherent speckle detection approach and also a DC shift in light intensity. There were several questions outstanding from these results, and this chapter will attempt to address these.

Firstly the effect of microbubble concentration on the ultrasonic modulation was not investigated, and so the results cannot confirm whether an effect would be observed at clinically relevant concentrations. At concentrations above $\sim 2 \times 10^5$ mm^{-3} the assumptions of the acoustic model are no longer valid as multiple scattering becomes relevant [30, 125]. Several techniques have been used by other groups to quantify the number concentration of microbubbles in a suspension, and also to estimate their size distributions. One such technique uses electro-impedance sensing devices such as Coulter

counters [29,113,136]. Some groups have reported that the size distributions generated by this technique vary depending on the microbubble preparation method [106]. Other groups have used optical methods such as low-angle laser diffraction [66, 88]. Direct observation under optical microscopy is also well-established [8, 119] and continues to be a popular technique [3, 27]. A recent study [114] has shown that the variability in optical microscopy techniques is sufficiently low for it to provide useful estimates of microbubble size distribution and concentration, and so this approach was adopted in this work. In addition to the question of concentration, clinical standard (SonoVue) microbubbles were used and compared with the polymer-shelled Expancel bubbles investigated in the preliminary study.

The majority of experimental studies into the detection of ultrasound-modulated diffusive light [24] have focused on the phase modulation of coherent light, using either single-point autocorrelation detection [39,70,82,83], parallel detection methods [5, 71, 138], photorefractive crystal interferometry [90, 102] or a spectral filtering technique known as spectral hole burning [73]. A number of groups have also studied non-phase mechanisms which do not require coherent light. These mechanisms, which rely on local changes in absorption, scattering and refractive index in an insonified medium, have been modelled [37, 63, 78] and detected experimentally in the case of fluorescence [61]. Microbubbles have also been used by one group [139, 140] to provide signal enhancement to US-modulated fluorescence detection by modulating the quenching efficiency of the system. In this work however microbubbles are used directly as a contrast agent, providing additional optical scattering which can be modulated as a result of US-driven radial oscillations. Contrast agents such indocyanine green have been used previously [69] in biomedical NIR imaging to provide additional absorption in measurements of blood flow, but this work is the first example (to the author's knowledge) of a scattering contrast agent for NIRS. One group [40] has reported

an increase in a frequency-domain AO signal using microbubbles, however the detection method used in this work remains somewhat unclear. Pressure contrast techniques have also been used in AO imaging [64] to differentiate between first and higher order US-modulation: in the work described below a similar pressure contrast method was used to provide a differential NIRS signal from a microbubble filled phantom.

The sensitivity of the microbubble-enhanced optical attenuation signal to US pressure will also be addressed in this chapter. Whereas focused US is generally used to achieve high spatial resolution in phase-based AO imaging [90], in this technique the source of the modulated signal is defined by the location of the microbubble suspension, and so unfocused US is used to increase the volume over which modulation occurs. Although the optical properties of turbid media without microbubbles are also expected to be modulated by US, modelling suggests [78] that these non-phase mechanisms are two to three orders of magnitude smaller than similar phase-based AO effects, and so will be negligible compared with microbubble-enhanced modulation.

6.1 Experimental Protocol

6.1.1 Detection Geometry

The experimental studies discussed in this chapter involve transmittance measurements of NIR light transmitted through a clear silicone gel phantom (Encapso K). This phantom contains a cuboidal hollow filled with intralipid and a microbubble suspension to provide optical scattering and absorption. A schematic of this setup is given in figure 6.1. The silicone phantom was suspended above a water bath, with the lower surface of the phantom submerged by approximately 5 mm. The external and internal dimensions of this phantom are given in figure 6.2. The internal capacity of the phantom

was 18 mL.

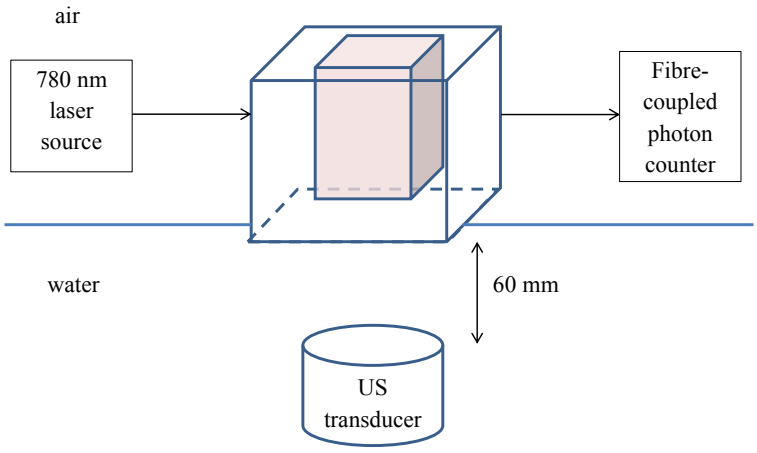

Figure 6.1: Experimental geometry, with hollow liquid-filled phantom in the centre.

6.1.2 Ultrasound Calibration

The US transducer used in this experiment was an A392S-SU Olympus immersion unfocused cylindrical transducer, with central frequency 1 MHz, nominal element diameter 39 mm. The transducer was positioned 60 mm below the phantom, as shown in figure 6.1, to avoid near-field effects. The input voltage was provided by an Agilent 33522A signal generator amplified by an RF amplifier. There is a limit to the driving voltage which can be supplied to this transducer to ensure that it does not overheat and depole the crystal [93]. Therefore the excitation voltage should provide no more than an average power of $P_{ave} = 125$ mW, which is related to the root mean square (RMS) voltage V_{rms} by:

$$P_{ave} = \frac{D_c V_{rms}^2}{Z} = \frac{D_c V_{p-p}^2}{8Z} \tag{6.1}$$

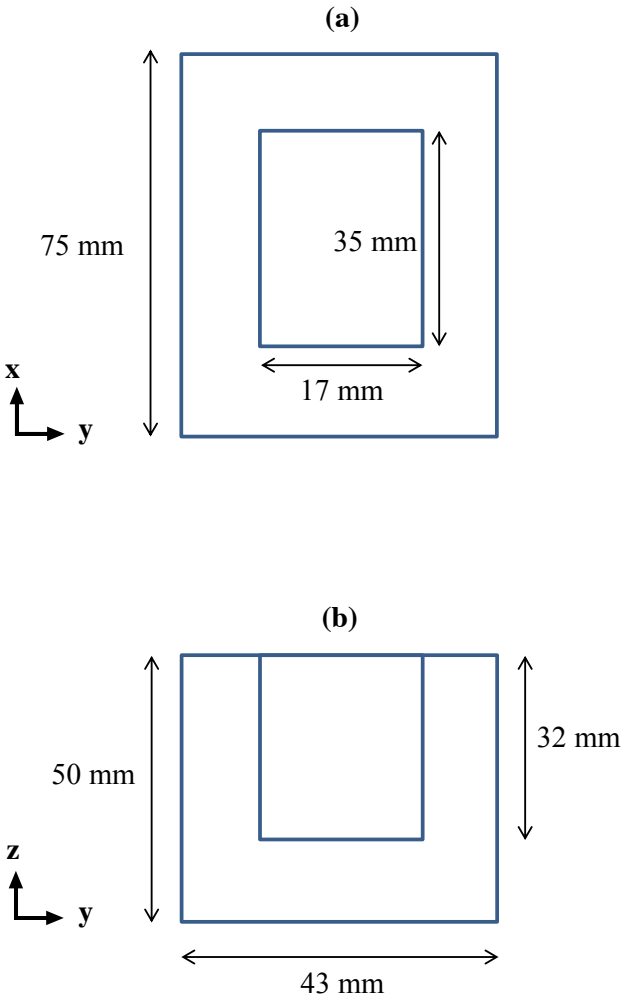

Figure 6.2: Dimensions of tissue phantom, viewed (a) from above, and (b) from the side.

where D_c is the duty cycle (i.e. the fraction of time for which the voltage is non-zero), $Z = 50\ \Omega$ is the impedance of the transducer and V_{p-p} is the peak-to-peak (P-P) input voltage. In this work, the signal generator is used to provide a burst of 5 cycles of a 1 MHz sinusoid, at a repetition frequency of f_{rep}. The maximum P-P voltage output by the signal generator is 270 mV, which is amplified by approximately 54.8 dB by the RF amplifier (1020L, RS, USA) to provide a maximum P-P input of 148 V to the US transducer. From equation 6.1 it is then possible to calculate the maximum duty cycle (and therefore the maximum repetition frequency) which can safely be used. This gives a maximum duty cycle of approximately $D_c = 0.25\%$. As explained in Section 6.1.3, the optical measurements with and without US present are taken in an interleaved way, so that the signal generator is only active for half of the total measurement period. Therefore twice this duty cycle was used. A duty cycle of $D_c = 0.5\%$ with a pulse length of 5μs corresponds to a repetition frequency of $f_{rep} = 1$ kHz.

A needle hydrophone (1 mm diameter, Precision Acoustics, USA) immersed in the liquid region of the phantom was used to measure the US beam profile, and to confirm that reflections from the top and sides of the phantom did not overlap with the incident pulse. The peak voltage measured by the hydrophone was used to estimate the peak negative pressure (PNP) within the phantom, given a calibration factor of 2302 mV MPa^{-1} (see table 6.1). The recorded US pulse in the middle of the phantom was also used to ensure that the optical detection system was active only while the phantom was insonified. This process is explained in the following section (6.1.3).

6.1.3 Optical Detection System

The laser source used in this study was a NIR laser (FCLM780.25-PLR48-H-MM, Ondax, USA) with a central wavelength of 780 nm. This was multimode fibre-coupled and fixed in position in the centre of the large face of

Pre-amplified input P-P voltage (mV)	Amplified input P-P voltage (V)	Hydrophone P-P voltage (mV)	US PNP (kPa)
20	11	34	7.4
50	27	79	17
100	55.0	174	37.8
150	82.4	266	57.8
200	110	372	80.8
230	126	432	93.8
270	148	512	111

Table 6.1: US transducer P-P input voltage, and the maximum P-P voltage recorded by the needle hydrophone. A conversion factor of 2302 mV MPa^{-1} was used to estimate the peak negative US pressure.

the phantom (see figure 6.1). The detector was a single photon detecting module (SPCM-AQRH-14-FC, Perkin Elmer, USA), which was coupled to the opposite side of the phantom by a multimode optical fibre. A neutral density filter (OD of 4) was fixed between the source and the phantom to avoid saturating the photon counter. The photon detector was connected to an analogue to digital converter (ADC, USB-6221, National Instruments, USA) which provided a digital count of the number of photons recorded.

As explained in Section 6.1.2, the duty cycle of the US pulses was very low (0.5%). In order to record only the US-modulated optical signal, time-gating was applied to the ADC so that photons were only counted while the phantom was insonified. This gating pulse was of the same duration and repetition frequency as the US input pulse but phase-shifted to account for the travel time of sound from the transducer to the phantom. A single-pulse counting mode built in to the hardware of the ADC (digital input PFI8) was used to record the number of pulses arriving from the photon detector. This responds to the increasing edge of a voltage spike and has a very high timing resolution [92] (50 ns) compared to the US frequency, so that photons are not 'lost' during the device's latency period. However the rate at which

this counter can be read from the hardware using LabView is the limiting factor in the timing resolution of this setup. The maximum sample rate is 250 kHz, so it is only possible to record the number of photons which have arrived within a 4 μs interval. Therefore information about the arrival times of individual photons cannot be retrieved, which limits the application of this technique to measuring mean light levels (DC signal) rather than measurements of optical correlation (AC signals). In this way the experiment could discriminate between photons which travelled through the medium while the microbubble suspension was insonified and those which arrived at the detector during the latency period between US pulses.

The average photon count was recorded both with US applied and in the absence of US. These measurements were taken in an interleaved pattern: for 5 seconds, US was applied with a 0.5% duty cycle and the photon count was recorded (with time-gating). For the following 5 seconds, the US was turned off and the photon count was recorded in a similar way. This process was repeated for a total of 30 seconds. After this point the phantom was lightly stirred to ensure the microbubbles were still well distributed, and the process repeated 10 times. The photon count was therefore averaged over 150 seconds in total to provide each measurement. For the duty cycle used here, this corresponds to $150 \times 0.005 = 0.75$s of time for which the photon counter was recording. This measurement pattern is summarised in figure 6.3.

The average photon count per second with US, proportional to I_{US}, and the photon count per second without US, proportional to I, were used to calculate a measure of microbubble-enhanced optical attenuation (MOA):

$$MOA = A_{US} - A = \log \frac{I_0}{I_{US}} - \log \frac{I_0}{I} = \log \frac{I}{I_{US}} \tag{6.2}$$

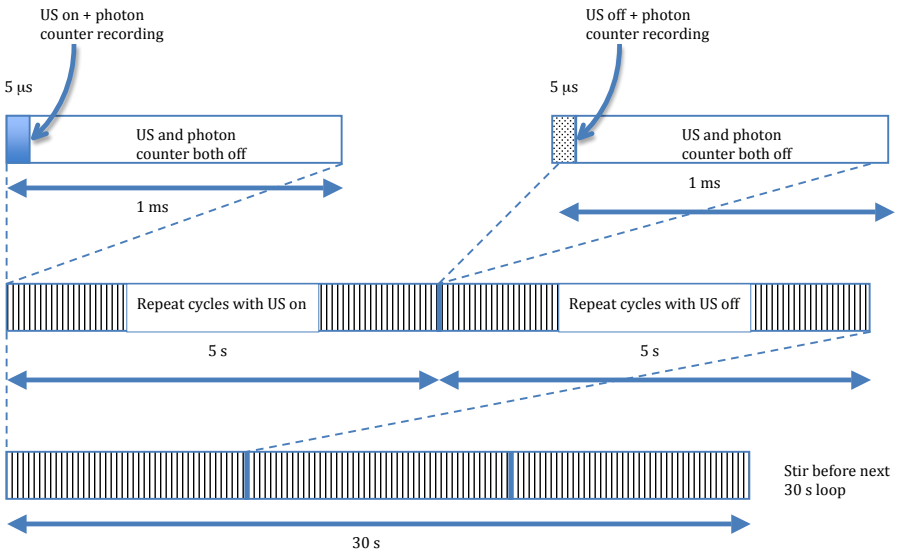

Figure 6.3: Diagram summarising the experimental protocol for each 30 second loop, in which photon counts with and without US are both recorded, switching between either mode every 5 seconds. In both modes, photons are only recorded for 5 μs in each 1 ms to allow cooling time for the US transducer.

as defined in Section 7.3. Figure 6.4 shows an example of the photon counts recorded using this experimental configuration. The mean photon arrival rates are calculated by taking a cumulative mean of each sample recorded, so that the uncertainty in the mean count reduces with time as each new sample is taken. The sample rate for the ADC is 100 Hz. From figure 6.4 it can also be seen that the difference in photon count recorded with and without US is signficant compared to the measurement uncertainty when microbubbles were used, but not significant where the phantom only contained intralipid.

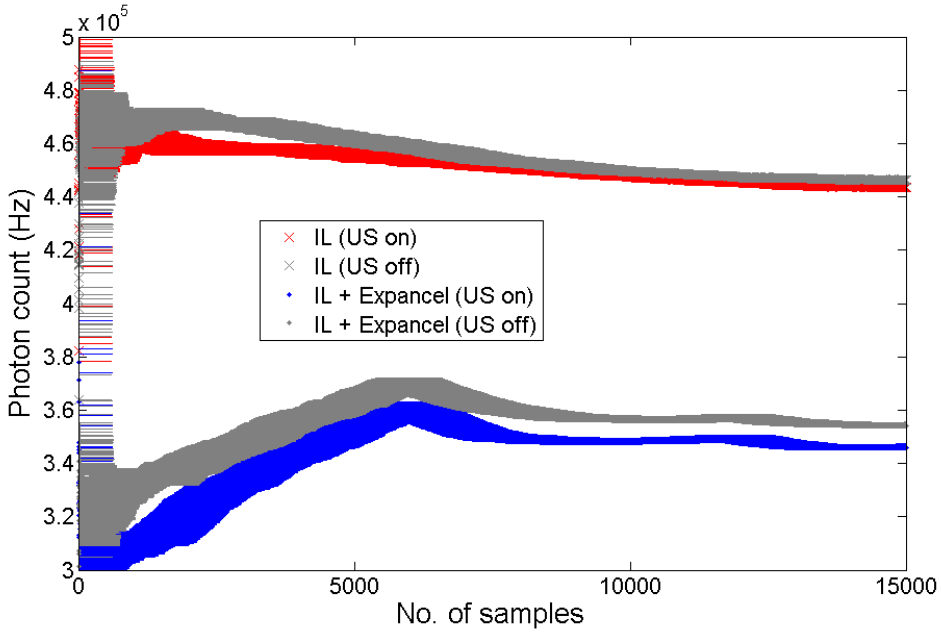

Figure 6.4: Cumulative mean photon count, calculated over all previous samples recorded by the ADC. The ADC sample rate is 100 Hz.

6.1.4 Quantifying Microbubble Concentration

Although other methods for measuring the concentration of a microbubble suspension have been discussed [29, 113, 136], optical microscopy has been

widely used [3, 74, 89, 114] and accepted as a reliable technique. Two different preparations of microbubbles were used in this study. SonoVue is a commonly used UCA for diagnostic US imaging, manufactured by Bracco UK Ltd. A clinical preparation of SonoVue consists of 25 mg of lyophilised powder which is reconstituted by mixing with 5 ml of sodium chloride solution (9 mg/ml, 0.9% w/v), forming phospholipid bubbles containing sulfur hexafluoride. This liquid suspension was prepared according to the instructions supplied by the manufacturer. Expancel consists of polymer gas bubbles used in industrial processes and is manufactured by Casco Products AB, Sweden. These bubbles have a mean radius of approximately 12 μm according to manufacturer specifications [125], which is larger than expected for a standard preparation of SonoVue (2.5-6 μm [89]). Expancel is supplied in powdered form, and was mixed with de-ionised water to form a suspension.

Optical measurements of these microbubble suspensions were made using a 400x magnification DS100 microscope (40x objective, 10x eyepiece) manufactured by VWR, with integrated 1.3 megapixel CCD camera. A sample was prepared for imaging using a haemocytometer (improved Neubauer, Weber, UK), which provides a square calibration grid in intervals of 0.05 mm. Following a procedure described by Sennoga *et al.* [114], 10 μL of microbubble suspension were introduced to either side of the haemocytometer counting chamber using a pipette. The sample was then left for 3 minutes to allow the microbubbles to float to the top of the haemocytometer. 50 microscope images were taken from the counting chamber for each sample, and a calibration factor of 0.188 μm pix^{-1} calculated by measuring the length in pixels of each 0.05 mm square. Images were analysed using LabVIEW software specifically written for this purpose. Other groups [3] have designed similar MATLAB-based software, however preliminary studies suggested that the contrast of the microscope images obtained varied too greatly for this software to provide a reliable estimate of microbubble concentrations. An

additional image processing stage was required to locally threshold each image in order to convert it into a 2 bit binary image without 'losing' bubbles which happened to lie in regions of low contrast. The bubble concentration ρ_b was estimated by counting the number of bubbles in 100 images; any bubbles smaller than 0.5 μm (estimated by measuring their diameter in pixels and applying the calibration factor 0.188 μm pix^{-1}) were assumed to be image artefacts or small impurities and were discarded. The total volume of fluid represented by each image was then calculated from the width of the square haemocytometer grating ($l = 0.05$ mm) and the depth of the counting platform ($d = 0.1$ mm), giving a bubble concentration of:

$$\rho_b = \frac{\sum_{i=1}^{n} N_i}{nl^2 d} \tag{6.3}$$

where N_i is the number of bubbles counted in the i^{th} image and n is the total number of images analysed.

The SonoVue manufacturer's guidelines suggest that a standard 5 ml preparation contains an average concentration of between 2 and 5×10^5 mm^{-3}. Figures 6.5 and 6.6 show examples of the microscopy images collected from a solution of Expancel and a standard preparation of SonoVue. The Expancel bubbles were generally larger and appear more opaque than those in the SonoVue suspension. The density of the SonoVue sample, as measured by the LabVIEW image analysis script, was $(1.60 \pm 0.02) \times 10^5$ mm^{-3}. This is slightly lower than that suggested by the manufacturer's instructions, but of the same order of magnitude.

In the case of SonoVue, this concentration was larger than the theoretical limit above which multiple scattering dominates, as derived in Section A.5, and was also larger than the concentrations reached *in vivo*. Therefore the

standard preparation was diluted in deionised water in the following studies to achieve lower concentrations.

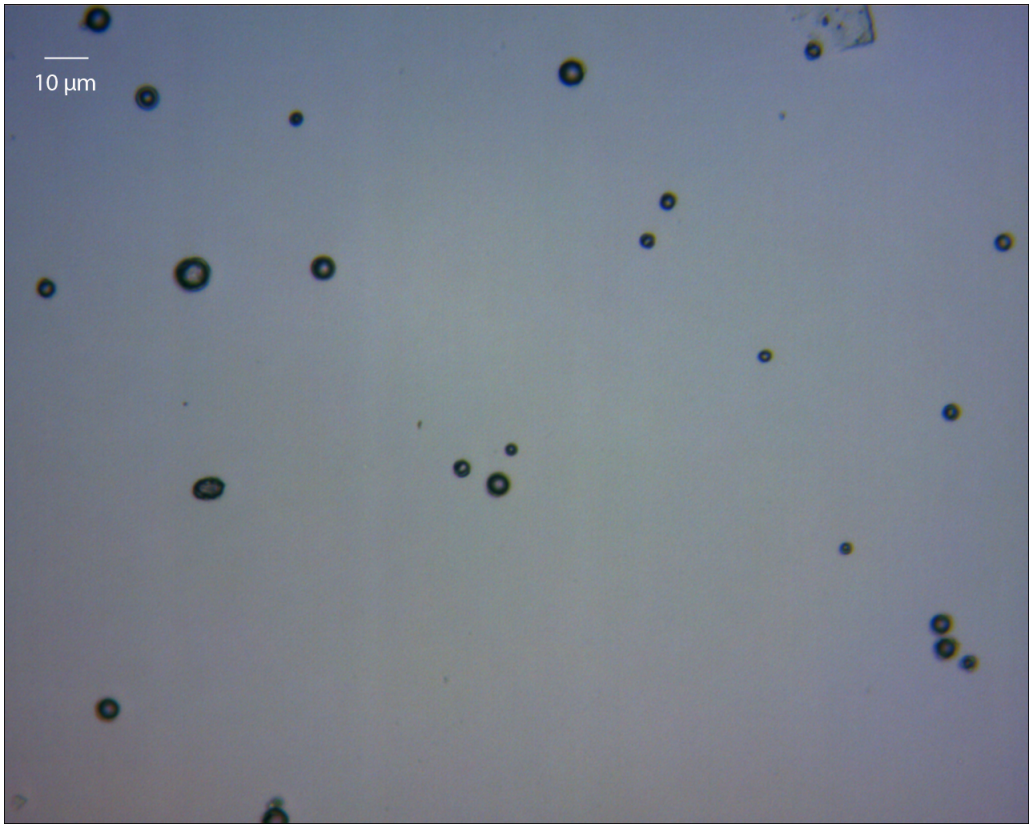

Figure 6.5: Microscopy image of an Expancel suspension, with measured ρ_b of 2×10^4 mm^{-3}.

Figure 6.7 shows a histogram of the radii of a SonoVue sample and of an Expancel sample. The mean radius of SonoVue microbubbles in this sample was 1.16 μm, and the mean radius of Expancel was 1.85 μm. In the case of SonoVue this radius was smaller than the manufacturer's guidelines suggest, but comparable with the sizes reported by other groups [3] who have used a similar optical microscopy approach.

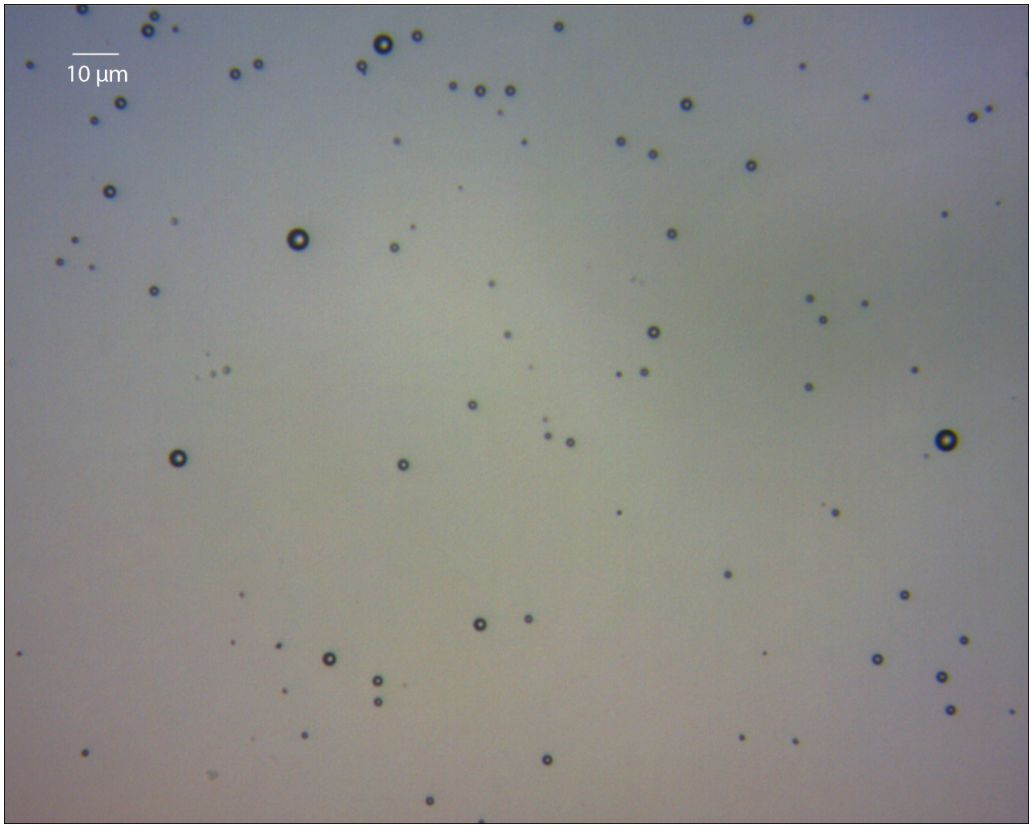

Figure 6.6: Microscopy image of a SonoVue suspension, with measured ρ_b of 1.6×10^5 mm^{-3}.

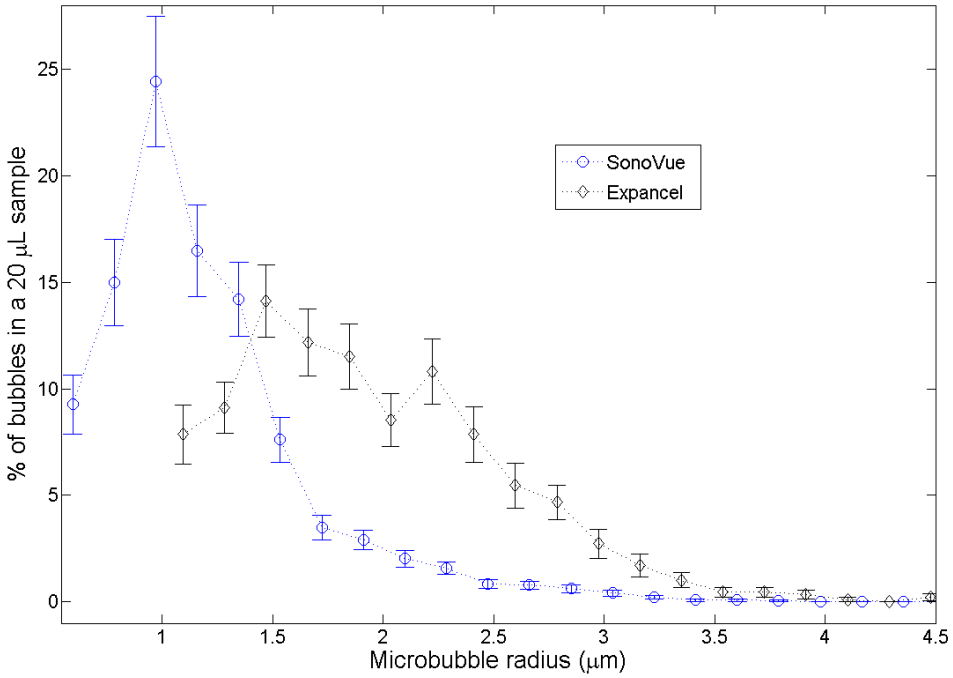

Figure 6.7: Histogram of the radii of microbubbles from suspensions of SonoVue and Expancel. The results are presented as the percentage of the total number of bubbles counted in that sample which have a radius within a given range (the width of each histogram bin is 0.2 μm).

6.1.5 Simulated Results

The experimental results presented below were compared with theoretical results produced by the Sumptuous Bubbles MC code. These comparisons are used to assess the validity of the MC code and of the theoretical description of microbubble-enhanced optical attenuation presented in Chapter 3, which underpins the simulations.

The simulation geometry consists of a finite element mesh with the same dimensions as the phantom, as given in figure 6.2. The external solid section of the phantom has negligible scattering and absorption properties, being made of clear silicone gel ($\mu_s = 0.01\text{cm}^{-1}$ and $\mu_a = 0.0001\text{cm}^{-1}$). The optical properties of the internal liquid section are derived from published scattering and absorption values for intralipid [121]. For a 0.1% solution of intralipid these properties are estimated to be $\mu_s = 4.8\text{cm}^{-1}$, $g = 0.77$ and $\mu_a = 0.011\text{cm}^{-1}$.

The presence of SonoVue microbubbles in this liquid section of the phantom provides additional scattering: this optical scattering is modulated by an applied US field. This field is modelled as a cylindrical beam of plane-wave US, with a diameter corresponding to the specifications of the US transducer used in this experiment (39 mm). Outside of this cylindrical beam the US pressure is assumed to be zero. The US field is centred on the bottom face of the phantom, and propagates upwards. The resulting spatially and temporally varying optical scattering of the insonified microbubbles is precalulated as described in Section 5.1.

The microbubble-enhanced optical attenuation is measured by recording the number of photons arriving at a circular area detector with a radius of 1 mm, centred on the face of the phantom opposite the source. This photon count is recorded for the cases where the US field is turned on and where it

is off, which provides a measurement of the MOA. An average is taken over five time points, equally spaced across one cycle of the US field. This gives the mean photon count detected with the US turned on, with 300 million photons used for each simulation.

6.2 Effect of US Pressure

In this section stock solutions of Expancel and SonoVue microbubbles were used, and the concentrations measured to be 2×10^4 mm^{-3} and 1×10^5 mm^{-3} respectively. In the case of the SonoVue solution, this has been diluted from the standard clinical preparation using deionised water. The silicone phantom was then filled with 9 ml of this stock solution and 9 ml of an intralipid stock solution, so that the resulting concentrations within the phantom were half of that in the stock solutions. The intralipid stock solution was prepared at a concentration of 0.2%, so that the phantom then contained 0.1% intralipid. This provides a background scattering coefficient of approximately 4.8 cm^{-1} [121].

The light intensities with and without US applied to the medium were measured according to the protocol described in Section 6.1.3. A range of US pressures were applied to assess the effect of pressure on the microbubble-enhanced change in optical attenuation (MOA). In each case the pressure was measured by needle hydrophone, and converted using a known calibration factor for the device (see table 6.1). These results are shown in figure 6.8. This demonstrates clearly that an AO modulated DC signal was not detectable above background noise without microbubbles present: with both Expancel and SonoVue this signal was significant and increased with applied US pressure. It can be inferred that microbubble destruction did not occur at the maximum pressure available from this transducer, 111 kPa with 5 cycle pulses, since the MOA signal was consistent, repeatable and significantly

different to the signal detected without microbubbles. This is consistent with other studies using SonoVue [22]. It should be noted when comparing the magnitudes of the MOA signals that the concentrations of SonoVue and Expancel were not equal.

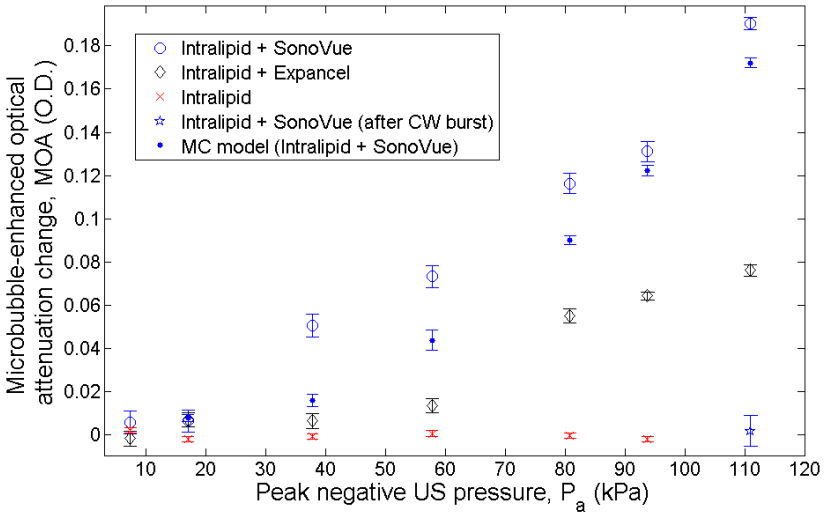

Figure 6.8: Experimental measurements of a microbubble-enhanced US-modulated NIR signal. The peak negative US pressure is varied and applied to suspensions of SonoVue and Expancel in intralipid, and also to intralipid without microbubbles as a control. The error bars are generated by finding the error in the mean from 10 repeated measurements. The MC results are only valid for the case of SonoVue microbubbles, since the parameters describing the microbubbles in the model are taken from experimental measurements of SonoVue. There are currently no published model parameters for Expancel microbubbles.

Following these measurements with SonoVue and short (5 cycle) US pulses, CW US of 0.11 MPa was applied to the phantom for 30 seconds. Many groups have observed that CW US can result in instability and destruction of microbubbles [72], even for lower pressures than those at which pulsed US routinely disrupts microbubbles [124]. Microscopy was performed

on a 20 μL sample taken from the phantom following this CW burst, confirming that few microbubbles remained: the concentration of microbubbles fell from 5×10^4 mm^{-3} to 5×10^3 mm^{-3}. The US-modulated optical signal was then recorded using the same protocol as described previously, using 5 cycle pulses at 0.11 MPa. Figure 6.8 shows that the MOA then falls to a level equivalent to a negligible microbubble concentration.

6.3 Effect of Microbubble Concentration

In the next part of the study, the sensitivity of the MOA signal to the concentration of microbubbles in the phantom was investigated. For each prepared suspension of Expancel and SonoVue, a bubble concentration ρ_b was estimated according to the process described in Section 6.1.4. Figure 6.9 shows the MOA signal measured for a range of concentrations of Expancel; figure 6.10 shows these results for suspensions of SonoVue microbubbles. In each case the input voltage for the US transducer was 230 mV P-P (before amplification), which was measured by needle hydrophone to result in a peak negative pressure of 93.8 kPa inside the liquid phantom.

From figures 6.9 and 6.10 it can be seen that below a critical concentration ρ_b no significant MOA is observable. This is of a similar order of magnitude for both Expancel and SonoVue ($0.4 - 0.6 \times 10^4 \text{mm}^{-3}$). The increase of MOA with ρ_b appears approximately linear at intermediate concentrations, but in the case of SonoVue becomes non-linear above approximately $3 \times 10^4 \text{mm}^{-3}$. It is known that as the concentration becomes sufficient that microbubbles are only several radii apart secondary radiation effects dominate [30, 125], and as such non-sphericity in bubble oscillations is expected. By comparing the magnitude of the MOA for SonoVue and Expancel suspensions of $1 \times 10^4 \text{mm}^{-3}$ it can be seen that the modulation due to Expancel is larger (approximately 0.07 compared with 0.02): this is consistent with the obser-

vation that Expancel microbubbles are larger and more opaque, therefore a higher optical scattering would be expected.

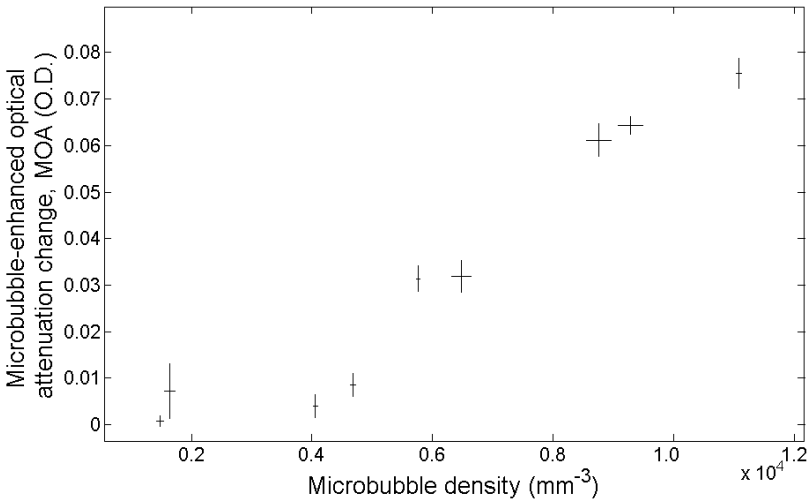

Figure 6.9: Experimental measurements of a microbubble-enhanced US-modulated NIR signal using Expancel suspensions of different concentrations.

6.4 Effect of Background Scattering

The effect of the background scattering of the medium in which the microbubbles are suspended is investigated in this section. A dilute (0.1%) intralipid solution provides background optical scattering of 4.8 cm^{-1} [121], which is of a similar order of magnitude as the scattering measured in some human tissues such as the forehead and abdomen [127]. By changing the dilution factor of the intralipid solution, this background scattering can be varied in order to demonstrate the sensitivity of a microbubble-enhanced NIR signal to this variable.

The intralipid concentration was varied from 0.1% up to 2.0%. Table 6.2 shows the estimated optical scattering provided by each solution of intralipid.

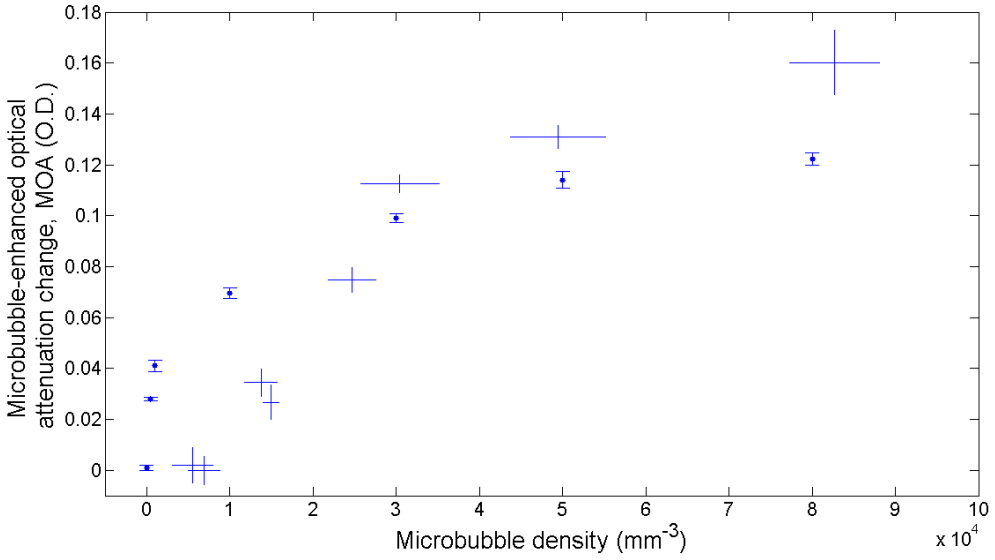

Figure 6.10: Experimental measurements of a microbubble-enhanced US-modulated NIR signal using SonoVue suspensions of different concentrations. Solid crosses show the experimental results, and the circles are corresponding MC simulations. (Simulated intralipid parameters: g =0.77, μ_s =4.8cm^{-1}, μ_a =0.011cm^{-1})

Intralipid concentration (%)	Effective μ_s (cm^{-1})
0.10	4.8
0.15	7.1
0.20	9.5
0.50	24
1.0	48
2.0	95

Table 6.2: Intralipid concentrations used in this study, with the estimated optical scattering provided by each solution [121].

Figure 6.11 shows the effect on the MOA signal of increasing the concentration of intralipid in the phantom. Increased background scattering reduces the MOA, until at around 20 cm^{-1} no significant signal is detected. The uncertainty in the measurement also increases as the scattering increases, since this is accompanied by a drop in the overall light intensities detected (both I and I_{US}). This result suggests that there is a limit on the optical scattering of a biological medium in which this technique could be successfully applied. Figure 6.11 shows that no signal can be detected over the noise floor from intralipid with effective scattering $\mu_s' = 24 \cdot (1 - 0.77) = 5.5 cm^{-1}$. The optical properties of tissue vary somewhat [32], but a recent study of breast tissue gives an estimate of $\mu_s' = 8.5 \pm 2.1 cm^{-1}$ (at 780 nm) [21]. It can be inferred from this that an *in vivo* measurement of MOA would require instrumentation at least as much resolving power as the photon counting setup used here. Of course the resolution of such an *in vivo* system would also depend on the geometry of the target blood vessel: in this case the measurement is taken in transmission mode through 17 mm of intralipid, whereas reflection mode is more appropriate *in vivo*. This question is addressed by the theoretical study presented in the following Chapter.

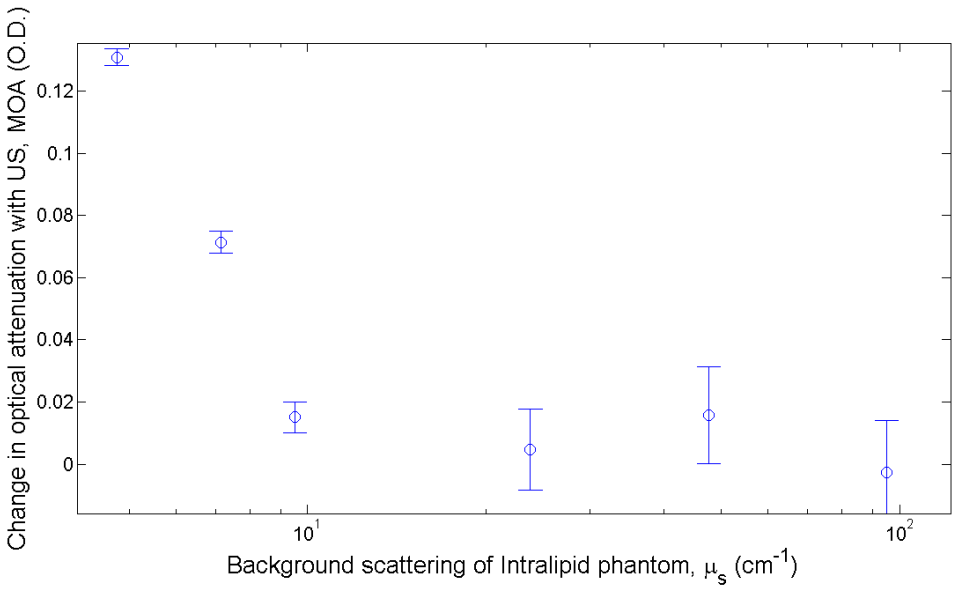

Figure 6.11: Experimental measurements of a microbubble-enhanced US-modulated NIR signal using SonoVue suspensions of different concentrations. There are no corresponding MC results available. This is because it is not possible to vary the scattering coefficient with the pMC model used here: in order to vary μ_s it is necessary to record the number of scattering events experienced by each photon in the simulation, which increases the computational time required.

Chapter Summary

- The concentrations of suspensions of Expancel and SonoVue microbubbles have been quantified by optical microscopy, and the size distributions are in agreement with manufacturer's values and previous studies.
- A microbubble-enhanced NIRS signal has been detected in transmission through a 17 mm of intralipid using unfocused US modulation.
- The magnitude of the MOA increased with applied US pressure in the case of both Expancel and SonoVue microbubbles.
- Above a critical microbubble concentration (which is comparable for populations of Expancel and SonoVue, around 5×10^3) the MOA magnitude increases with concentration, this relationship becoming increasing non-linear at high concentrations.
- As background scattering and absorption of the phantom increase this MOA signal becomes weaker, putting a limit on the types of turbid media or tissue in which this technique could be used ($\mu_s' = 5.5\text{cm}^{-1}$ in this case).

Chapter 7

Theoretical Study of Venous Oximetry Using Microbubble-enhanced NIRS

In this Chapter I will present a method for extracting an absolute measurement of venous oxygen saturation (S_vO_2) from an US-modulated NIR signal with microbubble contrast enhancement. The purpose of this is to investigate the limits of the experimental technique demonstrated in Chapter 6, and discuss whether it could be applied *in vivo* for clinical monitoring of S_vO_2. Using MC simulations of US-modulated light with microbubbles in a physiologically relevant geometry I will address questions such as whether it is possible to isolate the contribution from changes in oxygenation of a large blood vessel from changes in the surrounding tissue containing smaller vessels. This MC modelling technique will also provide an estimate of the magnitude of a microbubble-enhanced NIRS signal which can be detected from a highly absorbing blood vessel in reflection mode, to determine whether this is sufficient to be clinically useful.

Continuous clinical monitoring of tissue oxygen saturation (S_tO_2) using

NIRS is already regularly used [32]. NIRS has been used to successfully measure other haemodynamic variables such as cerebral blood volume and cerebral metabolic rate in neonates [105], however attempts to measure venous oxygen saturation have reported that standard NIRS techniques can only detect a linear combination of arterial and venous saturations [135]. Clinical measurement of central venous oxygen saturation (S_vO_2) in intensive care medicine generally requires an invasive catheter to be fitted, a procedure which carries significant patient risk [104]. This has motivated studies into non-invasive techniques such as NIRS and photoacoustic imaging [95], with limited success at present: recent work suggests that absolute central S_vO_2 cannot be accurately predicted by NIR measurements taken on the forehead [128], although relative changes can be predicted provided that bulk physiological changes do not occur. Further studies have shown that although regional NIRS measurements of SO_2 correlate with saturation changes in the right atrium, inferior vena cava, superior vena cava and pulmonary artery [7] they are not necessarily a predictor of absolute S_vO_2.

The approach taken in this Chapter is to model an US-modulated light signal detected from the pulmonary artery after an injection of microbubble contrast agent. Microbubbles are currently used clinically to improve the contrast in diagnostic US imaging in the pulmonary artery [34] and other areas of the heart. Preliminary simulations (see Chapter 4) have suggested that an US-modulated DC light signal enhanced by microbubbles correlates with absorption changes in a deep vessel, and so this situation is investigated further using a theoretical model. An algorithm based on the Modified Beer-Lambert Law is developed to extract an absolute measurement of S_vO_2 from a dual-wavelength microbubble-enhanced NIRS signal, modelled using the pMC code validated in Chapter 5.

7.1 Simulated Pulmonary Artery Measurements

In this section the Sumptuous Bubbles MC code, which was validated in Chapter 5, is used to simulate an AO measurement from a large blood vessel, such as the pulmonary artery. The turbid medium is defined by a tetrahedral mesh, composed of two broad classes of tissue type: blood, contained within a large (10 mm diameter) cylindrical vessel with high absorption, and tissue surrounding the blood vessel, with lower optical absorption. Microbubbles are added to the blood vessel, which increase optical scattering.

Photons are injected at a point source 10 mm above the centre of the blood vessel, and recorded at a 10 mm x 10 mm area detector positioned 20 mm from the source as shown by figure 7.1. Plane-wave US propagates downwards from the top surface of the tissue. This causes the microbubbles to oscillate radially as described in Chapter 3, with optical scattering $\mu_{s,b}(r,t)$ which now varies temporally and spatially in a constant phase relationship with the US. The weight of the photons is summed at the detector to create an intensity signal; phase-based modulation effects are not considered as the detection area is assumed to be large enough that any speckle pattern will be averaged out. The dimensions of the turbid medium are chosen to simulate a blood vessel with the same approximate diameter and depth as the pulmonary artery in adult humans [6, 95].

The MC procedure for calculating the free pathlength of a photon in a medium containing multiple populations of scatterers has been discussed in Section 5.1, and is summarised in figure 5.3. This process is repeated until the desired number of photons have been launched and recorded (in general approximately ten million or more photons are required to achieve a converging result). The sum of each photon's weight over the detection area is

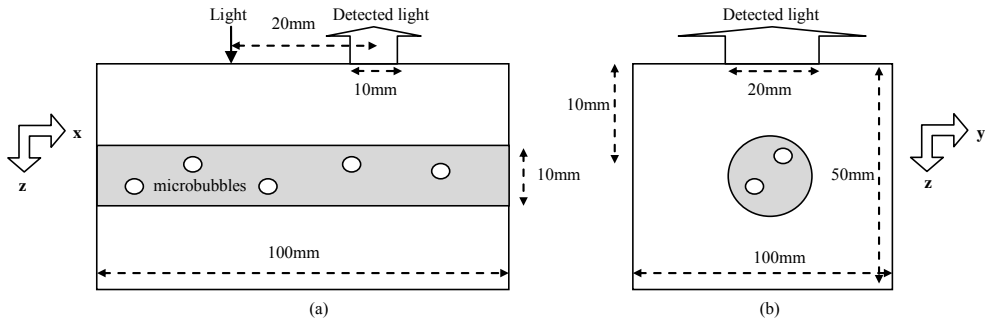

Figure 7.1: Simulation geometry, viewing the blood vessel from the side (a) and along its axis (b).

proportional to the detected light intensity.

The optical properties of the vessel and surrounding tissue are chosen to match the physiological parameters of the intended clinical target: the pulmonary artery. The optical absorption of the tissue is derived using a tissue hemoglobin concentration of 11 μM [69] and 70% water content. An additional background absorption accounting for other chromophores is added so that the total absorption matches in vivo measurements [118], with the optical scattering derived from these same measurements. The venous saturation S_vO_2 determines μ_a within the vessel, by assuming a fixed hemoglobin concentration of 14 g/dl. The hemoglobin concentration in the vessel is therefore 2200 μM. The optical scattering of blood and tissue are estimated using a model which describes the variation of μ_s with wavelength [69]. Although experimental studies report some variation in optical scattering between different types of tissue [118], this is comparable in magnitude with the variation between individual subjects observed in these studies. Therefore the optical scattering of tissue and blood is assumed to be homogeneous in this simulation. These properties are summarised in table 7.1.

	μ_s (cm^{-1}) 780 nm	μ_s (cm^{-1}) 810 nm	Anisotropy, g	SO_2 (%)	μ_a (cm^{-1}) 780 nm	μ_a (cm^{-1}) 810 nm
Tissue	29.5	28.2	0.85	30	0.190	0.184
				50	0.188	0.185
				70	0.187	0.185
				90	0.185	0.186
Blood	29.5+$\mu_{s,b}$	28.2+$\mu_{s,b}$	0.85	30	5.04	4.24
				50	4.66	4.38
				70	4.29	4.51
				90	3.92	4.64

Table 7.1: Parameters for the optical properties of the blood vessel and surrounding tissue in the Sumptuous Bubbles MC model (for λ_1=780 nm and λ_2=810 nm).

7.2 Near-infrared Algorithm for Quantitative Oximetry

Before we consider an acousto-optic method for measuring venous oxygenation, this section will outline how this problem could be approached using a NIRS technique. NIRS is widely used clinically to monitor the oxygenation of tissue [32], and here the difficulties in applying this technique to a large deep blood vessel are discussed. An algorithm for measuring oxygenation in a blood vessel will be derived based on a NIR signal, and the accuracy of this technique in predicting this oxygenation from simulated data will be used as a baseline for judging the success of the AO algorithm developed in Section 7.3.

7.2.1 Derivation

The basis for the NIRS approach to measuring oxygen saturation is the modified Beer-Lambert Law (MBLL), which can be applied to an inhomogeneous medium [44]. As figure 7.1 shows, in this work we consider the simple scenario

of a medium seperated into two compartments: the blood vessel, and the surrounding tissue. The oxygenation of the blood vessel (S_vO_2) contributes to a NIRS signal since it relates to the concentrations of oxyhemoglobin (c_{HbO_2}) and deoxyhemoglobin (c_{HHb}). This therefore affects the optical absorption within the blood vessel for a photon travelling on a diffuse path from the optical source to optical detector, with a mean partial pathlength (PPL) within the vessel of l_v. Similarly, the absorption of the surrounding tissue ($\mu_{a,t}$) will depend on the concentrations of chromophores and therefore on the tissue oxygen saturation (S_tO_2) and on the PPL outside the vessel (l_t). Whilst this would in reality vary spatially and with tissue type, here we assume a bulk average value across the tissue surrounding the blood vessel. The MBLL applied to this inhomogeneous but compartmentalised medium can be written as:

$$A_\lambda = l_{v,\lambda}\left[c_{HbO_2}\alpha_{HbO_2,\lambda} + c_{HHb}\alpha_{HHb,\lambda}\right] + l_{t,\lambda}\mu_{a,t}(\lambda, S_tO_2) + G_\lambda \qquad (7.1)$$

where A_λ is the optical attenuation at wavelength λ, $\alpha_{HbO_2/HHb,\lambda}$ is the specific absorption coefficient of each choromophore, and the absorption in the tissue is assumed to be homogeneous and a function of the bulk tissue oxygenation S_tO_2 and of λ. G_λ is an additional wavelength-dependent term which accounts for energy removed from the detected signal due to scattering [19].

When applying equation 7.1 to a measurement of blood vessel S_vO_2, the contribution to the attenuation from the tissue and from scattering are generally unknown. To account for these additional factors, a calibration approach is used in this algorithm: the attenuation due to the tissue and due to the scattering can be absorbed into a single new parameter, T'_λ. This factor can be estimated by fitting a known set of calibration data to the model and applying linear regression. Equation 7.1 can be rewritten in the form

$$A_\lambda = l_{v,\lambda} c_{HbT} \left[\alpha_{HHb,\lambda} + \left(\alpha_{HbO_2,\lambda} - \alpha_{HHb,\lambda}\right) S_v O_2\right] + T'_\lambda \tag{7.2}$$

where c_{HbT} is the total hemoglobin concentration in the blood vessel, and where:

$$S_v O_2 = \frac{c_{HbO_2}}{c_{HbO_2} + c_{HHb}}. \tag{7.3}$$

This linear regression fit using calibration data can also be used to estimate the PPL $l_{v,\lambda}$, which is also expected to be wavelength dependent. Once these two calibration parameters are estimated for both wavelengths in a dual wavelength NIRS measurement, equation 7.1 can be expressed in a matrix form and inverted to recover the hemoglobin concentrations c_{HbO_2} and c_{HHb}:

$$\begin{pmatrix} c_{HbO_2} \\ \\ c_{HHb} \end{pmatrix} = \begin{pmatrix} \alpha_{HbO_2,\lambda 1} & \alpha_{HHb,\lambda 1} \\ \\ \alpha_{HbO_2,\lambda 2} & \alpha_{HHb,\lambda 2} \end{pmatrix}^{-1} \cdot \begin{pmatrix} \frac{A_{\lambda 1} - T'_{\lambda 1}}{l_{v,\lambda 1}} \\ \\ \frac{A_{\lambda 2} - T'_{\lambda 2}}{l_{v,\lambda 2}} \end{pmatrix}. \tag{7.4}$$

where λ_1 and λ_2 are the two NIR wavelengths to be tested. In general, the total hemoglobin concentration in the blood vessel c_{HbT} is likely to be unknown. Therefore, from equation 7.2, only the ratio of the PPLs for the two wavelengths $l_{v,\lambda 1}/l_{v,\lambda 2}$ can be accurately estimated. The total hemoglobin concentration is removed when calculating the venous oxygen saturation (see equation 7.3).

7.2.2 Calibration

Calibration techniques are often used to remove the effect of unknown constants in analytical models of oxygen saturation, such as the attenuation to optical scattering [25]. In this model, the factors which need to be estimated before the model can be applied are the attenuation due to the surrounding tissue T'_λ and the mean pathlength of photons within the blood vessel $l_{v,\lambda}$. The MC model of a blood vessel described in Section 7.1 was initially used to generate a set of data with which to estimate the calibration factors T'_λ and $l_{v,\lambda}$ for two wavelengths: $\lambda_1 = 780$ nm and $\lambda_2 = 810$ nm. The perturbation MC approach was used to calculate optical measurements over a range of S_vO_2 values from a single set of data, which considerably reduces the amount of computational time required to generate these results. Each simulation consists of 50 million photons, with the total optical attenuation at the detector calculated from the sum of the weights of all detected photons and the sum of the initial photon weights using the definition $A = \log(\frac{I_0}{I})$.

	T' (O.D.)	$c_{HbT} \cdot l_v$ (m μM)
$\lambda_1 = 780$ nm	5.83	0.937
$\lambda_2 = 810$ nm	5.78	0.871

Table 7.2: Estimates for the optical attenuation of the surrounding tissue (T'_λ) and the pathlength in the blood vessel (l_v) obtained by fitting calibration data to the linear model.

Figure 7.2 shows the result of fitting these sets of calibration data to the linear model proposed in the previous section (equation 7.2). Four values of S_vO_2 were chosen, $S_vO_2 = \{0.55,0.65,0.75,0.85\}$, which correspond to a physiologically typical range for a large vein [116]. The tissue saturation is kept constant at $S_tO_2 = 0.75$. The estimates for T'_λ and l_v obtained from this linear fit are given in table 7.2. The PPLs l_v are scaled by the total hemoglobin concentration c_{HbT}: however since only their ratios are important for the calibration procedure, the value of c_{HbT} may be unknown. As this

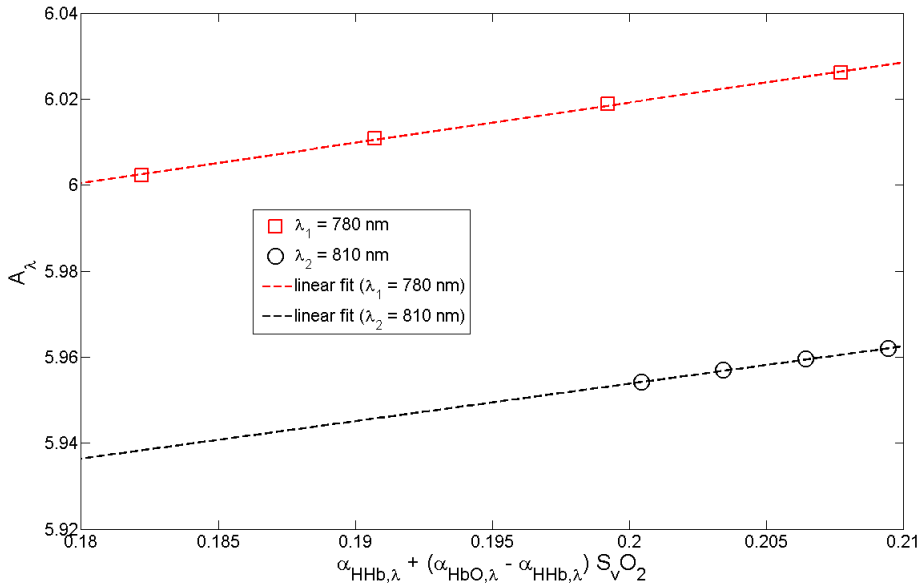

Figure 7.2: The MC data for attenuation A over a range of vessel oxygenation values S_vO_2 is fitted to the NIR linear calibration model. This process is repeated for both wavelengths λ_1 and λ_2 to estimate the calibration factors for each wavelength.

investigation is using simulated data, the concentration in the vessel has been fixed at $c_{HbT} = 2200$ μM.

7.2.3 Testing

The algorithm is now tested using a new set of independent simulated data, which corresponds to S_vO_2 in the range $\{0.3,0.4,0.5,0.6,0.7,0.8,0.9\}$. This was chosen to be wider than the range spanned by the calibration data, to assess how well the algorithm performs at extremes of S_vO_2. The tissue oxygenation is also now varied over the range $S_tO_2 = \{0.5,0.6,0.7,0.8,0.9\}$ to test the specificity of the algorithm in the case where oxygenation changes occur not only in the blood vessel.

Figure 7.3 shows the results of applying this calibrated NIRS algorithm to the set of test data. Where the tissue oxygenation is close to the value used in calibration ($S_tO_2 = 0.75$) the algorithm is able to approximately predict S_vO_2. However as the tissue oxygenation varies the predicted S_vO_2 diverges rapidly from the actual value, indicating that the NIRS technique is not robust to changes in oxygenation outside the target blood vessel.

7.3 Acousto-optic Algorithm for Quantitative Oximetry

In this section an AO algorithm for measuring blood vessel oxygenation will be derived, calibrated and tested against simulated data using a similar approach as was used in applying the NIRS algorithm (Section 7.2). The sensitivity of this algorithm to changes in S_vO_2, and the specificity in the case where S_tO_2 also varies will both be compared to the performance of the NIRS algorithm.

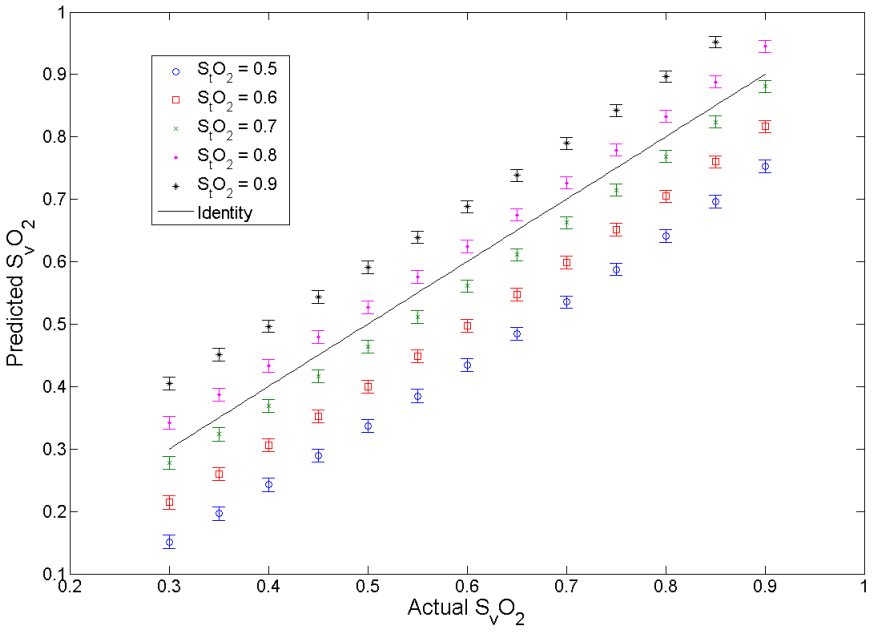

Figure 7.3: Results of measuring S_vO_2 using the calibrated NIRS algorithm. This is sensitive to oxygenation changes in both the blood vessel and the surrounding tissue, and does not provide a specific measurement of S_vO_2 in the case where the tissue oxygenation also varies. The identity line indicates what would be a perfect match between the real and predicted values.

7.3.1 Derivation

The AO signal used in this technique is the microbubble-enhanced change in optical attenuation induced by US-modulation:

$$MOA = A_{US} - A = \log \frac{I_0}{I_{US}} - \log \frac{I_0}{I} = \log \frac{I}{I_{US}} \tag{7.5}$$

where MOA is defined as the microbubble-enhanced optical attenuation, A_{US} and I_{US} are the optical attenuation and intensity after application of an US-field, and I is the detected intensity without US-modulation. Since microbubble size and therefore optical scattering vary significantly under US, intravenous microbubbles are expected to contribute to this US-modulated light signal.

The MBLL for this medium containing tissue and a blood vessel was described in the previous section, giving an expression for the optical attenuation for a given oxygenation in the vessel and tissue (see equation 7.1). This can be substituted into equation 7.5 for the case where a small change in attenuation is detected due to US-modulation of the optical field, giving:

$$MOA_\lambda = \Delta l_{v,\lambda} \left[c_{HbO_2} \alpha_{HbO_2,\lambda} + c_{HHb} \alpha_{HHb,\lambda} \right] + \Delta l_{t,\lambda} \mu_{a,t}(\lambda, S_t O_2) + \Delta G_\lambda \tag{7.6}$$

where Δ indicates a change in the property as a result of US-modulation, e.g. $\Delta l_v = l_{v,US} - l_v$ is the US-induced change in partial pathlength. This expression contains unknown terms which correspond to the US-induced change in the tissue attenuation ($\Delta l_{t,\lambda} \mu_{a,t}$), and also due to scattering changes (ΔG). This two terms are difficult to isolate, and so the approach used here is to combine these two terms into an unknown parameter T_λ:

$$MOA_\lambda = \Delta l_{v,\lambda} \left[c_{HbO_2} \alpha_{HbO_2,\lambda} + c_{HHb} \alpha_{HHb,\lambda} \right] + T_\lambda \tag{7.7}$$

This must be determined by fitting calibration data to the model. Equation 7.7 can then be expressed in terms of the vessel oxygenation S_vO_2, and measurements of MOA_λ for a known range of S_vO_2 can be fitted to the following by linear regression:

$$MOA_\lambda = \Delta l_{v,\lambda} c_{HbT} \left[\alpha_{HHb,\lambda} + \left(\alpha_{HbO_2,\lambda} - \alpha_{HHb,\lambda} \right) S_vO_2 \right] + T_\lambda. \tag{7.8}$$

This expression is then inverted to determine the concentrations of oxyhemoglobin and deoxyhemoglobin in the blood vessel:

$$\begin{pmatrix} c_{HbO_2} \\ \\ c_{HHb} \end{pmatrix} = \begin{pmatrix} \alpha_{HbO_2,\lambda 1} & \alpha_{HHb,\lambda 1} \\ \\ \alpha_{HbO_2,\lambda 2} & \alpha_{HHb,\lambda 2} \end{pmatrix}^{-1} \cdot \begin{pmatrix} \frac{MOA_{\lambda 1} - T_{\lambda 1}}{\Delta l_{v,\lambda 1}} \\ \\ \frac{MOA_{\lambda 2} - T_{\lambda 2}}{\Delta l_{v,\lambda 2}} \end{pmatrix}. \tag{7.9}$$

where an AO measurement is made at two wavelengths, λ_1 and λ_2. The differential PPLs for each of these wavelengths must also first be estimated by fitting a set of calibration data to equation 7.8. This calibration process is performed in the following section.

7.3.2 Calibration

An initial set of calibration data is first generated by the MC model. For each wavelength the detected light intensity without US I and the light intensity with US-modulation I_{US} are both required to calculate MOA. Since the optical properties of microbubbles will vary across each acoustic cycle with the temporal phase of the US wave, the light intensity I_{US} used

here is the average across an acoustic cycle: the simulation is repeated for t=$\{0,0.2T_a,0.4T_a,0.6T_a,0.8T_a\}$ and an average value of the detected intensity taken, where T_a is the period of the US. The acousto-optic modulation parameter MOA is then found from $MOA = \log \frac{I}{I_{US}}$. This is repeated for four values of S_vO_2=$\{0.55,0.65,0.75,0.85\}$, and this calibration data is fitted to the linear model (equation 7.8).

Table 7.3 gives the values for the fit parameters T_λ and Δl_v obtained from this model, where the differential PPL is again scaled by the total hemoglobin concentration in the vessel c_{HbT}. Figure 7.4 demonstrates that the MOA simulated data is consistent with the linear model derived in the previous section.

	T (O.D.)	$c_{HbT} \cdot \Delta l_v$ (m μM)
λ_1 = 780 nm	-0.0261	0.0258
λ_2 = 810 nm	-0.0252	0.0277

Table 7.3: Estimates for the US-modulated change in attenuation of the surrounding tissue (T_λ) and the differential pathlength in the blood vessel (Δl_v) obtained by fitting calibration data to the linear model.

7.3.3 Testing

The pMC model is now used to generate a new set of data with which to test the calibrated AO model. The range of S_vO_2 is again widened to test the robustness of the model in situations for which it has not been explicitly calibrated. The tissue oxygenation S_tO_2 is also varied, to determine whether the algorithm can still reliably estimate the venous saturation when changes in oxygenation outside of the blood vessel are also present.

From figure 7.5 it can be seen that the predicted results for S_vO_2 are close to the actual values used to define the optical properties of the simulation.

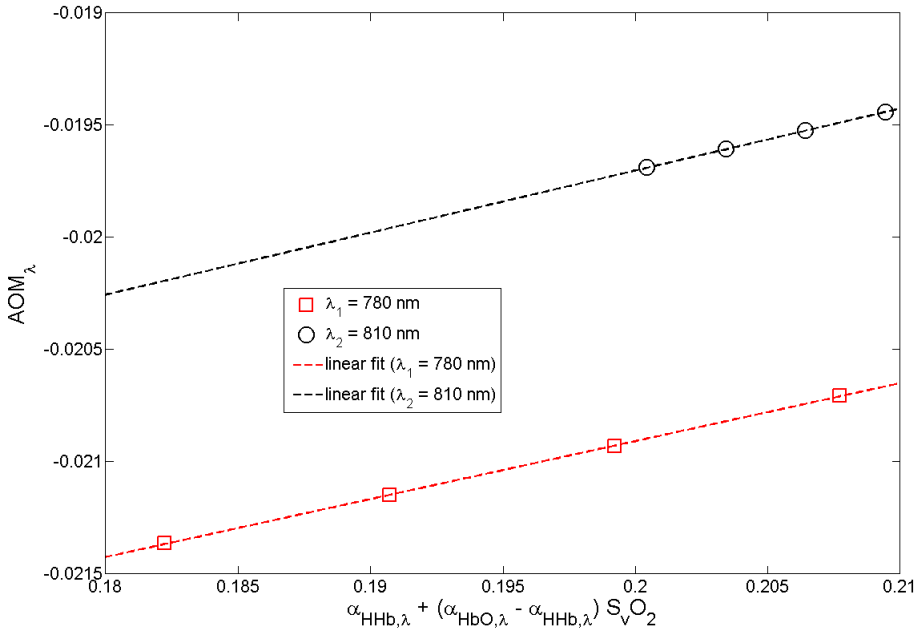

Figure 7.4: The MC data for attenuation A over a range of vessel oxygenation values S_vO_2 is fitted to the AO linear calibration model. This process is repeated for both wavelengths λ_1 and λ_2 to estimate the calibration factors for each wavelength.

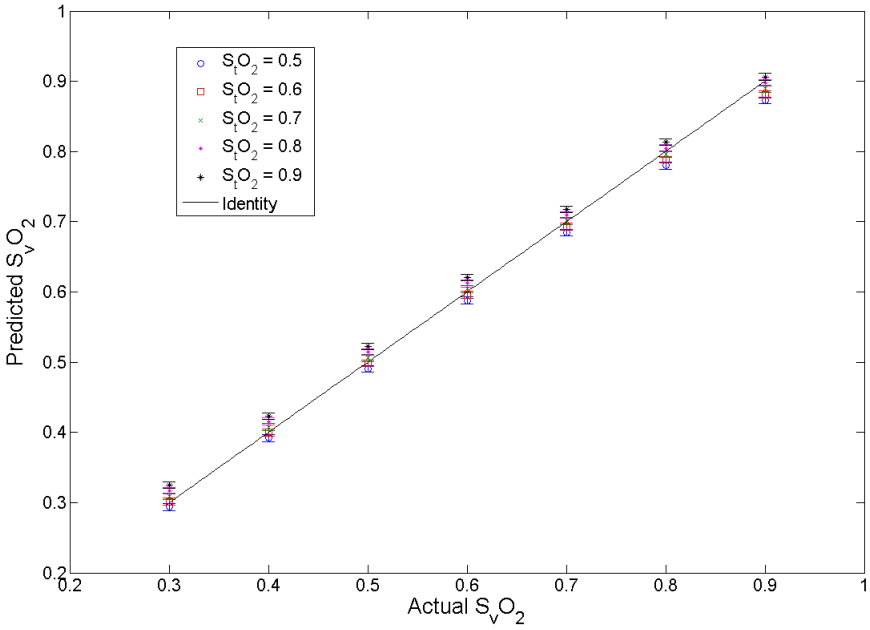

Figure 7.5: Results of measuring S_vO_2 using the calibrated AO algorithm. This measure is sensitive to changes within the blood vessel, and insensitive to changes in S_tO_2 of the surrounding tissue. The identity line indicates a perfect result.

Furthermore, this measurement is robust to changes outside the blood vessel, and provides a specific measure of S_vO_2. The explanation for this is likely to be that the microbubble contrast injection is localised to within the blood vessel: therefore US-induced modulation of light passing through the medium will be mostly enhanced by microbubble contrast within the blood vessel, and so the AO signal will be more sensitive to changes of venous oxygenation than to changes within the superficial tissue.

7.4 Error analysis

The errors in the predictions made by the NIR and MOA techniques are compared in this section. The difference between the actual S_vO_2 and the measured value S_vO_2' is presented as an average over all values of S_vO_2 tested ($0.3 < S_vO_2 < 0.9$) and all values of S_tO_2 ($0.5 < S_tO_2 < 0.9$). The metric used to quantify the error of each technique is the root mean square error (RMSE), given in this case by:

$$RMSE(S_vO_2') = \sqrt{\frac{\sum_i \sum_j \left[S_vO_2'(i,j) - S_vO_2(i,j)\right]^2}{N}} \tag{7.10}$$

where the index i indicates a sum over each S_vO_2 value tested, $\{0.3,0.4,0.5,0.6,0.7,0.8,0.9\}$, index j corresponds to the sum over each S_tO_2 value tested,
$\{0.5,0.6,0.7,0.8,0.9\}$, and N is the total number of points tested.

7.4.1 Effect of vessel depth

For a blood vessel 10 mm below the surface, the average error in the S_vO_2 value predicted by the MOA algorithm is 1.3%, compared with an error of

8.8% in the estimate provided by the NIR algorithm without US-modulation. This difference in performance of the two algorithms diverges further as we consider a deeper blood vessel: table 7.4 shows the mean error of each technique for blood vessels of three different depths. Each algorithm is tested in the same way, by calibrating it to a situation in which the surrounding S_tO_2 = 0.75, and then testing the robustness of the algorithm when the actual tissue oxygenation can vary in the range 0.5< S_tO_2 <0.9. This shows that with a superficial vessel (10 mm depth), NIRS provides a less accurate but still plausible value for the vessel oxygenation. Below this depth, the AO algorithm continues to perform well (2.3% error), but the NIRS algorithm does not deliver a useful result. Below 15 mm the AO algorithm also fails completely. This failure can be explained by the signal-to-noise ratio of the MOA signal compared with the optical A: when taking the difference between the attenuation with and without US (see equation 7.5), if this difference is comparable with the noise level then the uncertainty in the MOA will be very large. Therefore the algorithm will fail to generate a precise estimate of the calibration parameters as defined in Section 7.3.2. Therefore although the MOA signal is sensitive to S_vO_2 changes, signal-to-noise becomes limiting for deep blood vessels. Conversely, the NIR technique does not suffer from severe signal-to-noise issues at a depth of 20 mm, but instead fails to give an accurate result when S_tO_2 is not constant due to its lack of specificity to S_vO_2 changes. Of course in this theoretical study the noise level could have been reduced by increasing the number of photons simulated, however the noise in a detection system would still be the main factor which would limit the penetration depth of any *in vivo* study using this technique.

7.4.2 Effect of noise

The failure of the MOA algorithm to accurately estimate S_vO_2 in blood vessels below 15 mm is a result of the loss of specificity of the algorithm when

Depth of blood vessel (mm)	RMSE in predicted S_vO_2 using NIRS (%)	RMSE in predicted S_vO_2 using AO algorithm (%)
10	8.8	1.3
15	50	2.3
20	59	-

Table 7.4: RMSE in the predicted S_vO_2 value, when the algorithm is calibrated using a tissue oxygenation of 0.75 and tested with a tissue oxygenation which can vary in the range $0.5 < S_tO_2 < 0.9$.

the S_tO_2 also changes. A realistic model of a microbubble-enhanced optical measurement must also consider noise due to instrumentation. Noise is now added to the simulation results by adding a term to each light intensity measurement produced by the MC model. Noise in photon detection instruments is generally assumed to follow a Gaussian distribution [111] due to the central limit theorem of statistics, since we are considering a large number of detection events. The noise level can be characterised by the noise-to-signal ratio, or the ratio of the noise intensity at one standard deviation from the mean I_N to the mean light intensity I:

$$\frac{I_N}{I} = 10^{N_{dB}/10} \tag{7.11}$$

where N_{dB} is this noise-to-signal ratio expressed in decibels (e.g. $N_{dB} = -10$ dB indicates that the noise level at one standard deviation from the mean is a tenth of the light intensity level). This investigation will consider the effect of noise of a given level N_{dB} on the RMSE of both the NIRS and MOA techniques. For a given noise level N_{dB}, noise can be added to the detected light intensities as follows:

$$I' = I(1 + 10^{N_{dB}/10}\Gamma) \tag{7.12}$$

where I is the light intensity without noise and Γ is a random variable drawn from a standard Gaussian distribution (zero expectation, unit variance) with probability:

$$p(\Gamma) = \frac{1}{2\pi} \exp -\Gamma^2/2. \tag{7.13}$$

There is no closed analytical form for the cumulative Gaussian probability distribution, and so the Box-Muller transform [12] is often used to generate the random variable Γ:

$$\Gamma = \sqrt{-2 \ln U_1} \cos(2\pi U_2) \tag{7.14}$$

where U_1 and U_2 are both independent random variables with a uniform distribution on the interval (0,1]. The effect of measurement noise on the ability of the MOA and NIR algorithms to predict S_vO_2 is assessed here by calculating the RMSE in the measurement according to equation 7.10. The RMSEs with noise levels ranging from -43 dB to -30 dB are shown in figure 7.6. This shows that when the noise level is below around -35 dB, the MOA algorithm is more accurate than the NIR method. The RMSE in the NIR algorithm does not vary greatly with noise level here, whereas the RMSE in the MOA algorithm increases rapidly above -35 dB: this can be explained since the MOA algorithm relies on measuring the logarithm of the small change in light intensity with and without US, which will therefore be very sensitive to changes in either measurement. The NIR algorithm conversely uses the absolute magnitude of the light intensity to estimate S_vO_2, and so will be less sensitive to instrumentation noise. To estimate the noise level expected in an optical detection system, consider the single photon detecting module used in Chapter 7 (SPCM-AQRH-14-FC, Perkin Elmer, USA): the manufacturer's documentation states that the dark count expected is 100 ± 10

counts/second. This suggests that the variation in the photon count expected due to noise is around 10 counts/second. In the experiments of Chapter 7, the average photon counts detected were of the order of 10^5 counts/second. The noise level in these measurements is therefore approximately -40 dB. Figure shows that the RMSE in the MOA algorithm is less than half of the RMSE in the NIR algorithm in this regime. It can also be noted that at low noise levels (below -42 dB) the RMSE approaches that for a 10 mm deep blood vessel without noise (see table 7.4).

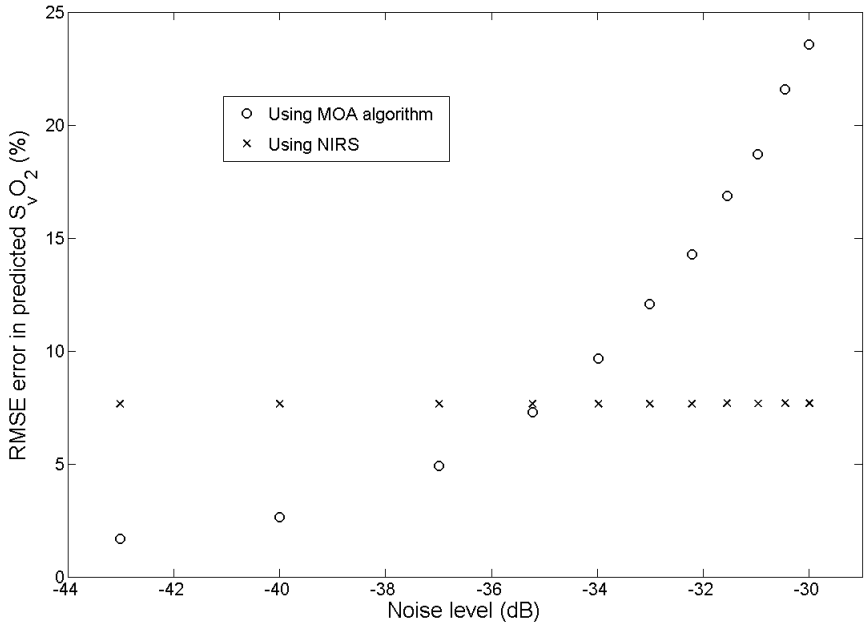

Figure 7.6: RMSE of the MOA and NIR algorithm in estimating S_vO_2 for a range of noise levels.

These investigations therefore show that the MOA algorithm is more accurate than the NIR method when used to measure S_vO_2 from a blood vessel within 15 mm of the tissue surface. This has been explained by showing that the MOA algorithm is more specific to S_vO_2 when S_tO_2 is not constant

than NIRS, provided that instrumentation noise levels are below around -35 dB. However in detection systems with high noise levels the MOA algorithm performs less well than the NIRS alternative. Similar observations about the penetration depth of NIRS and AO measurements have been made in another recent study [39]: this showed that an AO signal (measured in reflection mode using a digital correlator) had a mean penetration depth of 14.8 mm, compared with 11.4 mm for an optical signal. This is broadly in agreement with the findings of the theoretical study presented here, although the mechanisms of US-modulation and the detection technique are of course different.

These results suggest that this proposed technique of microbubble-enhanced US-modulated NIRS could provide a more accurate measure of absolute venous oxygenation from large blood vessels which are up to 15 mm below the surface of the skin, such as the pulmonary artery [95] or jugular vein [6], which cannot currently be measured to a satisfactory accuracy using NIRS [91]. Significant additional challenges remain to applying this technique *in vivo*, and these will be discussed in the final Chapter of this thesis.

Chapter Summary

- A pMC model is used to simulate a dual-wavelength NIR measurement from a large blood vessel containing an intravenous microbubble contrast agent with US applied from a transducer at the surface.
- An AO algorithm is derived which relates the venous saturation S_vO_2 to a microbubble-enhanced NIRS signal, and a similar algorithm is derived for a standard NIRS technique for comparative purposes.
- These algorithms are calibrated and used to predict S_vO_2 in the case where the surrounding tissue oxygenation S_tO_2 is not constant.
- Both algorithms provide accurate estimates (<1% error) when S_tO_2 is constant, however the NIRS approach fails when S_tO_2 varies.
- The MOA algorithm is reasonably accurate for vessels which are less than 20 mm below the surface in situations where the surrounding tissue oxygenation varies between $0.5 < S_tO_2 < 0.9$.

Chapter 8

Conclusions

The problem of detecting venous oxygenation using NIRS has received attention recently [105, 128, 135] due to its clinical importance [104]. In this work the novel use of microbubbles as an optical scattering contrast agent for NIRS has been proposed, as distinct from absorption contrast agents (e.g. indocyanine green [69]) which have been used in the past. Previous work has studied the use of encapsulated microbubbles or gas-filled spheres to enhance a diagnostic US image [123]. In NIRS the acoustic properties and the optical properties of these microbubbles are both significant in providing a measurable microbubble-enhanced change in optical attenuation (MOA), generated using a hybrid acousto-optic technique. This process has been investigated in the context of a clinical measurement of oxygen saturation.

Phase modulation

The preliminary work in this thesis compared two possible approaches to this problem: the first investigated the effect of microbubbles on the ultrasonic modulation of a laser speckle pattern. This approach combines analytical modelling of a bubble in an US field, MC modelling of light transport in an insonified turbid medium and experimental work with a tissue phantom.

The experimental work used an Intralipid-filled tube to form a speckle pattern: the autocorrelation of a single speckle grain was found to contain a small but measurable component which varied at the frequency of the applied US. Adding microbubbles of a broad size distribution to this solution led to an increase in US-modulation. Although this phantom is clearly an unrealistic representation of biological tissue, and the configuration is not equivalent to a clinical situation, this is used as a proof of principle. In order to understand why microbubbles should enhance the phase modulation of photons by US, an analytical model of a bubble under US is used. This is based on the Rayleigh-Plesset equation with the Hoff model describing the shell terms: a linearised form of this is appropriate for low US pressures and small amplitude oscillations, such as is the case in this experiment. The pressure radiated from the surface of an oscillating microbubble is proposed as a mechanism for increasing the US-induced phase shift on photons. This is investigated further using a MC model of light transport in tissue, based on an existing model [132, 133] with the addition of this proposed radiated pressure phase shift. Although the situation in this model is not equivalent to the experimental geometry (a semi-infinite slab rather than a tube), the increase in modulation depth after adding microbubbles is replicated. This effect in the MC model is shown to be sensitive to the applied US frequency, with the largest relative increase close to the theoretically predicted resonant frequency of the microbubbles. In the experimental work the US frequency was fixed, however it is likely that the frequency dependence of the effect will be less significant than is suggested by the MC model. This is because most commercially available microbubbles form suspensions with a range of sizes and hence resonant frequencies. The non-clinical Expancel^{TM} microbubbles used here are expected to have a broad size distribution; medical solutions such as SonoVue^{TM} however often have a smaller range [75], e.g. 0.5-3 μm.

The analytical model for the phase shift induced in a photon as the result

of the pressure radiated from the surface of an oscillating microbubble has not been explicitly validated in this work. However, further experiments with tissue phantoms could be used to determine whether this theoretical model is accurate. The experiment proposed would involve a scattering phantom illuminated by a coherent laser source. A CCD camera could be used to collect the diffuse light signal, which could then be processed to measure the autocorrelation of the speckle pattern. In order to detect modulation due to the microbubble oscillations, rather than due to the other mechanisms of US-modulation, autocorrelation measurements would need to be collected without an US field present. The bubbles however need to be oscillating so that pressure is radiated from their surface, which is key to the proposed AO mechanism. Several methods for producing oscillating bubbles in the absence of US could be used: short-pulsed US can produce bubble responses which are sustained beyond the pulse duration. Bubble oscillations can also be induced in the absence of US by forcing a suspension under presure through a fine mesh.

Intensity modulation

The alternative approach to using microbubbles as an optical contrast agent proposed here involves detecting a change in the DC light level caused by US-modulated microbubble scattering. Rather than the autocorrelation of a single speckle, this technique measures the mean intensity of the speckle pattern, and as such does not require coherent light. This was found to have several advantages over the phase-based approach, particularly that a larger detector with multi-mode coupling can be used. This allows more light to be collected over a given time period and improves on the main difficulty encountered with this technique, which is the ratio of signal to noise. This would also be cheaper to implement clinically, as detectors capable of single photon correlation are not required. Perhaps most importantly in the case of

this work, the experimentally measured MOA can be related directly to the oxygen saturation by making use of a differential version of the BLL derived in this thesis.

The MC models of light transport used in these preliminary studies also highlighted that the computational time required to produce a convergent simulation of a complex system was prohibitively long, such as was the case with a microbubble-filled blood vessel and US-modulation. This is because the high absorption of blood dramatically increases the number of photons required in a MC simulation. Although GPU computing is constantly advancing, and this may not be such an issue in the future, this motivated a new approach to MC modelling which made use of perturbation MC. pMC allows simulations to be made with low optical absorption in place of areas of high absorption such as blood, with the true optical properties recovered through post-processing. This model reduced the computational time to a manageable level when simulating a range of tissue parameters, and was validated against diffusion equation solutions. The results of this model also agree well with the tissue phantom experiments presented in this thesis, which detected MOA changes from a liquid phantom using both Expancel and clinical-grade SonoVue microbubbles. This was performed at pressures which would be safe *in vivo*, and at microbubble concentrations which were measured to be in the range of 10-100% of a clinically achievable level. The magnitude of this MOA signal was dependent on the optical properties of the tissue phantom, up to a background scattering of $\mu_s = 5.5\text{cm}^{-1}$, at which point no significant signal could be detected.

Venous oximetry

The question of whether this technique is sufficient to resolve a signal from a vein *in vivo* remains to be answered. In this thesis an attempt was made

to investigate this problem using the pMC model of a microbubble-filled vein, Sumptuous Bubbles. In the final chapter a theoretical model was developed which showed that an estimate of the oxygen saturation in a blood vessel can be inferred from a dual-wavelength measurement of MOA. The performance of this algorithm was compared with a purely optical NIRS algorithm, which showed that either technique were comparatively sensitive to oxygenation changes in a superficial blood vessel (with a depth of less than 10 mm). In the case of a deeper vessel (15 mm), the AO algorithm was more robust when changes in the surrounding tissue were present compared with the NIRS algorithm, which performed badly. The main limiting factor for the AO algorithm was the signal to noise ratio in the case where the blood vessel was deeper than 20 mm, in which case no significant MOA could be detected over the background noise floor. These observations are consistent with those made in another study comparing AO and optical sensitivity [39]. The performance of the AO algorithm at the depths investigated here suggest that blood vessels such as the pulmonary artery [95] and jugular vein [6] would be possible targets for this technique *in vivo*, being of a similar depth. Certainly in children, where these vessels would be closer to the surface, a significant MOA signal should be measurable. This motivates further clinical work, which could take the form of a measurement modality combining a clinical US monitor with a pulsing function and an optical detector which can be triggered in tandem with the applied US pulse. Microbubble contrast injections are routinely given during echocardiography examinations, and during such a procedure measurements of an MOA signal could be taken from another area of the patient such as superficial veins in the forearms, or the jugular vein.

Further work

In order for this novel technique to be used to measure venous oxygen saturation clinically, several questions remain which warrant further investigation. Firstly, a full experimental phantom study would be required to replicate the results of the theoretical oxygen saturation measurements presented in this thesis. This could be achieved using a blood-filled phantom, with oxygenation controlled by a co-oximeter. Dual-wavelength measurements of MOA using SonoVue microbubbles and modulation achieved using a clinical US system could be used to further test the S_vO_2 algorithm derived here. In addition, geometry of the phantoms used in this work do not closely resemble any physiological architecture. Future phantoms could be constructed with an optical scattering which matches the values expected in tissue surrounding large blood vessels such as the jugular vein in the neck or the pulmonary artery in the chest. The source-detector positions should also be varied and optimised: in particular, reflection mode measurements could be made to more closely match the clinical situation. Of course phantom models comprising of a single blood vessel are still unrealistic. The specificity of the signal should be considered in the case where multiple blood vessels are present, and we would like to measure a signal which is only sensitive to the blood in the US focal region. This will require a phantom with two hollow cores, each of which could be filled with blood and microbubbles, with only one sample of blood insonified.

In summary, this work has presented both a theoretical description of microbubbles as an optical scattering contrast agent for hybrid acousto-optic techniques, and also several experiments using tissue phantoms. A microbubble-enhanced optical signal has been detected from a turbid medium, and a theoretical and MC model has shown that such a signal can be used to infer the optical absorption of the background medium. Hence this technique could be used to enhance the depth sensitivity of NIRS measurements

of oxygen saturation in venous blood. These results suggest that a high concentration of microbubbles are required to detect a significant affect (>10% of the maxium clinically achievable concentration), and the robustness of the technique is highly sensitive to both the optical properties of the surrounding tissue and the depth of the target blood vessel. Therefore significant technical challenges remain before this could be implemented *in vivo*. However further study using a combination of tissue phantoms and preliminary clinical work on superficial blood vessels, such as the jugular vein or pulmonary artery in children, will determine the limits of this novel technique and the potential medical applications for which it could provide a benefit in the future.

Appendices

A.1 Derivation of Phase Shift due to Scatterer Displacement ϕ_d

In this section the phase shift of a photon due to ultrasonic displacement of scatterers is derived, ϕ_d (see equation 2.12). This results from the change in pathlength between successive scatterers when they are perturbed from their equilibrium position. In this derivation some simplifying assumptions are made:

- The time-dependence of a photon's electric field is ignored: we consider only the electric field of a photon arriving at a detector at a fixed time, so without loss of generality we can choose $t = 0$.
- The weak scattering approximation is used [107,108], i.e. $k_a l \gg 1$ where l is the photon mean free path and $k_a A_a \ll 1$ where A_a is the US amplitude. Therefore scattering events can be treated as independent. This is valid for optical scattering in biological tissue at the US frequencies and amplitudes commonly used in biomedical imaging.
- US-modulation of the refractive index is ignored (see Section 2.2.1),

so that the phase shift of a photon due to scatterer displacement is independent of the phase shift due to refractive index modulation.

The magnitude of the electric field of a photon at a point $\vec{r}$ is $E(\vec{r}) = E_0 \exp(i\vec{k}\cdot\vec{r})$, where $\vec{k} = n_0 k_0 \hat{k}$, k_0 is the optical wavenumber in air, and n_0 is the refractive index of the tissue at point $\vec{r}$. The phase of a photon ϕ is defined as the argument of the complex electric field, i.e. $E(\vec{r}) = E_0 \exp(i\phi)$. In the case where scatterers are moving under applied US, the vector connecting the j^{th} scatterer to the $(j+1)^{th}$ scatterer $(\vec{r}_{j+1} - \vec{r}_j)$ is modified due to the displacement of each scatterer $\Delta\vec{r}_j(\vec{r}_j, t)$. Figure A.1 shows the geometry of this situation.

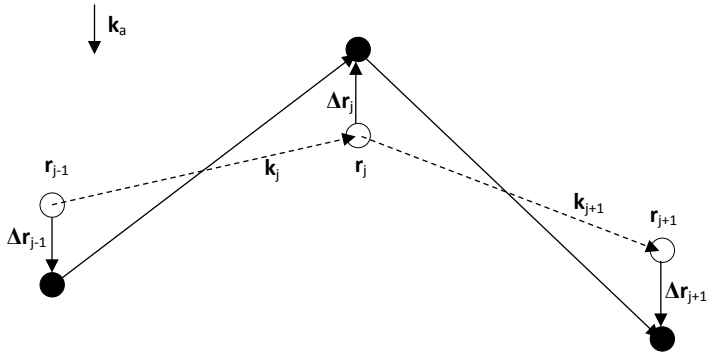

Figure A.1: The displacement of scatterers as a result of applied US changes the path a photon takes between successive scatterers.

Following the path shown in figure A.1, the electric field at position $\vec{r}\,'_j = \vec{r}_j + \Delta\vec{r}_j$ is:

$$E(\vec{r}\,'_j) = E(\vec{r}\,'_{j-1}) \exp\left[i\vec{k}_j \cdot (\vec{r}_j + \Delta\vec{r}_j - \vec{r}_{j-1} - \Delta\vec{r}_{j-1})\right] \tag{A.1}$$

Now if we assume that the initial position of the photon is $\vec{r}_0 = 0$, and that this position is unperturbed by US, the first few terms of equation A.1 become:

$$E(\vec{r}\,'_2) = \exp\left[i\vec{k}_1 \cdot (\vec{r}_1 + \Delta\vec{r}_1)\right] \exp\left[i\vec{k}_2 \cdot (\vec{r}_2 + \Delta\vec{r}_2 - \vec{r}_1 - \Delta\vec{r}_1)\right] \quad \text{(A.2)}$$

$$= \exp\left[i(\vec{r}_1 + \Delta\vec{r}_1) \cdot (\vec{k}_1 - \vec{k}_2) + i(\vec{r}_2 + \Delta\vec{r}_2) \cdot \vec{k}_2\right] \quad \text{(A.3)}$$

$$= \exp\left[i(\vec{r}_2 + \Delta\vec{r}_2) \cdot \vec{k}_2 - i(\vec{r}_1 + \Delta\vec{r}_1) \cdot \vec{q}_1\right] \quad \text{(A.4)}$$

where $\vec{q}_j = \vec{k}_{j+1} - \vec{k}_j$. We can generalise this to find the magnitude of the electric field of the photon after N scattering events:

$$E(\vec{r}_N) = \exp\left[i(\vec{r}_N + \Delta\vec{r}_N) \cdot \vec{k}_N - i\sum_{j=1}^{N-1}(\vec{r}_j + \Delta\vec{r}_j) \cdot \vec{q}_j\right] \quad \text{(A.5)}$$

$$= \exp\left[i\vec{r}_N \cdot \vec{k}_N - i\sum_{j=1}^{N-1}\vec{r}_j \cdot \vec{q}_j - i\phi_d\right] \quad \text{(A.6)}$$

where ϕ_d is the extra phase as a result of the displacement of scatterers. If the point of interest is the photon's final position at a detector, then we can also assume that $\Delta\vec{r}_N = 0$. So the contribution from each individual scattering event to this phase shift is [133, 134]:

$$\phi_{dj} = -\vec{q}_j.\Delta\vec{r}_j \quad \text{(A.7)}$$

$$= -(\vec{k}_{j+1} - \vec{k}_j) \cdot \vec{A}_a(\vec{r}_j, t) \quad \text{(A.8)}$$

A.2 Linearisation of Rayleigh-Plesset Equation

In this section it will be shown that the Rayleigh-Plesset equation (with shell terms based on the Hoff model) can be linearised, so that it takes the form

of a driven simple harmonic oscillator. This assumes that the amplitude of bubble oscillations is small, i.e. $R(t) = R_0[1 + z(t)]$ where $z(t) \ll 1$. Substituting this into equation 2.16:

$$\rho_L R_0^2 \left[(1+z)\ddot{z} + \frac{3}{2}\dot{z}^2\right] + P_0 - P_a(t) - P_G(z) + \frac{4\dot{z}}{1+z}\eta_L = f_{ce} + f_{cd} \quad \text{(A.9)}$$

and similarly for the pressure inside the bubble (equation 2.17) and the shell terms (equations 2.21 and 2.22):

$$P_G(z) = \left[P_0 + \frac{2\sigma_0}{R_0}\right](1+z)^{-3} \quad \text{(A.10)}$$

$$f_{ce} = -12G_s d_s R_0^{-1}\left[1 - (1+z)^{-1}\right](1+z)^{-3} - \frac{2\sigma_0}{R_0} \quad \text{(A.11)}$$

$$f_{cd} = -12\eta_s d_s R_0^{-1}\dot{z}(1+z)^{-4} \quad \text{(A.12)}$$

Combining the above equations and discarding terms of order z^2 and above gives:

$$\begin{aligned} &\rho_L R_0^2\ddot{z} + P_0 - P_a(t) - \left[P_0 + \frac{2\sigma_0}{R_0}\right](1-3z) + 4\dot{z}\eta_L \\ &= -12G_s d_s R_0^{-1} z - 12\eta_s d_s R_0^{-1}\dot{z} + O(z^2) \end{aligned} \quad \text{(A.13)}$$

This can be written in the standard form of a harmonic oscillator:

$$a\ddot{z} + b\dot{z} + cz = P_a(t) \quad \text{(A.14)}$$

where the coefficients a, b and c depend only on the physical properties of the bubble and surrounding fluid:

$$a = \rho_L R_0^2 \tag{A.15}$$

$$b = 4\eta_L + 12\frac{d_s\eta_s}{R_0} \tag{A.16}$$

$$c = 3P_0 + \frac{6\sigma_0}{R_0} + 12\frac{G_s d_s}{R_0} \tag{A.17}$$

The solution to equation A.14 is therefore that of a harmonic oscillator. If the driving pressure $P_a(t) = P_a \cos(\vec{k_a} \cdot \vec{r} - \omega_a t)$ then:

$$z(t) = \frac{P_a}{\beta}\cos(\vec{k_a} \cdot \vec{r} - \omega_a t + \xi) \tag{A.18}$$

where β (the response of the system) is a function of US frequency, and ξ is a phase shift:

$$\beta = \sqrt{\omega_a^2 b^2 + (c - a\omega_a^2)^2} \tag{A.19}$$

$$\xi = \arctan\left(\frac{\omega_a b}{a\omega_a^2 - c}\right) \tag{A.20}$$

A.3 Second Order Solution of Rayleigh-Plesset Equation

To extend the linear solution of the Rayleigh-Plesset equation to second order, we use the same expansion for the bubble radius $R(t) = R_0[1 + z(t)]$. In this case we retain terms of order z and order z^2, so that the equation of motion becomes:

$$a\ddot{z} + b\dot{z} + cz = P_a(t) + dz^2 + ez\dot{z} - az\ddot{z} - \frac{3}{2}a\dot{z}^2 \tag{A.21}$$

which is equivalent to a harmonic oscillator with some extra quadratic terms. The coefficients a, b and c are as defined in the linear model (Section A.2). The coefficients of the non-linear terms d and e are:

$$d = \frac{48G_s d_s}{R_0} + \frac{10\sigma_0}{R_0} + 6P_0 \tag{A.22}$$

$$e = \frac{48\eta_s d_s}{R_0} + 4\mu_L \tag{A.23}$$

In this section the applied US pressure $P_a(t)$ will be expressed in complex exponential form:

$$P_a(t) = P_a \cos(-\omega_a t) = \frac{P_a}{2}\left[e^{i\omega_a t} + e^{-i\omega_a t}\right] \tag{A.24}$$

where we have assumed for convenience that the bubble in question is at a location $\vec{r} = 0$. To express the trial solution for equation A.21 we now adopt a vector form, which will simplify many of the expressions that follow:

$$\begin{aligned} & R(t) \\ & = R_0\left[1 + X_0 + X_1 e^{i\omega_a t} + X_1^* e^{-i\omega_a t} + X_2 e^{2i\omega_a t} + X_2^* e^{-2i\omega_a t}\right] \\ & = R_0 \begin{pmatrix} 1 + X_0 \\ X_1 \\ X_1^* \\ X_2 \\ X_2^* \end{pmatrix} \cdot \begin{pmatrix} 1 \\ e^{i\omega_a t} \\ e^{-i\omega_a t} \\ e^{2i\omega_a t} \\ e^{-2i\omega_a t} \end{pmatrix} \end{aligned} \tag{A.25}$$

X_0 is the shift in equilibrium size compared with a non-oscillating bubble, X_1 is the complex linear response of the bubble and X_2 is the complex second order response. These response function are expected to depend on

the parameters of the system and on the US frequency ω_a. In order to find expressions for X_0, X_1 and X_2 this trial solution is substituted into the equation of motion A.21. Following the weakly non-linear analysis of Church [13] we assume that $1 > |X_1| > |X_2| \approx X_0$ (i.e. that the 1st order term is dominant): therefore only terms of order X_0, X_1, X_1^2 and X_2 are retained, and any higher order or cross terms are assumed to be negligible. This leaves:

$$
\begin{aligned}
&\left[a \begin{pmatrix} 0 \\ -\omega^2 X_1 \\ -\omega^2 X_1^* \\ -4\omega^2 X_2 \\ -4\omega^2 X_2^* \end{pmatrix} + b \begin{pmatrix} 0 \\ i\omega X_1 \\ -i\omega X_1^* \\ 2i\omega X_2 \\ -2i\omega X_2^* \end{pmatrix} + c \begin{pmatrix} X_0 \\ X_1 \\ X_1^* \\ X_2 \\ X_2^* \end{pmatrix} \right] \cdot \underline{Z} - \\
&\left[d \begin{pmatrix} X_0^2 + 2X_1 X_1^* \\ 0 \\ 0 \\ X_1^2 \\ X_1^{*2} \end{pmatrix} + e \begin{pmatrix} 0 \\ 0 \\ 0 \\ i\omega X_1^2 \\ -i\omega X_1^{*2} \end{pmatrix} - \frac{3}{2} a \begin{pmatrix} 2\omega^2 X_1 X_1^* \\ 0 \\ 0 \\ -\omega^2 X_1^2 \\ -\omega^2 X_1^{*2} \end{pmatrix} \right] \cdot \underline{Z} - \\
&\left[a \begin{pmatrix} -2\omega^2 X_1 X_1^* \\ 0 \\ 0 \\ -\omega^2 X_1^2 \\ -\omega^2 X_1^{*2} \end{pmatrix} \right] \cdot \underline{Z} \\
&= \frac{P_a}{2} \begin{pmatrix} 0 \\ 1 \\ 1 \\ 0 \\ 0 \end{pmatrix} \cdot \underline{Z}
\end{aligned}
\tag{A.26}
$$

where $\underline{Z} = \begin{bmatrix} 1 \\ e^{i\omega_a t} \\ e^{-i\omega_a t} \\ e^{2i\omega_a t} \\ e^{-2i\omega_a t} \end{bmatrix}$.

Here the subscript a has been omitted from ω_a for brevity. Comparing coefficients of equation A.26 provides five simultaneous equations in terms of X_0, X_1 and X_2: in fact, only three of these are independent (the 3rd row is the complex conjugate of the 2nd row, and the 5th row is the conjugate of the 4th row). The 2nd row can be rearranged to give an expression for X_1:

$$X_1 = \frac{P_a}{2}\left(c - a\omega^2 + ib\omega\right)^{-1} \tag{A.27}$$

The first row provides an expression for X_0 in terms of X_1:

$$X_0 = |X_1|^2 \frac{2d - a\omega^2}{c} \tag{A.28}$$

Similarly the 3rd row gives the following expression for X_2:

$$X_2 = X_1^2 \frac{\frac{5}{2}a\omega^2 + d + ie\omega}{c - 4a\omega^2 + 2ib\omega} \tag{A.29}$$

This shows that X_1 and X_2 in general have real and imaginary parts, with a magnitude corresponding to the amplitude of the bubble response and phase relative to the applied US.

A.4 Derivation of $\Delta\phi_n$, $\Delta\phi_d$ and $\Delta\phi_r$

In this section the phase difference between two photons seperated by a time lag of τ will be derived. This phase shift arises from the two mechanisms of US-modulation of light explored in this work (refractive index changes and scatterer displacement) and the proposed mechanism for microbubble enhancement of the phase shift (due to radiated pressure from a bubble surface). Considering the j_{th} photon free path in the medium, these three mechanisms induce the following phase shifts on a photon:

$$\begin{aligned}
\phi_{n,j}(t,\tau) =& 2n_0k_0A_a\eta\sin(k_al_j\cos\theta_j/2) \\
& \sin(\vec{k}_a\cdot\vec{r}_{j-1}+k_al_j\cos\theta_j/2-\omega_at)/\cos(\theta_j) \\
\phi_{d,j}(t,\tau) =& -n_0k_0A_a\left[(\hat{k_{j+1}}-\hat{k_j})\cdot\hat{k_a}\right] \\
& \sin(\vec{k}_a\cdot\vec{r}_j-\omega_at) \\
\phi_{r,j}(t,\tau) =& \frac{n_0k_0\eta k_a^2R_0^3P_a}{\beta}\left[\ln(\frac{R_0}{l_j})+\ln(\frac{R_0}{l_{j+1}})\right] \\
& sin(\vec{k}_a\cdot\vec{r}_j-\omega_at+\xi)
\end{aligned} \tag{A.30}$$

Here the applied US pressure is taken as $P_a(t) = P_a\sin(\vec{k}_a\cdot\vec{r}_j-\omega_at)$. The phase difference between two photons seperated by a time τ is given by $\phi_j(t+\tau)-\phi_j(t)$. In order to simplify these expressions in the above 3 cases, it will be necessary to use the following result:

$$\begin{aligned}
\sin(X-\epsilon)-\sin X &= \sin X\cos\epsilon-\cos X\sin\epsilon-\sin X \\
&= \sin X(\cos\epsilon-1)-\cos X\sin\epsilon \\
&= \sin X(\cos^2(\epsilon/2)-\sin^2(\epsilon/2)-1)-2\cos X\sin(\epsilon/2)\cos(\epsilon/2)) \\
&= \sin X(-2\sin^2(\epsilon/2)-2\cos X\sin(\epsilon/2)\cos(\epsilon/2)) \\
&= -2\sin(\epsilon/2)\cos(X-\epsilon/2)
\end{aligned}$$

(A.31)

Using this general result the phase difference between two photons can be simplified into a single expression, which is advantageous for large scale simulations such as the Monte Carlo model presented in Section 4.1:

$$
\begin{aligned}
\Delta\phi_{n,j}(t,\tau) &= 4n_0k_0A_a\eta\sin(-\omega_a\tau/2)\sin(k_al_j\cos\theta_j/2) \\
&\quad \cos(\vec{k}_a\cdot\vec{r}_{j-1}+k_al_j\cos\theta_j/2-\omega_at-\omega_a\tau/2)/\cos(\theta_j) \\
\Delta\phi_{d,j}(t,\tau) &= 2n_0k_0A_a\sin(\omega_a\tau/2)\left[(\hat{k_{j+1}}-\hat{k_j}).\hat{k_a}\right] \\
&\quad \cos(\vec{k}_a\cdot\vec{r}_j-\omega_at-\omega_a\tau/2) \\
\Delta\phi_{r,j}(t,\tau) &= \frac{2n_0k_0\eta k_a^2R_0^3P_a}{\beta}\left[\ln(\frac{R_0}{l_j})+\ln(\frac{R_0}{l_{j+1}})\right] \\
&\quad cos(\vec{k}_a\cdot\vec{r}_j-\omega_at-\omega_a\tau/2+\xi)\sin(-\omega_a\tau/2)
\end{aligned}
\tag{A.32}
$$

A.5 Limit on the Bubble Concentration ρ_b

The optical model assumes that particles are sufficiently far apart so that scattering events are independent of one another. The conditions under which this holds can be stated in terms of a limit on the fraction of the tissue volume occupied by the scatterers [84] (no greater than 1%), or expressed as a limit on the average seperation between neighbouring bubbles [87] (greater than $3R_0$). The acoustic modelling also assumes that the average bubble seperation is more than several bubble diameters, so that secondary bubble radiation effects can be ignored. In this section the limit imposed by these conditions on the bubble concentration ρ_b are calculated.

The volume fraction V_{frac} is defined as the total volume occupied by scattering particles divided by the volume of the solution. In the case of bubbles (assumed to be spherical) this is given by:

$$V_{frac} = \rho_b \frac{4}{3}\pi R^3 \tag{A.33}$$

where R is the radius of a bubble and ρ_b has units m^{-3}. Taking the limit of V_f to be 0.01 for light scattering to be independent [84], this suggest ρ_b should be no larger than $2\text{x}10^9\text{mm}^{-3}$ for a bubble of radius $R = 2.25\mu\text{m}$.

For the acoustic model to be valid, the average bubble separation must be greater than several bubble diameters [101]. To calculate the limit imposed on ρ_b by this condition, assume that the population of bubbles are arranged on a cubic lattice (see figure A.2). If the seperation between neighbouring bubbles is d, the volume occupied by each bubble V_b is then $V_b \approx d^3 = 1/\rho_b$. If the limit on bubble seperation is taken to be $d > 8R_0$ [87], the maximum bubble concentration is:

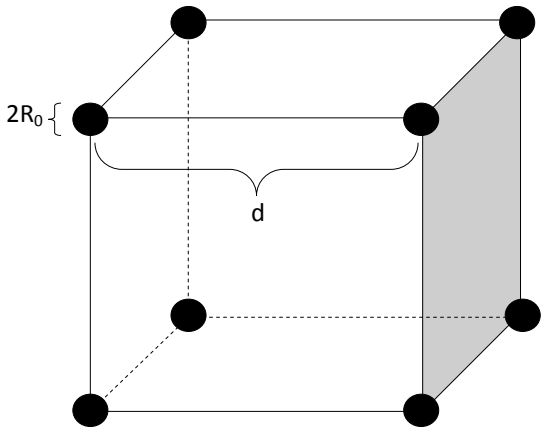

Figure A.2: Microbubbles are assumed to be arranged on a cubic lattice, with seperation d.

$$\rho_b < \left(\frac{1}{8R_0}\right)^3 \tag{A.34}$$

For a bubble of radius $R = 2.25\mu$m this limit is $\rho_b < 1.7\text{x}10^5\text{mm}^{-3}$.

References

[1] E. Alerstam, T. Svensson, and S. Andersson-Engels. Parallel computing with graphics processing units for high-speed monte carlo simulation of photon migration. *Journal of biomedical optics*, 13:060504, 2008.

[2] E. Alerstam, T. Svensson, and S. Andersson-Engels. Cudamcml - user manual and implementation notes. *Lund University, Lund*, 2009.

[3] J. Alter, C. A. Sennoga, D. M. Lopes, R. J. Eckersley, and D. J. Wells. Microbubble stability is a major determinant of the efficiency of ultrasound and microbubble mediated in vivo gene transfer. *Ultrasound in Medicine & Biology*, 35(6):976–984, 2009.

[4] O. W. Van Assendelft and W. G. Zijlstra. Extinction coefficients for use in equations for the spectrophotometric analysis of haemoglobin mixtures. *Analytical Biochemistry*, 69(1):43–48, 1975.

[5] M. Atlan, B. C. Forget, F. Ramaz, A. C. Boccara, and M. Gross. Pulsed acousto-optic imaging in dynamic scattering media with heterodyne parallel speckle detection. *Optics letters*, 30(11):1360–1362, 2005.

[6] M. Bazaral and S. Harlan. Ultrasonographic anatomy of the internal jugular vein relevant to percutaneous cannulation. *Critical Care Medicine*, 9(4):307, 1981.

[7] A. T. Bhutta, J. W. Ford, J. G. Parker, P. Prodhan, E. E. Fontenot, P. M. Seib, B. I. Stroope, E. A. Frazier, M. L. Schmitz, J. J.

Drummond-Webb, et al. Noninvasive cerebral oximeter as a surrogate for mixed venous saturation in children. *Pediatric cardiology*, 28:34–41, 2007.

[8] K. Bjerknes, P. C. Sontum, G. Smistad, and I. Agerkvist. Preparation of polymeric microbubbles: formulation studies and product characterisation. *International Journal of Pharmaceutics*, 158(2):129–136, 1997.

[9] F. J Blonigen, A. Nieva, C. A DiMarzio, S. Manneville, L. Sui, G. Maguluri, T. W Murray, and R. A Roy. Computations of the acoustically induced phase shifts of optical paths in acoustophotonic imaging with photorefractive-based detection. *Applied optics*, 44(18):3735–3746, 2005.

[10] C. F Bohren and D. R Huffman. Absorption and scattering of light by small particles. 1983.

[11] M. Born and E. Wolf. *Principles of Optics, 7th edn.* Cambridge, 1999.

[12] G. E. P. Box and M. E. Muller. A note on the generation of random normal deviates. *The Annals of Mathematical Statistics*, 29:610–611, 1958.

[13] C. C Church. The effects of an elastic solid surface layer on the radial pulsations of gas bubbles. *The Journal of the Acoustical Society of America*, 97:1510, 1995.

[14] L. Cohen. *Time-frequency analysis.* Prentice-Hall, 1995.

[15] M. Cope. *The development of a near infrared spectroscopy system and its application for non invasive monitoring of cerebral blood and tissue oxygenation in the newborn infants.* PhD thesis, University College London, 1991.

[16] P. A Dayton, K. E. Morgan, A. L. Klibanov, G. H. Brandenburger, and K. W. Ferrara. Optical and acoustical observations of the effects of ultrasound on contrast agents. *Ultrasonics, Ferroelectrics and Frequency Control, IEEE Transactions on*, 46(1):220–232, 2002.

[17] H. C. Van de Hulst. *Light scattering by small particles*. Dover, New York, 1981.

[18] C. E Dean and P. L Marston. Critical angle light scattering from bubbles: an asymptotic series approximation. *Applied Optics*, 30(33):4764–4776, 1991.

[19] D. T. Delpy, M. Cope, P. Zee, S. Arridge, S. Wray, and J. Wyatt. Estimation of optical pathlength through tissue from direct time of flight measurement. *Physics in Medicine and Biology*, 33:1433, 1988.

[20] J. J. Duderstadt and W. R. Martin. *Transport theory. A Wiley-Interscience Publication*. John Wiley & Sons, 1979.

[21] T. Durduran, R. Choe, J. P. Culver, L. Zubkov, M. J. Holboke, J. Giammarco, B. Chance, and A. G. Yodh. Bulk optical properties of healthy female breast tissue. *Physics in medicine and biology*, 47:2847, 2002.

[22] R. J. Eckersley, M. X. Tang, K. Chetty, and J. V. Hajnal. Microbubble contrast agent detection using binary coded pulses. *Ultrasound in medicine & biology*, 33(11):1787–1795, 2007.

[23] J. M Elazar, O. Steshenko, Y. Deng, S. Zeng, Q. Luo, Z. Zhang, L. Fu, S. Moon, D. Kim, and E. Sim. Doppler effect's contribution to ultrasonic modulation of multiply scattered coherent light: Monte carlo modeling. *Optics Letters*, 33(2):131–133, 2008.

[24] D. S. Elson, R. Li, C. Dunsby, R. Eckersley, and M.-X. Tang. Ultrasound-mediated optical tomography: a review of current methods. *Interface Focus*, 1(4):632–648, 2011.

[25] C. E. Elwell, M. Cope, A. D. Edwards, J. S. Wyatt, D. T. Delpy, and E. O. Reynolds. Quantification of adult cerebral hemodynamics by near-infrared spectroscopy. *Journal of Applied Physiology*, 77:2753–2760, 1994.

[26] P. S. Epstein and M. S. Plesset. On the stability of gas bubbles in liquid-gas solutions. *The Journal of Chemical Physics*, 18:1505, 1950.

[27] U. Farook, E. Stride, and M. J. Edirisinghe. Preparation of suspensions of phospholipid-coated microbubbles by coaxial electrohydrodynamic atomization. *Journal of The Royal Society Interface*, 6(32):271–277, 2009.

[28] S. B Feinstein, F. J Ten Cate, W. Zwehl, K. Ong, G. Maurer, C. Tei, P. M Shah, S. Meerbaum, and E. Corday. Two-dimensional contrast echocardiography. i. in vitro development and quantitative analysis of echo contrast agents. *Journal of the American College of Cardiology*, 3(1):14, 1984.

[29] J. A. Feshitan, C. C. Chen, J. J. Kwan, and M. A. Borden. Microbubble size isolation by differential centrifugation. *Journal of colloid and interface science*, 329(2):316–324, 2009.

[30] C. Feuillade. Acoustically coupled gas bubbles in fluids: Time-domain phenomena. *The Journal of the Acoustical Society of America*, 109:2606, 2001.

[31] M. Firbank, E. Okada, and D. T Delpy. Investigation of the effect of discrete absorbers upon the measurement of blood volume with near-infrared spectroscopy. *Physics in Medicine and Biology*, 42:465, 1997.

[32] A. P. Gibson, J. C. Hebden, and S. R. Arridge. Recent advances in diffuse optical imaging. *Physics in Medicine and Biology*, 50:R1, 2005.

[33] W. J Glantschnig and S. H Chen. Light scattering from water droplets in the geometrical optics approximation. *Applied Optics*, 20(14):2499–2509, 1981.

[34] B. B Goldberg, J. B Liu, and F. Forsberg. Ultrasound contrast agents: a review. *Ultrasound in medicine & biology*, 20(4):319–333, 1994.

[35] J. Gorce, M. Arditi, and M. Schneider. Influence of bubble size distribution on the echogenicity of ultrasound contrast agents: A study of sonovue (tm). *Investigative radiology*, 35(11):661, 2000.

[36] R. Graaff, M. H. Koelink, F. F. M. De Mul, W. G. Zijistra, A. C. M. Dassel, and J. G. Aarnoudse. Condensed monte carlo simulations for the description of light transport. *Applied optics*, 32(4):426–434, 1993.

[37] E. Granot, A. Lev, Z. Kotler, B. G. Sfez, and H. Taitelbaum. Detection of inhomogeneities with ultrasound tagging of light. *Journal of the Optical Society of America A*, 18(8):1962–1967, 2001.

[38] J. Guan and T. J Matula. Using light scattering to measure the response of individual ultrasound contrast microbubbles subjected to pulsed ultrasound in vitro. *The Journal of the Acoustical Society of America*, 116:2832, 2004.

[39] S. Gunadi and T. S. Leung. Spatial sensitivity of acousto-optic and optical near-infrared spectroscopy sensing measurements. *Journal of Biomedical Optics*, 16(12):127005, 2011.

[40] D. J Hall, M. J Hsu, S. Esener, and R. F Mattrey. Detection of ultrasound-modulated photons and enhancement with ultrasound microbubbles. In *Proc. of SPIE*, volume 7177, pages 71771L–1.

[41] C. K. Hayakawa, J. Spanier, F. Bevilacqua, A. K. Dunn, J. S. You, B. J. Tromberg, and V. Venugopalan. Perturbation monte carlo methods to solve inverse photon migration problems in heterogeneous tissues. *Optics Letters*, 26(17):1335–1337, 2001.

[42] L. G. Henyey and J. L. Greenstein. Diffuse radiation in the galaxy. *AstroPhys J*, 93:70–83, 1941.

[43] C. Herring. Theory of the pulsations of the gas bubble produced by an underwater explosion (columbia university, new london, connecticut, 1941). Technical report, NDRC Report No. C4, 1941.

[44] M. Hiraoka, M. Firbank, M. Essenpreis, M. Cope, S. R. Arridge, P. Zee, and D. T. Delpy. A monte carlo investigation of optical pathlength in inhomogeneous tissue and its application to near-infrared spectroscopy. *Physics in Medicine and Biology*, 38:1859, 1993.

[45] L. Hoff, P. C Sontum, and J. M Hovem. Oscillations of polymeric microbubbles: Effect of the encapsulating shell. *The Journal of the Acoustical Society of America*, 107:2272, 2000.

[46] J. Honeysett, E. Stride, and T. Leung. Monte carlo simulations of acousto-optics with microbubbles. In *Proceedings of SPIE*, volume 7564, page 75640K, 2010.

[47] J. E. Honeysett, E. Stride, and T. S. Leung. Microbubble enhancement of ultrasound-modulated optical sensing with incoherent light. In *Proceedings of SPIE*, volume 7899, page 789919, 2011.

[48] J. E. Honeysett, E. Stride, and T. S. Leung. Feasibility study of non-invasive oxygenation measurement in a deep blood vessel using acousto-optics and microbubbles. *Oxygen Transport to Tissue XXXIII*, pages 277–283, 2012.

[49] J. E. P. Honeysett, E. Stride, J. Deng, and T. S. Leung. An algorithm for sensing venous oxygenation using ultrasound-modulated light enhanced by microbubbles. In *Proceedings of SPIE*, volume 8223, page 82232Z, 2012.

[50] B. L. Horecker. The absorption spectra of hemoglobin and its derivatives in the visible and near infra-red regions. *Journal of Biological Chemistry*, 148(1):173, 1943.

[51] A. Ishimaru. *Wave Propagation and Scattering in Random Media*. Academic Press, New York, 1978.

[52] S. L. Jacques and L. Wang. Monte carlo modeling of light transport in tissues. *Optical-thermal response of laser-irradiated tissue*, pages 73–100, 1995.

[53] F. F Jobsis. Noninvasive, infrared monitoring of cerebral and myocardial oxygen sufficiency and circulatory parameters. *Science*, 198(4323):1264, 1977.

[54] N. De Jong, R. Cornet, and C. T. Lancee. Higher harmonics of vibrating gas-filled microspheres. part one: simulations. *Ultrasonics*, 32(6):447–453, 1994.

[55] N. De Jong, R. Cornet, and C. T. Lancee. Higher harmonics of vibrating gas-filled microspheres. part two: measurements. *Ultrasonics*, 32(6):455–459, 1994.

[56] N. De Jong, L. Hoff, T. Skotland, and N. Bom. Absorption and scatter of encapsulated gas filled microspheres: theoretical considerations and some measurements. *Ultrasonics*, 30(2):95–103, 1992.

[57] V. Kamath and A. Prosperetti. Numerical integration methods in gas-bubble dynamics. *The Journal of the Acoustical Society of America*, 85:1538, 1989.

[58] M. Keijzer, J. W. Pickering, and M. J. C. van Gemert. Laser beam diameter for port wine stain treatment. *Lasers in surgery and medicine*, 11(6):601–605, 1991.

[59] J. B Keller and M. Miksis. Bubble oscillations of large amplitude. *J. Acoust. Soc. Am*, 68(2):628–633, 1980.

[60] A. Kienle and M. S. Patterson. Determination of the optical properties of turbid media from a single monte carlo simulation. *Physics in Medicine and Biology*, 41:2221, 1996.

[61] M. Kobayashi, T. Mizumoto, Y. Shibuya, M. Enomoto, and M. Takeda. Fluorescence tomography in turbid media based on acousto-optic modulation imaging. *Applied Physics Letters*, 89(18):181102–181102, 2006.

[62] S. R Kothapalli, S. Sakadzic, C. Kim, and L. V Wang. Imaging optically scattering objects with ultrasound-modulated optical tomography. *Optics letters*, 32(16):2351–2353, 2007.

[63] K. B. Krishnan, P. Fomitchov, S. J. Lomnes, M. Kollegal, and F. P. Jansen. A theory for the ultrasonic modulation of incoherent light in turbid medium. *Proceedings of SPIE*, 6009(1):60090V–60090V, 2005.

[64] P. Lai, R. A. Roy, and T. W. Murray. Quantitative characterization of turbid media using pressure contrast acousto-optic imaging. *Optics Letters*, 34(18):2850–2852, 2009.

[65] T. G. Leighton. *The acoustic bubble*. Academic Pr, 1997.

[66] I. Lentacker, B. G. De Geest, R. E. Vandenbroucke, L. Peeters, J. Demeester, S. C. De Smedt, and N. N. Sanders. Ultrasound-responsive polymer-coated microbubbles that bind and protect dna. *Langmuir*, 22(17):7273–7278, 2006.

[67] T. S. Leung, J. E. Honeysett, E. Stride, and J. Deng. Light propagation in a turbid medium with insonified microbubbles. *Journal of Biomedical Optics*, 18(1):1500215002, 2013.

[68] T. S. Leung and S. Powell. Fast monte carlo simulations of ultrasound-modulated light using a graphics processing unit. *Journal of Biomedical Optics*, 15(5):055007, 2010.

[69] T. S Leung, I. Tachtsidis, M. Tisdall, M. Smith, D. T Delpy, and C. E Elwell. Theoretical investigation of measuring cerebral blood flow in the adult human head using bolus indocyanine green injection and near-infrared spectroscopy. *Applied optics*, 46(10):1604–1614, 2007.

[70] W. Leutz and G. Maret. Ultrasonic modulation of multiply scattered light. *Physica B: Condensed Matter*, 204(1-4):14–19, 1995.

[71] S. Leveque, A. C. Boccara, et al. Ultrasonic tagging of photon paths in scattering media: parallel speckle modulation processing. *Optics letters*, 24(3):181–183, 1999.

[72] H. L. Li, X. Z. Zheng, H. P. Wang, F. Li, Y. Wu, and L. F. Du. Ultrasound-targeted microbubble destruction enhances (aav-mediated) gene transfection in human (rpe) cells in vitro and rat retina in vivo. *Gene therapy*, 16(9):1146–1153, 2009.

[73] Y. Li, H. Zhang, C. Kim, K. H. Wagner, P. Hemmer, and L. V. Wang. Pulsed ultrasound-modulated optical tomography using spectral-hole burning as a narrowband spectral filter. *Applied Physics Letters*, 93(1), 2008.

[74] P. L. Lin, R. J. Eckersley, and E. A. H. Hall. Ultrabubble: a laminated ultrasound contrast agent with narrow size range. *Advanced Materials*, 21(38-39):3949–3952, 2009.

[75] J. R Lindner. Microbubbles in medical imaging: current applications and future directions. *Nature Reviews Drug Discovery*, 3(6):527–533, 2004.

[76] H. Liu, B. Chance, A. H. Hielscher, S. L. Jacques, F. K. Tittel, et al. Influence of blood vessels on the measurement of hemoglobin oxygenation as determined by time-resolved reflectance spectroscopy. *Medical Physics*, 22(8):1209–1218, 1995.

[77] P. Liu. A new phase function approximating to mie scattering for radiative transport equations. *Physics in Medicine and Biology*, 39:1025, 1994.

[78] Q. Liu, S. Norton, and T. Vo-Dinh. Modeling of nonphase mechanisms in ultrasonic modulation of light propagation. *Applied optics*, 47(20):3619–3630, 2008.

[79] G. W. Lucassen, W. Verkruysse, M. Keijzer, and M. J. C. van Gemert. Light distributions in a port wine stain model containing multiple cylindrical and curved blood vessels. *Lasers in surgery and medicine*, 18(4):345–357, 1996.

[80] C. Maetzler. Matlab functions for mie scattering and absorption. *IAP Res. Rep*, 2002.

[81] G. D. Mahan, W. E. Engler, J. J. Tiemann, and E. Uzgiris. Ultrasonic tagging of light: theory. *Proceedings of the National Academy of Sciences of the United States of America*, 95(24):14015, 1998.

[82] G. Maret and P. E. Wolf. Multiple light scattering from disordered media. the effect of brownian motion of scatterers. *Zeitschrift Physik B Condensed Matter*, 65(4):409–413, 1987.

[83] F. A Marks, H. W Tomlinson, and G. W Brooksby. Comprehensive approach to breast cancer detection using light: photon localization by

ultrasound modulation and tissue characterization by spectral discrimination. 500, 1888.

[84] F. Martelli, S. Del Bianco, A. Ismaelli, and G. Zaccanti. *Light Propagation Through Biological Tissue and Other Diffusive Media: Theory, Solutions, and Software*. SPIE Press, 2010.

[85] D. L. Miller. Ultrasonic detection of resonant cavitation bubbles in a flow tube by their second-harmonic emissions. *Ultrasonics*, 19(5):217–224, 1981.

[86] M. Minnaert. On musical air-bubbles and the sounds of running water. *Philosophical Magazine Series 7*, 16(104):235–248, 1933.

[87] M. I Mishchenko, L. D Travis, and A. A Lacis. *Scattering, absorption, and emission of light by small particles*. Cambridge Univ Pr, 2002.

[88] C. M. Moran, J. A. Ross, C. Cunningham, M. Butler, T. Anderson, D. Newby, K. A. A. Fox, and W. N. McDicken. Manufacture and acoustical characterisation of a high-frequency contrast agent for targeting applications. *Ultrasound in Medicine & Biology*, 32(3):421–428, 2006.

[89] H. Mulvana, E. Stride, J. V. Hajnal, and R. J. Eckersley. Temperature dependent behavior of ultrasound contrast agents. *Ultrasound in Medicine & Biology*, 36(6):925–934, 2010.

[90] T. W. Murray and R. A. Roy. Illuminating sound: Imaging tissue optical properties with ultrasound. *Acoustics Today*, 3(3), 2007.

[91] N. Nagdyman, P. Ewert, B. PETERS, O. Miera, T. Fleck, and F. Berger. Comparison of different near-infrared spectroscopic cerebral oxygenation indices with central venous and jugular venous oxygenation saturation in children. *Pediatric Anesthesia*, 18:160–166, 2008.

[92] USA National Instruments. Ni-usb6221 adc technical notes. *http://sine.ni.com/ds/app/doc/p/id/ds-10/lang/en#header4*, 2011.

[93] Olympus NDT. Ultrasound transducer technical notes. *http://www.olympus-ims.com/*, 2011.

[94] E. A. Neppiras. Acoustic cavitation. *Physics reports*, 61(3):159–251, 1980.

[95] Y. Y. Petrov, I. Y. Petrova, I. A. Patrikeev, R. O. Esenaliev, and D. S. Prough. Multiwavelength optoacoustic system for noninvasive monitoring of cerebral venous oxygenation: a pilot clinical test in the internal jugular vein. *Optics letters*, 31(12):1827–1829, 2006.

[96] D. J. Pine, D. A. Weitz, P. M. Chaikin, and E. Herbolzheimer. Diffusing wave spectroscopy. *Physical review letters*, 60(12):1134–1137, 1988.

[97] M. S Plesset and A. Prosperetti. Bubble dynamics and cavitation. *Annual Review of Fluid Mechanics*, 9(1):145–185, 1977.

[98] S. Powell and T. S. Leung. Highly parallel monte-carlo simulations of the acousto-optic effect in heterogeneous turbid media. *Journal of Biomedical Optics*, 17(4):045002, 2012.

[99] A. Prosperetti. Nonlinear oscillations of gas bubbles in liquids: steady-state solutions. *The Journal of the Acoustical Society of America*, 56:878, 1974.

[100] A. Prosperetti. Thermal effects and damping mechanisms in the forced radial oscillations of gas bubbles in liquids. *The Journal of the Acoustical Society of America*, 61:17, 1977.

[101] A. Prosperetti, L. A Crum, and K. W Commander. Nonlinear bubble dynamics. *The Journal of the Acoustical Society of America*, 83:502, 1988.

[102] F. Ramaz, B. Forget, M. Atlan, A. C. Boccara, M. Gross, P. Delaye, and G. Roosen. Photorefractive detection of tagged photons in ultrasound modulated optical tomography of thick biological tissues. *Optics Express*, 12(22):5469–5474, 2004.

[103] L. Rayleigh. On the pressure developed in a liquid during the collapse of a spherical cavity. *Phil. Mag*, 34(200):94–98, 1917.

[104] K. Reinhart, H. J Kuhn, C. Hartog, and D. L Bredle. Continuous central venous and pulmonary artery oxygen saturation monitoring in the critically ill. *Intensive care medicine*, 30(8):1572–1578, 2004.

[105] N. Roche-Labarbe, S. A. Carp, A. Surova, M. Patel, D. A. Boas, P. E. Grant, and M. A. Franceschini. Noninvasive optical measures of CBV, StO2, CBF index, and rCMRO2 in human premature neonates' brains in the first six weeks of life. *Human brain mapping*, 31:341–352, 2010.

[106] J. J. Rychak, J. R. Lindner, K. Ley, and A. L. Klibanov. Deformable gas-filled microbubbles targeted to p-selectin. *Journal of controlled release*, 114(3):288–299, 2006.

[107] S. Sakadzic and L. V Wang. Ultrasonic modulation of multiply scattered coherent light: an analytical model for anisotropically scattering media. *Physical Review E*, 66(2):26603, 2002.

[108] S. Sakadzic and L. V Wang. Modulation of multiply scattered coherent light by ultrasonic pulses: An analytical model. *Physical Review E*, 72(3):36620, 2005.

[109] S. Sakadzic and L. V Wang. Correlation transfer and diffusion of ultrasound-modulated multiply scattered light. *Physical review letters*, 96(16):163902, 2006.

[110] S. Sakadzic and L. V Wang. Correlation transfer equation for ultrasound-modulated multiply scattered light. *Physical Review E*, 74(3):36618, 2006.

[111] B. E. A. Saleh and M. C. Teich. Multiplied-poisson noise in pulse, particle, and photon detection. *Proceedings of the IEEE*, 70:229, 1982.

[112] A. Sassaroli, C. Blumetti, F. Martelli, L. Alianelli, D. Contini, A. Ismaelli, and G. Zaccanti. Monte carlo procedure for investigating light propagation and imaging of highly scattering media. *Applied optics*, 37(31):7392–7400, 1998.

[113] P. A. Schumann, J. P. Christiansen, R. M. Quigley, T. P. Mccreery, R. H. Sweitzer, E. C. Unger, J. R. Lindner, and T. O. Matsunaga. Targeted-microbubble binding selectively to gpiib iiia receptors of platelet thrombi. *Investigative radiology*, 37(11):587, 2002.

[114] C. A. Sennoga, V. Mahue, J. Loughran, J. Casey, J. M. Seddon, M. Tang, and R. J. Eckersley. On sizing and counting of microbubbles using optical microscopy. *Ultrasound in Medicine & Biology*, 36(12):2093–2096, 2010.

[115] I. S. Seo, J. S. You, C. K. Hayakawa, and V. Venugopalan. Perturbation and differential monte carlo methods for measurement of optical properties in a layered epithelial tissue model. *Journal of Biomedical Optics*, 12:014030, 2007.

[116] M. Sheinberg, M. J. Kanter, C. S. Robertson, C. F. Contant, R. K. Narayan, and R. G. Grossman. Continuous monitoring of jugular venous oxygen saturation in head-injured patients. *Journal of neurosurgery*, 76(2):212–217, 1992.

[117] M. L Shendeleva and J. A Molloy. Diffuse light propagation in a turbid medium with varying refractive index: Monte carlo modeling in

a spherically symmetrical geometry. *Applied optics*, 45(27):7018–7025, 2006.

[118] C. R. Simpson, M. Kohl, M. Essenpreis, and M. Cope. Near-infrared optical properties of ex vivo human skin and subcutaneous tissues measured using the monte carlo inversion technique. *Physics in Medicine and Biology*, 43:2465, 1998.

[119] P. C. Sontum and C. Christiansen. Precision and accuracy of analysis of air-filled albumin microspheres using coulter multisizer mark II. *Journal of pharmaceutical and biomedical analysis*, 12(10):1233–1241, 1994.

[120] M. R Sprague, E. Cherin, D. E Goertz, and F. S Foster. Nonlinear emission from individual bound microbubbles at high frequencies. *Ultrasound in medicine & biology*, 36(2):313–324, 2010.

[121] H. J Van Staveren, C. J. M Moes, J. Van Marle, S. A Prahl, and M. J. C van Gemert. Light scattering in intralipid-10% in the wavelength range of 400-1100 nm. *Appl. Opt*, 30(31):4507–4514, 1991.

[122] E. Stride. The influence of surface adsorption on microbubble dynamics. *Philosophical Transactions of the Royal Society A: Mathematical, Physical and Engineering Sciences*, 366(1873):2103, 2008.

[123] E. Stride and N. Saffari. Microbubble ultrasound contrast agents: a review. *Proceedings of the Institution of Mechanical Engineers, Part H: Journal of Engineering in Medicine*, 217(6):429–447, 2003.

[124] E. Stride and N. Saffari. On the destruction of microbubble ultrasound contrast agents. *Ultrasound in medicine & biology*, 29(4):563–573, 2003.

[125] E. Stride and N. Saffari. Investigating the significance of multiple scattering in ultrasound contrast agent particle populations. *IEEE*

Transactions on Ultrasonics, Ferroelectrics and Frequency Control, 52(12):2332–2345, 2005.

[126] E. Stride, M. X. Tang, and R. J. Eckersley. Physical phenomena affecting quantitative imaging of ultrasound contrast agents. *Applied Acoustics*, 70(10):1352–1362, 2009.

[127] A. Torricelli, A. Pifferi, P. Taroni, E. Giambattistelli, and R. Cubeddu. In vivo optical characterization of human tissues from 610 to 1010 nm by time-resolved reflectance spectroscopy. *Physics in medicine and biology*, 46:2227, 2001.

[128] T. A. Tortoriello, S. A. Stayer, A. R. Mott, E. Dean McKenzie, C. D. Fraser, D. B. Andropoulos, and A. C. Chang. A noninvasive estimation of mixed venous oxygen saturation using near-infrared spectroscopy by cerebral oximetry in pediatric cardiac surgery patients. *Pediatric Anesthesia*, 15(6):495–503, 2005.

[129] L. Trilling. The collapse and rebound of a gas bubble. *Journal of Applied Physics*, 23(1):14–17, 2009.

[130] K. Vokurka. Amplitudes of free bubble oscillations in liquids. *Journal of Sound and Vibration*, 141(2):259–275, 1990.

[131] J. A Wahr, K. K Tremper, S. Samra, and D. T Delpy. Near-infrared spectroscopy: theory and applications. *Journal of cardiothoracic and vascular anesthesia*, 10(3):406–418, 1996.

[132] L. Wang, S. L Jacques, and L. Zheng. Mcml - monte carlo modeling of light transport in multi-layered tissues. *Computer methods and programs in biomedicine*, 47(2):131–146, 1995.

[133] L. V Wang. Mechanisms of ultrasonic modulation of multiply scattered coherent light: a monte carlo model. *Optics Letters*, 26(15):1191–1193, 2001.

[134] L. V Wang. Mechanisms of ultrasonic modulation of multiply scattered coherent light: an analytic model. *Physical Review Letters*, 87(4):43903, 2001.

[135] H. M. Watzman, C. D. Kurth, L. M. Montenegro, J. Rome, J. M. Steven, and S. C. Nicolson. Arterial and venous contributions to near-infrared cerebral oximetry. *Anesthesiology*, 93:947, 2000.

[136] G. E. R. Weller, F. S. Villanueva, E. M. Tom, and W. R. Wagner. Targeted ultrasound contrast agents: In vitro assessment of endothelial dysfunction and multi-targeting to icam-1 and sialyl lewisx. *Biotechnology and bioengineering*, 92(6):780–788, 2005.

[137] B. C Wilson and G. Adam. A monte carlo model for the absorption and flux distributions of light in tissue. *Medical Physics*, 10:824, 1983.

[138] G. Yao, S. Jiao, and L. V Wang. Frequency-swept ultrasound-modulated optical tomography in biological tissue by use of parallel detection. *Optics Letters*, 25(10):734–736, 2000.

[139] B. Yuan. Ultrasound-modulated fluorescence based on a fluorophore-quencher-labeled microbubble system. *Journal of Biomedical Optics*, 14:024043, 2009.

[140] B. Yuan, Y. Liu, P. M. Mehl, and J. Vignola. Microbubble-enhanced ultrasound-modulated fluorescence in a turbid medium. *Applied Physics Letters*, 95(18), 2009.

Monte Carlo simulations of acousto-optics with microbubbles

Jack Honeysett*[a], Eleanor Stride[b], Terence Leung[a]
[a]Dept. of Medical Physics and Bioengineering, University College London, UK
[b]Dept. of Mechanical Engineering, University College London, UK

ABSTRACT

Acousto-optic (AO) signals can be very weak and the aim of this work was to investigate their amplification using microbubbles. The acoustic pressure radiated by the microbubbles produces refractive index changes in the surrounding medium, and this is proposed as an additional mechanism which modulates the phase of photons. The analytical form of this additional modulation is derived based on the Rayleigh-Plesset equation, which describes microbubble oscillations, in the case where the microbubble oscillations are linear under low applied ultrasound pressure. We show that microbubbles can increase the modulation depth of the AO signal using Monte Carlo simulations. The increase in modulation depth is dependent on the applied ultrasound frequency and the resonance frequency of the microbubbles.

Keywords: acousto-optics, microbubbles, Monte Carlo, ultrasound-modulated optical tomography

1. INTRODUCTION

Optical imaging in biological tissue has many clinical applications, such as breast cancer diagnosis, blood oxygen saturation measurements and neonatal brain monitoring[1]. These techniques are limited by strong scattering of light in the medium. The highly diffusive nature of light propagation in tissue imposes an inherent limit on the spatial resolution of any purely optical measurements. Hybrid techniques combining the spatial resolution of focused ultrasound (US) with light measurements (acousto-optics, or ultrasound modulated optical tomography) offer a solution to this limitation. The principle of biomedical acousto-optics (AO) is that photons entering the US focal region are modulated at the US frequency. This process effectively 'tags' light which has passed through the area of interest. However, extracting this 'tagged' signal from the vast majority of un-modulated photons is not a trivial task because of the low signal-to-noise ratio of the AO signal.

Microbubbles in the blood have been shown to be effective in improving US image contrast[3]. In acousto-optic measurements, it has been shown that microbubbles can be used to enhance the weak signals of ultrasound-modulated fluorescence[2]. In general, we expect that microbubble oscillations will significantly alter the optical properties of the medium, e.g. refractive index and optical scattering. A significant increase in the AO signal would allow these biomedical techniques to be applied to areas of the body other than those at the very surface. For example, the pulmonary artery is one area in which oximetry measurements are of clinical importance in critical care[4]; non-invasive acousto-optics would remove the need for catherisation, a procedure which is both costly and carries significant patient risk.

Here we use Monte Carlo simulations to investigate the effect of microbubbles on the AO signal under relatively low applied US pressures, where microbubble oscillations are linear and purely harmonic. These are presented as preliminary results, which both shed light on the theoretical basis of the use of microbubbles in acousto-optics and will guide future work in the non-linear oscillation regime under a higher applied US pressure.

* j.honeysett@ucl.ac.uk; www.ucl.ac.uk/~ucbpjeh

Photons Plus Ultrasound: Imaging and Sensing 2010, edited by Alexander A. Oraevsky, Lihong V. Wang,
Proc. of SPIE Vol. 7564, 75640K · © 2010 SPIE · CCC code: 1605-7422/10/$18 · doi: 10.1117/12.842030

2. MODELLING MICROBUBBLES

2.1 Equation of motion

The Rayleigh-Plesset equation is commonly used to describe the radial oscillations of bubbles in a pressure field[5]:

$$\rho_L\left(R\ddot{R}+\frac{3}{2}\dot{R}^2\right)+p_0-p_A(t)-p_G(R)+\frac{4\dot{R}}{R}\eta_L=f_{ce}+f_{cd}, \quad (1)$$

where R(t) is the radius of the bubble as a function of time, and $p_A(t)$ is the applied acoustic pressure. The terms f_{ce} and f_{cd} are the elastic and dissipative resistance respectively due to the bubble coating. The form of these resistive terms is taken from the model developed by Hoff[6].

The remaining variables in these equations are the properties of the bubble. The values of these parameters have been estimated from experiments on commercially available (SonoVue®) microbubbles[7]: the equilibrium radius of the microbubbles R_0 = 2.25 μm, density of the surrounding fluid ρ_L = 1000 kg m^{-3} and viscosity η_L = 1 mPa s. The equilibrium interfacial tension at the microbubble surface σ_0 = 0.05 N m^{-1}. The effective thickness d_s = 1 nm, effective shear modulus G_s = 20 MPa and effective shear viscosity η_s = 1.5 Pa s. The ambient surrounding pressure p_0 = 100 kPa.

Equation (1) is solved for the linear case by assuming that the radial oscillations are small, and take the form $R(t)=R_0\{1+z(t)\}$, where z(t) << 1. The Rayleigh-Plesset equation then reduces to the form of a driven harmonic oscillator, with solution:

$$R(t)=R_0\left\{1+\frac{p_A}{\beta}\sin(\boldsymbol{k}_a.\boldsymbol{r}_j-\omega_a t+\xi)\right\}, \quad (2)$$

where β (the response function) depends strongly on the applied US frequency ω_a. $\mathbf{r}_j$ is the vector position of the microbubble in the US field, and $\mathbf{k}_a$ is the acoustic wave vector. The phase shift ξ is also a function of ω_a.

$$\beta=\sqrt{{\omega_a}^2(4\eta_l+12\frac{d_s\eta_s}{R_0})^2+(3p_0+\frac{6\sigma_0}{R_0}+12\frac{G_s d_s}{R_0}-\rho_l R_0^2{\omega_a}^2)^2}, \quad (3)$$

$$\xi=\arctan\left(\omega_a(4\eta_l+12\frac{d_s\eta_s}{R_0})/(\rho_l R_0^2{\omega_a}^2-3p_0-\frac{6\sigma_0}{R_0}-12\frac{G_s d_s}{R_0})\right). \quad (4)$$

2.2 Optical scattering from microbubbles

In order to incorporate microbubbles into the Monte Carlo model of light transport, it is necessary to model the scattering phase function of light from a microbubble. The optical scattering from a spherical particle can be described by Mie theory and calculated using a Matlab-based algorithm[8] for a microbubble of radius R_0 = 2.25 μm, refractive index ratio 1/1.33 and optical wavelength λ = 0.5 μm. The mean value of the cosine of the scattering angle for this phase function was found to be $\langle\cos\theta\rangle$ = 0.85. This suggests that the Henyey-Greenstein function[9] with an anisotropic factor of g = 0.85 will be a suitable approximation to the angular distribution. In the case of linear microbubble oscillations, the radius changes are small enough (±5%) that the phase function can be assumed to be constant over time.

For the purposes of computational speed in the Monte Carlo simulations, the analytically simpler Henyey-Greenstein approximation is used to model optical scattering from microbubbles.

2.3 Photon phase modulation by microbubbles

The various mechanisms by which US modulates the phase of photons in the target region are well established. In this model we consider the modulation of the local refractive index of the medium by the applied US pressure (leading to modulation of the wavelengths of photons), and the displacement of scatterers (hence the modulation of the optical path lengths between scattering events) proposed by Wang[10]. In addition to these, a new mechanism of ultrasonic modulation due to the presence of microbubbles is proposed.

Oscillating microbubbles radiate pressure outwards from their surface. This is predicted by potential flow theory to reduce with radial distance from the microbubble, r_b. The equation can be simplified in the case of linear oscillations, where the radiated pressure is given by[5]:

$$p_{rad}(r_b, t) = \frac{1}{r_b}\left(\rho_L {R_0}^2 \frac{\partial^2 R}{\partial t^2}\right). \qquad (5)$$

This additional pressure will also modulate the refractive index of the medium in the vicinity of the microbubble, hence there will be a further phase shift introduced to photons in the US focal region. This will only be significant for photons that approach close to the surface of a microbubble, i.e. when scattering (see figure 1).

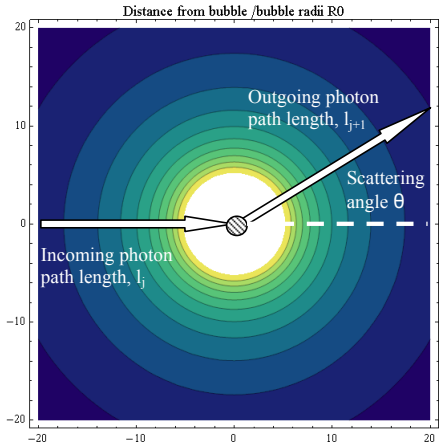

Figure 1: The contrast shows the radiated pressure increasing as the photon approaches the microbubble. The overall additional photon phase shift is calculated by integrating the phase shift along these photon paths.

This phase shift is integrated over the path length of the photon with respect to the radial distance r_b, making use of the symmetry of the situation and modelling a microbubble as a point scatterer:

$$\varphi_{rj}(t) = \int_{l_j}^{0} k_0 \Delta n(\boldsymbol{r}_j, r_b, t)(-dr_b) + \int_0^{l_{j+1}} k_0 \Delta n(\boldsymbol{r}_j, r_b, t) dr_b = \frac{n_0 k_0 \eta}{\rho_L v_a^2}\left\{\int_0^{l_j} p_{rad}(\boldsymbol{r}_j, r_b, t) dr_b + \int_0^{l_{j+1}} p_{rad}(\boldsymbol{r}_j, r_b, t) dr_b\right\}, \qquad (6)$$

where l_j is the free path length of the photon as it approaches the microbubble, l_{j+1} is the path length as the photon recedes from the microbubble after scattering, $\mathbf{r}_j$ is the position of the microbubble within the US field, η is the piezo-optical coefficient of the medium, v_a is the acoustic velocity, ρ_L is the density of the medium and k_o is the optical wavevector. Substituting equation (2) and (5) into equation (6) and integrating gives the additional phase shift due to this radiated pressure, φ_{rj}:

$$\varphi_{rj}(t) = \frac{n_0 k_0 \eta k_a^2 R_0^3 p_A}{\beta} \sin(\boldsymbol{k}_a.\boldsymbol{r}_j - \omega_a t + \xi)\left\{\ln\left(\frac{R_0}{l_j}\right) + \ln\left(\frac{R_0}{l_{j+1}}\right)\right\}. \qquad (7)$$

This contributes along with the two original US mechanisms to the autocorrelation function of the detected signal, $G_1(\tau) = \int_0^\infty p(s)\,\langle E_s(t){E_s}^*(t+\tau)\rangle ds$, where the contribution from each photon path is $\langle E_s(t){E_s}^*(t+\tau)\rangle = \langle \exp[-i\Delta\varphi(t,\tau)]\rangle$. The phase variation between two photons with a time lag of τ is given by $\Delta\varphi(t,\tau) = \varphi(t+\tau) - \varphi(t)$. The new mechanism of ultrasonic modulation due to the pressure radiated from microbubbles contributes to this phase variation, along with the original two mechanisms, as follows:

$$\Delta\varphi(t,\tau) = \sum_{j=1}^{N+1} \Delta\varphi_{nj} + \sum_{j=1}^{N} \Delta\varphi_{dj} + \sum_{j=1}^{N} \Delta\varphi_{rj}, \qquad (8)$$

where $\Delta\varphi_{nj}$ is the phase variation due to the ultrasound-modulated refractive index and $\Delta\varphi_{dj}$ is the phase variation due to displacement of scatterers in the applied US field.

3. MONTE CARLO MODEL

3.1 Modelling procedure

The computational model is based on the Monte Carlo model proposed by Wang (2001) which considers two mechanisms (described earlier) of ultrasonic modulation of multiply scattered coherent light by US plane wave[10]. In addition to scattering from the biological medium, optical scattering by microbubbles is included in this work. We also consider the additional mechanism due to the radiated pressure produced by microbubbles (equation 7). The Monte Carlo model was implemented on a graphics-processing-unit (GPU) platform by modifying a GPU based Monte Carlo code on photon transport[11].

The simulations were performed in a slab geometry, with a thickness of 2 cm. Optical scattering in the background medium is modelled using the same properties as for a 1% Intralipid solution[12]: anisotropic factor g = 0.77 with a scattering coefficient μ_s = 48 cm^{-1}. The biological medium is also an optical absorber, with absorption coefficient μ_a = 0.015 cm^{-1}. US is included as a plane wave at a given frequency f_a (in Hz) and amplitude A (in nm).

A scattering coefficient for the population of microbubbles in the sample, $\mu_{s,b}$, can be estimated by considering the effective cross-sectional area of a microbubble[13]. This will of course vary with time and space, as the radius of a microbubble is a function of time and space. When the applied US pressure is low, the microbubble oscillations become linear and the variation of the radius is small. As a first approximation the time-averaged value is used to represent the radius of all microbubbles:

$$\langle \mu_{s,b}(t) \rangle = \pi \langle R(t)^2 \rangle \rho_b Q = \pi \rho_b Q R_0^2 \left(1 + \frac{p_A^2}{2\beta^2}\right), \qquad (9)$$

where Q is the quality factor of the scattering, and the limit of Q~2 for scatter sizes much larger than the optical wavelength is assumed[13]. A clinically plausible value for the concentration of microbubbles in the bloodstream is estimated to be $\rho_b = 10^5$ mm^{-3}. The Henyey-Greenstein scattering phase function with g = 0.85 has been used to generate the deflection angle of the microbubbles (see Section 2.2).

The process for calculating whether a photon collides with a microbubble or a biological scatterer is as follows:

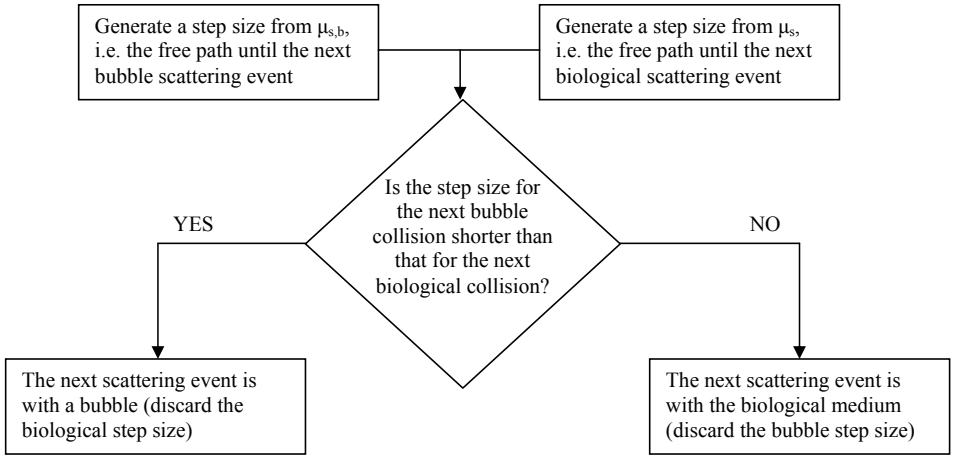

Figure 2: Flowchart describing the generation of a photon free path length in a population of two distinct scattering species.

This is statistically equivalent to generating a single free path length from the combined distribution of both scatterer populations (with coefficient $\mu_s + \mu_{s,b}$).

3.2 Simulation results

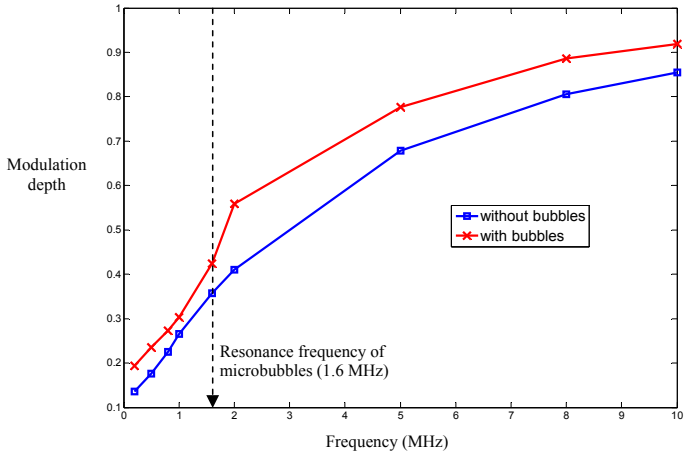

Figure 3: Monte Carlo results for applied US frequencies of 1 MHz $\leq f_a \leq$ 10 MHz. The US amplitude is A = 1.7 nm. The two curves show results with and without microbubbles.

Figure 3 shows an increase in modulation depth at all applied US frequencies when microbubbles are introduced. It is significant to note that the extra modulation due to microbubbles leads to a larger overall increase in modulation depth when the US frequency exceeds the resonance frequency of the microbubbles (this is predicted from the given microbubble parameters to be 1.6 MHz). Below this frequency, the modulation due to radiated pressure is out of phase with the modulation due to the applied US pressure, as shown by figure 4.

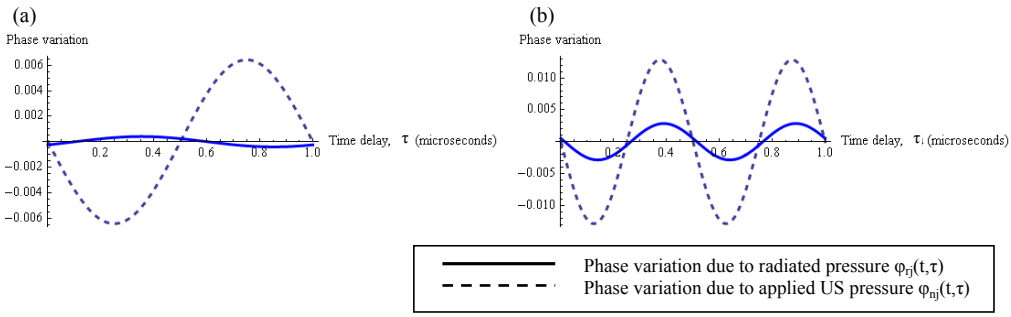

Figure 4: The phase variation due to microbubble radiated pressure [$\varphi_{rj}(t,\tau)$] and the phase variation due to applied US pressure [$\varphi_{nj}(t,\tau)$]: (a) below the resonance frequency (f_a = 1 MHz), φ_{rj} and φ_{nj} out of phase and (b) above the resonance frequency (f_a = 2 MHz), φ_{rj} and φ_{nj} in phase

4. EXPERIMENTAL RESULTS

Microbubble enhancement of the acousto-optic effect is also demonstrated in an experimental phantom. The tissue phantom used is a thin silicone tube (internal diameter 6 mm, thickness 2 mm) which is filled with 1% Intralipid solution. The optical properties of this solution can be estimated from its concentration[12]: $\mu_s = 47.7\ cm^{-1}$, $\mu_a = 0.015\ cm^{-1}$ and $g \sim 0.77$. A second phantom is half filled with 2% Intralipid solution and a solution of a commercially available microbubble (Expancel™), giving an identical 1% Intralipid solution containing microbubbles.

The phantom is placed in the focal region of an US transducer (central frequency 1 MHz, producing 10 μs tone bursts at a rate of 5 kHz, Olympus Panametrics V392-SU, nominal element diameter=1.5inch, point focus at 2.5inch, focal zone 2.56mm x 29.36mm at -6dB) and the beam path of a 5 mW He-Ne laser (632 nm, CW). This has a relatively long coherence length (>> 1 m). The autocorrelation of the speckle pattern is measured with a photon counter and digital correlator. The amplitude of the US field at the focus is approximately 80 kPa in water. This is relatively low, and predicted by the model to be in the linear regime of microbubble oscillations. Figure 5 shows this configuration.

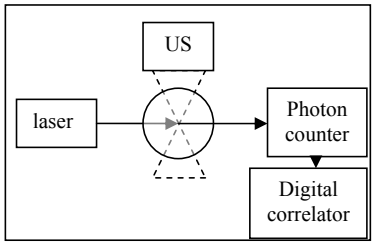

Figure 5: Diagram of experimental geometry (viewed from above). The tube phantom is in the centre, and orientated vertically.

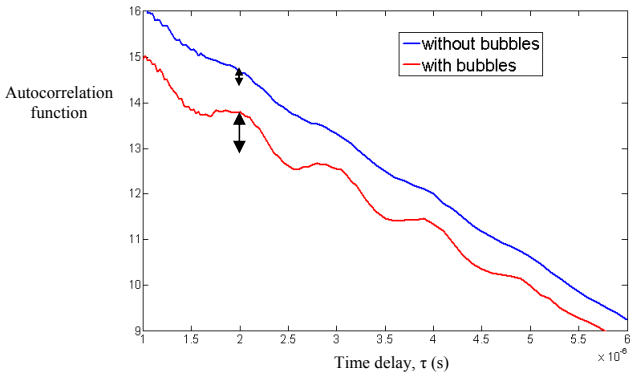

Figure 6: Autocorrelation function showing acousto-optic modulation in a 1% intralipid phantom with and without microbubbles. The arrows show the acousto-optic modulation depth.

Figure 6 shows that even with a relatively low applied US pressure, and microbubbles undergoing linear small amplitude oscillations, the acousto-optic modulation depth is increased significantly by the presence of microbubbles. The component of the autocorrelation function which varies at the US frequency (with a period of 1 μs) originates from photons passing through the US focal region. The decay of the autocorrelation function is mainly due to the use of gating in the optical detection. The experiment performed here mainly serves to demonstrate the potential of using microbubbles to amplify the AO signals. It is not our intention to verify our simulation results with the experimental results since the experimental and the simulation configurations are very different, e.g. focused US (experiment) compared with plane-wave US (simulation), and tube geometry (experiment) compared with slab geometry (simulation).

5. CONCLUSIONS

These results demonstrate that microbubbles can be used to enhance the modulation depth in acousto-optic measurements. The amplification effect of microbubbles on the acousto-optic signal has been observed experimentally in a tissue phantom, and this effect has been investigated with Monte Carlo simulations. A new mechanism affecting the phase of photons is proposed, derived analytically from the radiated pressure of an oscillating microbubble. This explains the increase in modulation depth, and also the strong frequency dependence of the AO signal when using microbubbles. In particular, when microbubbles are driven by ultrasound with a frequency lower than the resonance frequency of the microbubbles, the resulting radiated pressure is out of phase with the applied ultrasound. Despite this, the modulation depth is still increased when microbubbles are present: although the radiated pressure is out of phase with the ultrasound, the increase in scattering events compensates for this. Above the resonance frequency however, this radiated pressure acts in phase with the ultrasound, producing an increased overall phase shift in photons, and hence a larger increase in modulation depth.

It is important to note that these models are valid only for linear microbubble oscillations, with a small change in radius (±5%). At higher applied ultrasound pressures microbubble oscillations become non-linear, which will result in changes in their optical scattering properties. The next stage of this work, which is currently in progress, is to model microbubbles with spatially and temporally varying scattering properties.

6. ACKNOWLEDGEMENTS

The authors would like to acknowledge the help of Sava Sakadžić in implementing the acousto-optic simulations, and Erik Alerstam for assistance with regards to performing GPU computation. This work was funded primarily by the Engineering and Physical Science Research Council (Grant code: EP/G005036/1), the British Heart Foundation and the Medical Research Council, who are the main sponsors of the CoMPLEX department at UCL (Centre of Mathematics and Physics in the Life Sciences and Experimental Biology).

REFERENCES

1. Gibson A. P., Hebden J. C., Arridge S. R.: “Recent advances in diffuse optical imaging” Phys. Med. Biol. 50, R1-R43 (2005)
2. Yuan B.: “Ultrasound-modulated fluorescence based on a fluorophore-quencher-labeled microbubble system” J. Biomed. Opt. Vol. 14, 024043 (2009)
3. Lindner J. R.: “Microbubbles in medical imaging: current applications and future directions” Nat. Rev. 3, 527-532 (2004)
4. Reinhart K. *et al.*: “Continuous central venous and pulmonary artery oxygen saturation monitoring in the critically ill” Intensive Care Med. 30, 1572-1578 (2004)
5. Plesset M., Prosperetti A.: “Bubble dynamics and cavitation” Ann. Rev. Fluid Mech. 9, 145-185 (1977)
6. Hoff L., Sontum P. C., Hovern J. M.: “Oscillations of polymeric microbubbles: Effect of the encapsulating shell” J. Acoust. Soc. Am. 107:4, 2272-2280 (2000)
7. Stride E., Tang M-X., Eckersley R. J.: “Physical phenomena affecting quantitative imaging of ultrasound contrast agents” Appl. Acoust., 70(10), 1352-1362 (2009)
8. Mätzler C.: “MATLAB Functions for Mie Scattering and Absorption” IAMP Research Report, University of Bern (2002)
9. Henyey L. G., Greenstein J. L.: “Diffuse radiation in the galaxy” Astrophys. J. 93, 70-83 (1941)
10. Wang L. V.: “Mechanisms of ultrasonic modulation of multiply scattered coherent light: a Monte Carlo model” Optics Letters vol. 26, no. 15 1191 (2001)
11. Alerstam E., Svensson T., Andersson-Engels S.: “Parallel computing with graphics processing units for high-speed Monte Carlo simulation of photon migration,” Journal of Biomedical Optics, 13(6), 060504 (2008)
12. Van Staveren H. J. *et al.*: “Light scattering in Intralipid-10% in the wavelength range of 400-1100 nm” Applied Optics Vol. 30, Issue 31, 4507-4514 (1991)
13. Van De Hulst H. C.: “Multiple Light Scattering” vol. 1, Academic Press, New York (1980)